UNIVERSITÀ DEGLI STUDI DI TRIESTE

UNIVERSITÀ DEGLI STUDI DI TRIESTE

38° CICLO DEL DOTTORATO DI RICERCA IN

SCIENZE DELLA TERRA E MECCANICA DEI FLUIDI

Finanziato dall'Unione europea - NextGenerationEU
Funded by the European Union - NextGenerationEU

Boundaries behaviour of sediment gravity current

Settore scientifico-disciplinare: **Icar/02**

DOTTORANDO / A
Antonio Ammendola

COORDINATORE
PROF. Stefano Maset

SUPERVISORI DI TESI
PROF. Michele Rebesco
PROF. Federico Roman
PROF. Stefano Salon
PROF. Federico Falcini

ANNO ACCADEMICO 2024/2025

Finanziato dall'Unione europea NextGenerationEU
Ministero dell'Università e della Ricerca
Italiadomani
UNIVERSITÀ DEGLI STUDI DI TRIESTE

Boundaries behaviour of sediment gravity current

Antonio Ammendola

February 2026

Contents

1 Introduction **4**

2 A brief introduction to gravity current dynamics **8**
2.1 Gravity currents - main features 8
2.2 Turbidity currents 10
2.3 Hyperpycnal flows 11
2.4 Dimensionless parameters for gravity current characterization . . 12

3 Material and Methods **14**
3.1 Mathematical Model 14
3.1.1 Gravity Currents experiments 14
3.1.2 Sediment-Laden flows 17
3.1.3 wall-functions 18
3.2 Hyperpycnal flows: Experimental Setup 22

4 Study Cases and Quality assessment **25**
4.1 Gravity currents in lock-exchange 25
4.2 Sediment-laden flows in lock-exchange 28
4.3 Hyperpycnal flows experiments 29
4.4 Spatial and Temporal Quality Assessment 31
4.4.1 Gravity currents in lock-exchange assessment 31
4.4.2 Sediment-laden flows in lock exchange assessment 36

5 Results for gravity current: boundary layer and wall modeling **38**
5.1 Validation 38
5.1.1 Flow topology 38
5.1.2 Wall-shear stresses 39
5.2 Boundary layer 42
5.3 High Reynolds cases and wall models 48
5.3.1 Flow topology 48
5.3.2 Wall-shear stresses 51

5.3.3 Entrainment . . . 55
5.3.4 Near-wall region . . . 59

6 Results for sediment-laden flow: interaction with bottom structure 62
6.1 Saline and low-concentration Turbidity Currents . . . 62
6.1.1 Flow Topology . . . 62
6.1.2 Density Fields . . . 65
6.1.3 Entrainment . . . 68
6.2 Turbidity Current . . . 70
6.2.1 Flow topology . . . 70
6.2.2 Density Fields . . . 72
6.2.3 Entrainment . . . 74
6.2.4 Wall-Shear Stresses . . . 77
6.2.5 Shields Parameter . . . 79
6.2.6 Drag and Lift Forces . . . 82

7 Results for hyperpycnal flow: plunging point and mixing layer 85
7.1 Determination of the plunging point . . . 85
7.2 Surface velocity vs Plunging Point . . . 89
7.3 Transient Fields . . . 91

8 Conclusions 100

9 Bibliography 103

Abstract

Gravity currents are buoyancy-driven flows generated by horizontal density gradients, governing the transport of mass, momentum, and scalars in both natural and engineered systems. Examples include brine disposal, reservoir operations, large-scale ocean overturning circulation, industrial pollutant releases, river inflows into lakes and coastal regions, seabed-propagating turbidity currents, and sediment-laden hyperpycnal plumes generated during flood events. Despite their ubiquity and practical importance, gravity currents remain challenging to characterize and predict. The objective of this doctoral thesis is to improve the understanding of the phenomenon in specific contexts through a combined use of numerical and experimental approaches. First, gravity currents induced by salinity differences are analyzed numerically using Large Eddy Simulations to understand the behavior near the bottom wall. Second, the impact of currents on submerged structures, like pipes, is analyzed in terms of the acting forces and the associated erosion and deposition processes. In particular, the case in which density variations are due to the presence of sediments (turbidity currents) is examined. In this context, the analyses are carried out using a two-phase numerical model in order to more accurately represent the dispersed granular phase. Third, the surface dynamics of a hyperpycnal plume, representative of a river–basin system, are analyzed using laboratory data obtained from the Coriolis platform (LEGI, Grenoble), with the aim of assessing the influence of the inlet dimensions. Simulations reveal a well-defined boundary layer beneath the current head, with velocity profiles approximately following a logarithmic law. The use of a parameterized wall shear stress enables an adequate representation of the flow dynamics while employing coarse computational grids, thereby reducing the computational cost by two orders of magnitude. The presence of a bottom cylindrical obstacle strongly modifies flow dynamics, mixing, and near-bed shear, enhancing erosive capacity in the rear and generating significant drag and lift forces, capable of mobilizing both fine and coarse sediments. Finally, it is observed that for hyperpycnal flows the plunging location shifts linearly downstream with increasing inlet width, and Kelvin–Helmholtz instabilities dominate the mixing and entrainment dynamics.

1 Introduction

Gravity currents constitute a fundamental class of buoyancy-driven flows generated by horizontal density gradients and play a key role in a wide range of natural and engineered systems. Such density contrasts may arise from natural processes, including thermohaline circulation, which contributes to the regulation of global ocean temperatures and large-scale oceanic transport [43]. They may also originate from atmospheric and hydrological phenomena such as avalanches, pyroclastic density currents, and river inflows into stratified basins [5, 48]. In engineered and anthropogenic contexts, gravity currents are commonly encountered in the discharge of dense industrial effluents, desalination brine releases, wastewater outfalls, and seawater intrusion into coastal and inland reservoirs [20, 13, 29, 81]. Owing to their ability to propagate over long distances while maintaining a coherent structure, gravity currents can significantly influence mixing, transport, and deposition processes in both natural and built environments.

When the presence of suspended sediment particles further enhances the density contrast, the flow evolves into a turbidity current. These sediment-laden gravity currents represent one of the primary mechanisms for sediment transport in aquatic environments and play a central role in shaping submarine channels, continental slopes, and deep-sea fans [74, 28, 53]. Turbidity currents are frequently triggered by river flood events that deliver large sediment loads into lakes, reservoirs, and marine basins, giving rise to hyperpycnal inflows that plunge beneath the ambient water column [83]. Their strong erosive capacity and associated depositional patterns have major implications for reservoir siltation, submarine infrastructure stability, and geohazard assessment [31].

Motivated by these wide-ranging applications and impacts, a detailed understanding of the fundamental dynamics of gravity currents is essential. From a fluid-mechanical perspective, gravity currents are inherently complex phenomena whose evolution depends on a variety of controlling factors, including the release volume (finite or continuous), the initial geometry of the current, the relative importance of inertial and viscous effects, the properties of the ambient fluid (homogeneous or stratified), the density contrast between the two fluids, geometric confinement, which determines whether the flow develops in a two- or three-dimensional manner, and the characteristics of the bottom boundary, such as slope and roughness. Comprehensive treatments of these aspects can be found, for example, in [87]. Considering the canonical case of a two-dimensional, inertial gravity current generated by the instantaneous release of a finite volume over a horizontal surface, the flow initially undergoes an acceleration phase, during which potential energy is converted into kinetic energy. The subsequent propagation is commonly described in terms of three distinct regimes. In the initial slumping phase, the front advances at an approximately constant velocity, and viscous effects are negligible. As entrainment and mixing with the ambient fluid become significant, the current transitions into a self-similar phase characterized by a progressive reduction of the front velocity. Finally, when the flow slows down sufficiently, viscous effects dominate, and the current enters a

viscous phase, leading to a further decay of the propagation speed [34, 72, 79].

The main objective of this dissertation is to investigate the physical behavior of gravity currents at high Reynolds numbers, defined as Re$= UL/\nu$, where U and L denote the characteristic velocity and length of the flow, respectively, and ν is the molecular viscosity. This study employs a combined numerical and experimental approach, considering both saline and sediment-laden configurations, as well as the influence of complex geometrical constraints.

Laboratory experiments provide a fundamental physical reference for studying fluid flows. Typically, such experiments yield two-dimensional measurements along horizontal and vertical planes, obtained using techniques like Particle Image Velocimetry (PIV). High-precision three-dimensional methods, such as volumetric PIV, are also available; however, as noted by [89], their application can be challenging in flows such as gravity or turbidity currents. This is due to factors including limited fluid transparency, surface undulations, and complex interfacial structures, such as Kelvin–Helmholtz billows that develop between fluids of different densities. Additional practical limitations arise in sediment-laden flows, where the presence of suspended particles restricts the applicability and accuracy of PIV and Acoustic Doppler Velocimetry (ADV) measurements, particularly in near-wall regions dominated by viscous effects [8, 85]. In this context, numerical simulations offer a complementary tool to access flow features that are difficult to resolve experimentally, enabling a more complete interpretation of the observed dynamics. This combined approach addresses the need for robust modeling strategies capable of capturing gravity-current behavior at the high Reynolds numbers typical of geophysical applications, where the multiscale nature of turbulence and the prohibitive computational cost of Direct Numerical Simulation (DNS), scaling approximately as $\mathrm{Re}^{3.5}$, pose significant challenges [67, 27]. A widely adopted compromise between accuracy and computational efficiency is Large Eddy Simulation (LES), in which the filtered Navier-Stokes equations are solved. Within this framework, the large, energy-containing turbulent structures responsible for momentum transport and mixing are explicitly resolved, while the effects of the unresolved sub-grid scales are accounted for through a sub-grid stress (SGS) model [14]. Despite the substantial reduction in computational cost compared to DNS, LES remains prohibitively expensive for high Reynolds number flows. This limitation is primarily due to the near-wall region, characterized by intense turbulence, and near-wall eddies need to be directly resolved, as they play a crucial role in energy transport. These eddies scale in terms of wall units, meaning that as the Reynolds number increases, their size decreases rapidly, necessitating a correspondingly finer grid resolution. Properly resolving this layer incurs a computational cost proportional to $\mathrm{Re}^{1.8}$ in space and $\mathrm{Re}^{0.6}$ in time [10], requiring a grid resolution comparable to that of DNS to be accurately captured [9].

The first objective of this work is methodological and focuses on reducing the computational cost of high-fidelity simulations of gravity currents. To this end, a systematic assessment and optimization of coarse-grid LES coupled with wall-functions (WF-LES) is carried out to retain the essential near-wall physics while alleviating the stringent resolution requirements associated with fully wall-

resolved LES (WR-LES). A prerequisite for the adoption of a wall-modeled approach is the verification that the near-wall region exhibits the characteristic features of a turbulent boundary layer. In particular, velocity profiles beneath the head of the gravity current are analyzed to assess their consistency with classical descriptions of the viscous sublayer and logarithmic region. The identification of these near-wall scaling behaviors provides a physical justification for the use of wall-functions as an effective strategy to reduce computational cost while preserving accuracy [68].

Accordingly, several wall-model formulations commonly employed in wall-modeled LES of wall-bounded turbulent flows are systematically investigated in the OpenFOAM® framework. These include algebraic wall-functions derived from the law of the wall, such as the Spalding and Blended formulations [80], which provide a continuous description across the viscous sublayer and logarithmic region through constraints on the turbulent eddy viscosity. In addition, the Jayatilleke model [37] is examined, in which near-wall effects are incorporated through a modification of the turbulent diffusivity. The comparative analysis quantifies the influence of wall-model selection on the representation of near-wall dynamics in high-Reynolds-number gravity currents while enabling a substantial reduction in computational cost relative to fully wall-resolved LES.

The second objective of this dissertation is the investigation of gravity currents in complex flow domains. In particular, a simplified configuration is adopted to represent the interaction between turbidity currents and submarine cables resting on the seabed. This problem is of significant practical relevance, as turbidity currents are characterized by high Reynolds numbers and sediment concentrations capable of exerting intense hydrodynamic and erosive forces, potentially leading to damage of anthropogenic structures [31]. To address the complexities associated with flow-structure-sediment interactions, a canonical obstacle configuration is considered, consisting of a cylindrical element placed on the seabed. The presence of such an obstacle substantially modifies the flow structure, enhances mixing processes, and alters the erosive capacity of the current. This part of the study employs both single-phase (*buoyantBoussinesqPimpleFoam*) and two-phase (*SedFoam*) solvers within a wall-resolved LES framework. The numerical approaches are first validated against laboratory experiments conducted at the Hydraulic Engineering Laboratory of Roma Tre University [51], which investigated the interaction between a gravity current and a cylindrical obstacle anchored to the bed. Following validation, additional numerical simulations are performed under density contrasts representative of turbidity currents in a lock-exchange configuration. This approach enables a detailed analysis of the flow structure and near-bed dynamics, including the formation of localized regions of elevated bed shear stress. The erosive capacity of the flow is quantified through the friction velocity u_τ and the Shields parameter [78, 3], confirming the likelihood of sediment mobilization and providing insight into the localized effects of macro-roughness elements [51]. In addition, the drag and lift forces acting on the cylindrical obstacle during the passage of the current are analyzed.

The third objective of this dissertation is the experimental characteriza-

tion of hyperpycnal plumes generated by river inflows into receiving basins [5]. Laboratory experiments conducted at the Coriolis platform in the LEGI (Laboratoire des Écoulements Géophysiques et Industriels) laboratory investigate the dynamics of hyperpycnal inflows, with a particular emphasis on identifying the plunging point, defined as the location where the dense inflow detaches from the free surface and transitions into a bottom-propagating gravity current. A quantitative methodology based on the combined analysis of the Q-criterion and Turbulent Kinetic Energy fields is employed to identify this transition robustly. In addition, spectral decomposition of velocity time series is used to characterize Kelvin–Helmholtz instabilities developing within the mixing layer (for an overview on the mixing layer mechanisms, please refer to [86]).

Taken together, these analyses aim to advance the understanding of gravity current dynamics in geophysical contexts by improving computational efficiency through optimized LES strategies, by providing a systematic framework for the investigation of flow structure interactions under sediment-laden conditions, and by enhancing the characterization of the turbulent dynamics of hyperpycnal plumes.

The structure of this dissertation is as follows. Chapter 2 introduces the physical phenomena addressed in this study. Chapter 3 focuses on the methodologies employed, addressing both numerical simulations and laboratory experiments. Chapter 4 presents the case studies used to conduct the experiments and includes a detailed quality assessment of the computational meshes employed in the numerical simulations. Subsequent chapters are organized according to the specific phenomena investigated. Chapter 5 presents the results for gravity currents in a lock-exchange configuration, emphasizing the physical mechanisms and the reduction of computational costs in LES simulations. Chapter 6 addresses both gravity currents and turbidity currents in a lock-exchange setup with a cylindrical obstacle placed on the bed, analyzing flow-structure interactions in terms of bed erosion and the hydrodynamic forces exerted on the obstacle. Chapter 7 presents the experimental results obtained from the Coriolis platform, focusing on hyperpycnal plume dynamics. Finally, the concluding chapter synthesizes the findings from all aspects of this work, highlighting the integrated understanding of gravity current dynamics achieved through the combined numerical and experimental approach, the insights gained into flow-structure-sediment interactions, and the characterization of turbulent mixing in hyperpycnal plumes.

2 A brief introduction to gravity current dynamics

Gravity currents constitute a fundamental class of buoyancy-driven flows that arise whenever horizontal density gradients are established within a fluid system. Their dynamics are central to a wide range of geophysical and engineering processes, from oceanic circulation and river inflows to sediment transport and industrial discharges. Despite the diversity of contexts in which they occur, gravity currents share common physical mechanisms: the conversion of potential energy into kinetic energy, the progressive entrainment of ambient fluid, and the eventual dominance of viscous dissipation. Understanding these mechanisms is essential not only for interpreting natural phenomena but also for designing laboratory experiments and numerical simulations capable of reproducing their complex behavior. In the following subsections, canonical gravity currents, turbidity currents, and hyperpycnal flows are introduced qualitatively, together with the dimensionless parameters that provide a unified framework for their characterization. These types of currents will be subsequently analyzed quantitatively using numerical and experimental methods.

2.1 Gravity currents - main features

To provide a qualitative introduction to gravity currents and highlight their key features, the description of the simplest configuration is adopted: a two-dimensional current developing over a horizontal surface as a result of the release of a finite volume of dense fluid [63, 84]. For a more comprehensive overview, including three-dimensional cases, continuous releases, and variable bottom geometry, even in the presence of bed roughness, see, for example [35, 16, 51]

Considering Figure 1, which illustrates the different phases of the current, it can be observed that at the very beginning the system undergoes an **acceleration stage** (Figure 1a). During this stage, the potential energy stored in the initial density difference is rapidly converted into kinetic energy, setting the current in motion and establishing the characteristic front that separates the dense fluid from the lighter ambient.

Following this onset, the current typically enters what is known as the **slumping phase** (Figure 1b). In this regime, the front advances at an approximately constant velocity, and the dynamics can be regarded as essentially inviscid. The dense fluid propagates forward coherently, with minimal mixing with the surrounding environment. The slumping phase is therefore dominated by inertia, and the flow retains much of the structure imposed by the initial release conditions. However, as the current evolves, instabilities develop at the interface between the dense and the light fluid, and entrainment of ambient fluid begins to occur. During this phase, the front advances with a time scaling of t^1.

The onset of entrainment marks the transition to the **self-similar phase** (Figure 1c). In this regime, the lighter ambient fluid is progressively mixed into the dense current, altering its composition and reducing its front velocity. The

dynamics become more complex, as turbulent structures emerge and the current adjusts to the continuous dilution of its density anomaly. The term "self-similar" reflects the fact that, despite the ongoing mixing and deceleration, the overall shape of the current evolves in a geometrically consistent manner, preserving certain scaling properties that can be described analytically. This phase is crucial for understanding the long-term propagation of gravity currents, since it governs the rate at which the density contrast, and therefore the driving buoyancy force, is reduced through mixing. During this phase, the front advances with a time scaling proportional to $t^{2/3}$.

Eventually, as the current continues to decelerate and the density difference diminishes, viscous effects become increasingly significant. This leads to the final regime, known as the **viscous phase** (Figure 1d). Here, the flow is no longer dominated by inertia or large-scale turbulent mixing, but rather by the dissipative action of viscosity. The front velocity decreases further, and the current gradually loses its capacity to propagate over long distances. The viscous phase thus represents the ultimate stage in the life cycle of a gravity current, where the initial energy has been largely dissipated and the density anomaly has been homogenized with the ambient fluid. During this phase, the front advances with a time scaling of $t^{1/5}$.

This progression of stages, from acceleration to slumping, to self-similar evolution, and finally to viscous decay, has been consistently documented in classical studies such as [72, 79, 34]. It provides a robust framework for interpreting both laboratory experiments and natural observations of gravity currents in diverse contexts.

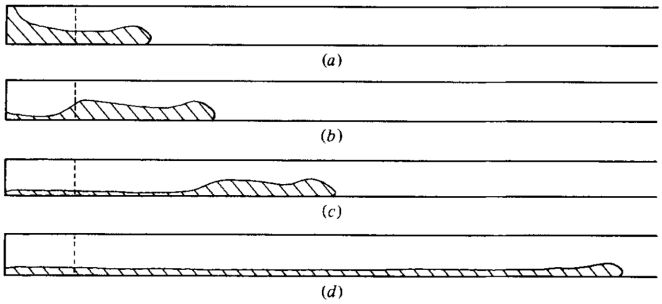

Figure 1: Schematic illustrations of the collapse of a finite volume of dense fluid at four successive times after release. Panel (a) shows the acceleration phase, panel (b) the slumping phase, panel (c) the self-similar phase, and panel (d) the viscous phase [72].

One of the central objectives of this dissertation is to investigate whether numerical simulations can faithfully reproduce these regimes under conditions of high Reynolds numbers, which are of relevant importance for realistic geophysical and engineering applications. High-Reynolds flows are notoriously challenging to model, as they involve intricate turbulence dynamics, multi-scale interac-

tions, and significant computational demands ([55]). Capturing the transition between the different phases of a gravity current in such regimes requires not only advanced numerical techniques but also careful validation against experimental data. The ability to simulate these flows with sufficient accuracy and reliability is essential for advancing our understanding of large-scale natural phenomena, such as river inflows, turbidity currents, and oceanic circulation, and for developing predictive tools applicable to engineering problems where buoyancy-driven flows play a critical role.

2.2 Turbidity currents

When density differences in a fluid are further enhanced by the suspension of sediment particles, the resulting phenomenon is known as a **turbidity current**, a type of sediment-laden gravity current (see Figure 2). Such flows are typically generated by the detachment of material from continental slopes and propagate down-slope along the seabed at velocities considerably higher than those of salinity-driven gravity currents [53].

River flood waves can also trigger powerful sediment-laden flows, transporting large volumes of sediment into lakes or coastal seas [28, 74, 83]. Turbidity currents are characterized not only by their density anomaly but also by their high velocity, which can reach several meters per second depending on slope and sediment concentration. Their elevated momentum allows them to maintain coherence over long distances, entraining additional material as they propagate.

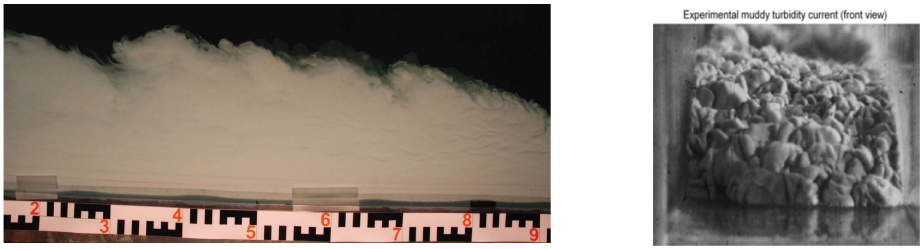

a) b)

Figure 2: Example of laboratory experiments on turbidity currents: a) lateral view [74], and b) frontal view [76].

The consequences of such dynamics are significant. Turbidity currents are highly erosive: the intense shear stresses they exert on the seabed can mobilize and transport vast quantities of sediment, reshaping the underwater landscape. Over geological timescales, repeated turbidity-current passages carve deep submarine canyons, which act as preferential pathways for subsequent flows. These canyons are among the most striking geomorphological features of continental margins, reflecting the cumulative impact of sediment-laden gravity currents.

From an engineering perspective, turbidity currents pose considerable risks to human infrastructure. Their combination of high velocity, sediment load,

and long runout can damage or sever submarine pipelines and communication cables, often laid across continental slopes and abyssal plains. Historical records [31] document several instances in which slope failures or river-flood-induced turbidity currents disrupted telecommunication networks and energy transport systems.

Thus, turbidity currents represent a dual phenomenon: they are both a primary agent of sediment transport and seabed morphology, shaping submarine canyons and depositional fans, and a source of hazard to anthropogenic structures. Their study is therefore essential for understanding sedimentary processes, marine geology, and for mitigating risks associated with human infrastructure in deep marine environments.

2.3 Hyperpycnal flows

Physically, a hyperpycnal flow occurs when a dense, sediment or salinity, laden plume is injected into a lighter ambient fluid, such as freshwater. In this configuration, the density contrast drives a gravity current along the bed, and the flow can be classified as a sediment-laden current, analogous to turbidity currents when significant sediment is present. At first, the dynamics are governed by inertia: the inflow advances along the surface with limited vertical exchange, maintaining a coherent front and decaying primarily along its lateral margins. This lateral spreading produces a characteristic triangular footprint at the free surface, whose planform narrows downstream as momentum weakens and the density contrast becomes progressively more influential. Within this inertial regime, interfacial shear between plume and ambient triggers Kelvin–Helmholtz billows along the lateral edges; these structures facilitate entrainment and induce secondary circulations [83, 5], including near-surface return flows that recirculate ambient water towards the centerline. The triangular surface pattern thereby acts as both a kinematic signature of lateral decay and a dynamical precursor of mixing-driven transformation (see Figure 3): as the plume loses momentum, dilution increases, and buoyancy forces associated with the density anomaly begin to dominate. The process reaches its critical stage at the plunging point, where the dense plume submerges beneath the free surface and reconfigures into a bottom- or intermediate-layer gravity current [57]. Downstream of plunging, the flow adopts the morphology of a density-driven undercurrent, undergoing further entrainment from above, interacting with bed roughness and slope, and organizing coherent vortical structures whose length scales are set by the interplay of shear, stratification, and geometric confinement. This conceptual behavior for laterally unconfined river inflows, lateral decay, triangular surface pattern, KH billows and return flow, followed by plunging, is articulated in Figure 3, which synthesizes the three-dimensional structure, planform evolution, and vertical transects highlighting convergence and recirculation zones that accompany the onset of submergence.

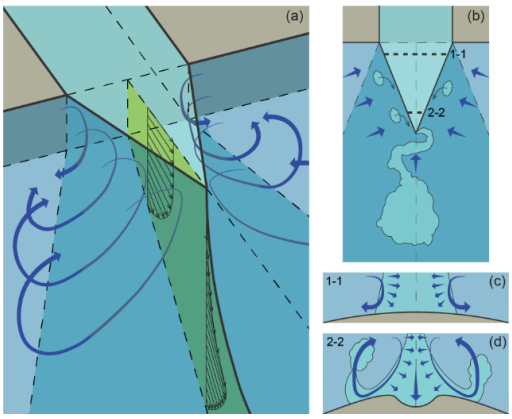

Figure 3: Conceptual model of a laterally unconfined, sediment-laden plunging river inflow. (a) 3D view. (b) Top view. (c) Lateral-vertical transect 1–1 near the river mouth. (d) Lateral-vertical transect 2–2 farther downstream. Transect locations are shown in (b), and longitudinal centerline velocity profiles for both sections are presented in (a) [83].

2.4 Dimensionless parameters for gravity current characterization

In order to characterize gravity-driven flows in a unified framework, a set of dimensionless parameters must be introduced, each of which highlights the relative importance of inertia, buoyancy, viscous forces, and geometric confinement. The first and most fundamental is the densimetric Froude number, which expresses the competition between the denser fluid momentum and the buoyancy forces induced by density differences. It is defined as

$$Fr_d = \frac{U}{u_b} \tag{1}$$

where the buoyancy velocity u_b is given by

$$u_b = \sqrt{g'H} \tag{2}$$

and the reduced gravity g' is

$$g' = \frac{g(\rho_1 - \rho_0)}{\rho_0} \tag{3}$$

with g the gravitational acceleration, ρ_1 the density of the heavier fluid, ρ_0 the ambient density, and H the characteristic plume thickness. This parameter is central, for example, for hyperpycnal flows, since it governs the onset of plunging and the subsequent transition from an inertial surface plume to a bottom-propagating gravity current.

A second parameter of general relevance is the Reynolds number, which quantifies the ratio between inertial and viscous forces:

$$Re = \frac{u_b H}{\nu} \tag{4}$$

where ν is the kinematic viscosity of the fluid. High values of Re indicate turbulent regimes, typical of geophysical currents, while lower values correspond to laminar or transitional flows. The Reynolds number is therefore necessary for assessing the dynamical regime of canonical gravity currents and for determining whether turbulence models or direct numerical resolution are required in simulations.

Another important aspect, for instance in the study of finite releases of dense fluid, is the volume, and in particular the associated potential energy. This aspect is often characterized through the geometric parameter known as the aspect ratio R.

$$R = \frac{H}{x_0} \tag{5}$$

where H is the denser volume height and x_0 its length. This ratio controls the initial release conditions, influencing the duration of the slumping phase and the scaling of the self-similar regime. In sediment-laden currents, R also determines the efficiency of downslope propagation and the degree of entrainment of ambient fluid. This parameter is widely used in lock-exchange analyses. Taken together, these dimensionless numbers, Fr_d, Re, and R, provide a coherent set of parameters for comparing different classes of gravity currents. Canonical currents are primarily described by Re, and their phase progression, turbidity currents in lock-exchange setups are governed by R and Re, hyperpycnal flows are controlled by Fr_d in combination with slope geometry and confinement. By employing these parameters, laboratory experiments and numerical simulations can be scaled consistently, ensuring similitude with natural phenomena and enabling a systematic identification of the dominant physical mechanisms across canonical, sediment-laden, and river-driven density flows.

3 Material and Methods

This chapter presents the mathematical models employed in the numerical experiments, together with the experimental setup used for the laboratory investigations. The latter includes a detailed description of the measurement techniques and data acquisition methods adopted during the experimental campaign.

3.1 Mathematical Model

3.1.1 Gravity Currents experiments

The gravity currents numerical cases are analyzed by solving the filtered Navier-Stokes equations in the Boussinesq form (continuity and momentum conservation, Eq. 6 and 7), together with a transport equation for a scalar, Eq. 8, salinity in this case. Within the LES framework, the governing equations are obtained by applying a spatial low-pass filter to the instantaneous conservation laws for mass, momentum, and energy. This filtering procedure separates the large, energy-containing eddies, which are explicitly resolved, from the smaller, subgrid-scale motions, which must be modeled. The resulting three-dimensional, unsteady filtered equations describe the dynamics of the resolved large-scale motions, while the influence of the unresolved turbulent scales enters through a subgrid-scale closure model. Figure 4 illustrates the distinction between the filtered velocity field $\tilde{u}_x$ and the instantaneous velocity u_x, highlighting the effect of the explicit filtering [91].

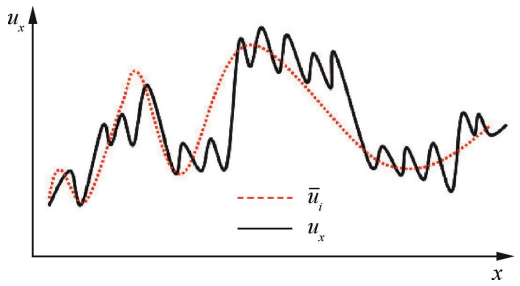

Figure 4: Difference between the filtered velocity and the instantaneous velocity ([91])

Within the LES framework, the governing equations can be written as follows:

$$\frac{\partial \bar{u_j}}{\partial x_j} = 0 \tag{6}$$

$$\frac{\partial \overline{u_i}}{\partial t} + \frac{\partial \overline{u_j u_i}}{\partial x_j} = -\frac{1}{\rho_0}\frac{\partial \bar{p}}{\partial x_i} + \frac{\partial}{\partial x_j}\left(\nu \frac{\partial \overline{u_i}}{\partial x_j}\right) - \frac{\rho'}{\rho_0} g \delta_{ij} - \frac{\partial \tau_{ij}}{\partial x_j} \tag{7}$$

$$\frac{\partial \bar{s}}{\partial t} + \frac{\partial \bar{u_j}\bar{s}}{\partial x_j} = \frac{\partial}{\partial x_j}\left(k_s \frac{\partial \bar{s}}{\partial x_j}\right) - \frac{\partial \lambda_j}{\partial x_j} \tag{8}$$

the over-bar ($\bar{\square}$) represents filtered values, u_i is the velocity component in the x_i direction, and direction 1, 2 and 3 correspond to x, y and z in a cartesian frame of reference. p is the hydrodynamic pressure and s is the salinity concentration, g is gravity, δ_{ij} is the Kronecker delta, the kinematic viscosity and the molecular diffusivity of the scalar s are ν and k_s, respectively. ρ' is the variation of density with respect to the reference value ρ_0, in isothermal conditions:

$$\rho = \rho_0[1 + \beta(s - s_0)] \tag{9}$$

where β is the salinity contraction coefficient, s_0 is the salinity concentration of the ambient fluid. τ_{ij} and λ_j in Eq. 7 and 8 are the SGS momentum and salinity fluxes, obtained by the following relations:

$$\tau_{ij} = -2\nu_t \bar{S_{ij}} \tag{10}$$

$$\lambda_j = -\kappa_t \frac{\partial \bar{s}}{\partial x_j} \tag{11}$$

where $\bar{S_{ij}}$ is the strain tensor of the solved stresses:

$$\bar{S_{ij}} = \frac{1}{2}\left(\frac{\partial \bar{u_i}}{\partial x_j} + \frac{\partial \bar{u_j}}{\partial x_i}\right) \tag{12}$$

the eddy viscosity, ν_t, and the eddy diffusivity, κ_t, are defined as:

$$\nu_t = C\Delta^2 \left|\bar{S}\right| \tag{13}$$

$$\kappa_t = C_s\Delta^2 \left|\bar{S}\right| \tag{14}$$

where

$$\left|\bar{S}\right| = \sqrt{2\bar{S_{ij}}\bar{S_{ij}}} \tag{15}$$

Δ denotes the characteristic LES filter width, typically associated with the local grid cell size. The constants C and C_s in Eq. 13 and 14 are evaluated using the WALE (Wall-Adapting Local Eddy-Viscosity) subgrid-scale model [22], which provides accurate near-wall behavior without the need for additional damping functions or dynamic procedures.

The Wall-Adapting Local Eddy-viscosity (WALE) model defines the subgrid-scale eddy viscosity through a formulation that naturally incorporates both strain and rotation effects of the smallest resolved turbulent structures. The model expression reads

$$\nu_t = (C_w\Delta)^2 \frac{\left(S_{ij}^d S_{ij}^d\right)^{3/2}}{\left(S_{ij}S_{ij}\right)^{5/2} + \left(S_{ij}^d S_{ij}^d\right)^{5/4}} \tag{16}$$

where Δ denotes the filter width, C_w is a constant typically of order 0.5 [22], and S_{ij} is the resolved strain-rate tensor defined as

$$S_{ij} = \frac{1}{2}\left(\frac{\partial u_i}{\partial x_j} + \frac{\partial u_j}{\partial x_i}\right) \tag{17}$$

The distinctive feature of the WALE model lies in the construction of the tensor S_{ij}^d, which represents the traceless symmetric part of the square of the velocity-gradient tensor. This tensor is defined so as to vanish in the case of pure shear and to reproduce the correct near-wall scaling of the eddy viscosity. Explicitly, it is written as

$$S_{ij}^d = \frac{1}{2}\left(\frac{\partial u_i}{\partial x_k}\frac{\partial u_k}{\partial x_j} + \frac{\partial u_j}{\partial x_k}\frac{\partial u_k}{\partial x_i}\right) - \frac{1}{3}\,\delta_{ij}\,\frac{\partial u_m}{\partial x_n}\frac{\partial u_n}{\partial x_m} \tag{18}$$

Through this definition, the WALE model succeeds in detecting regions of turbulence characterized either by strong strain or by strong rotation, while ensuring that the eddy viscosity vanishes in laminar shear flows and scales as y^3 in the vicinity of solid boundaries. This property is crucial for the correct representation of wall-bounded turbulence, since it avoids the need for ad hoc damping functions or dynamic adjustments of the model constant. The resulting formulation is therefore particularly well-suited for large-eddy simulations in complex geometries, where robustness and physical consistency of the subgrid-scale closure are essential.

A crucial advantage of the WALE formulation lies in its ability to reproduce the correct asymptotic behaviour of the eddy viscosity in the vicinity of solid boundaries. As shown by [22], the invariant $S_{ij}^d S_{ij}^d$ constructed from the traceless symmetric part of the squared velocity-gradient tensor scales as y^2 when the wall-normal coordinate $y \to 0$. This scaling directly implies that the eddy viscosity behaves as

$$\nu_t = \mathcal{O}(y^3),$$

which is consistent with the theoretical expectations for turbulent flows near walls. As emphasized by [70], the suppression of turbulent fluctuations in the viscous sublayer requires the subgrid-scale viscosity to vanish sufficiently rapidly as the wall is approached, in order to avoid artificial dissipation that would otherwise damp the near-wall streaks and compromise the correct reproduction of buffer-layer dynamics. The WALE model satisfies this requirement intrinsically, without relying on empirical damping functions. In contrast, the classical Smagorinsky model yields $\nu_t = \mathcal{O}(1)$ at the wall—a non-physical behaviour that results in excessive subgrid dissipation and, in many cases, in the relaminarization of channel or pipe flows unless the model constant is artificially reduced. The WALE formulation therefore constitutes a significant improvement in the modelling of wall-bounded turbulence, as it naturally enforces the correct near-wall scaling while retaining sensitivity to both strain and rotation rates of the

resolved field. This property is particularly advantageous in large-eddy simulations of complex geometries, where the absence of ad hoc damping functions enhances both the robustness and the generality of the closure.

The use of the WALE subgrid-scale model in the context of WF-LES has been extensively examined in the literature (see, for example, [82, 56]), as well as in more recent applications involving complex flows ([15, 19]).

The model is implemented in the OpenFOAM® environment, starting from the *buoyantBoussinesqPimpleFoam* solver. A finite-volume implementation of the governing equations is carried out implicitly, using the PISO algorithm [21]. The diffusive term is projected using the Euler-Implicit scheme to avoid the diffusive stability limit. The Schmidt number ($Sc = \nu/k_s$) is equal to 600, a reference value for salty water. At $t = 0$, the flow field is at rest in the domain.

3.1.2 Sediment-Laden flows

For the sediment transport simulations, an Eulerian–Eulerian two-phase flow formulation is employed to represent the coupled dynamics of a continuous fluid phase and a dispersed granular phase [30, 32]. The model, implemented in the *sedFoam* framework [11, 7], solves the volume-averaged conservation equations for mass and momentum [17, 36], treating both phases as interpenetrating continua. The fluid and particle phases occupy the volume fractions β and α, respectively, which satisfy the saturation constraint $\alpha + \beta = 1$.

Mass conservation for each phase is expressed as

$$\frac{\partial \alpha}{\partial t} + \nabla \cdot (\alpha \, \mathbf{u}^p) = 0 \tag{19}$$

$$\frac{\partial \beta}{\partial t} + \nabla \cdot \left(\beta \, \mathbf{u}^f\right) = 0 \tag{20}$$

where $\mathbf{u}$ denotes the phase-averaged velocity of fluid (superscript f) and granular (superscript p) phase.

Momentum conservation incorporates the effects of pressure gradients, gravitational body forces, viscous and turbulent stresses in the fluid phase, granular stresses in the particle phase, and interphase momentum exchange through drag. The corresponding momentum equations are:

$$\alpha\rho^p \frac{\partial \mathbf{u}^p}{\partial t} + \alpha\rho^p \left(\mathbf{u}^p \cdot \nabla\right) \mathbf{u}^p = -\alpha \nabla p + \nabla \cdot \boldsymbol{\tau}^p + \alpha\rho^p \mathbf{g} + \mathbf{f}_d \tag{21}$$

$$\beta\rho^f \frac{\partial \mathbf{u}^f}{\partial t} + \beta\rho^f \left(\mathbf{u}^f \cdot \nabla\right) \mathbf{u}^f = -\beta \nabla p + \nabla \cdot \boldsymbol{\tau}^f + \beta\rho^f \mathbf{g} - \mathbf{f}_d \tag{22}$$

where p is the shared pressure field, $\mathbf{g}$ is the gravitational acceleration, $\boldsymbol{\tau}^k$ is the stress tensor of phase $k = f, p$, and $\mathbf{f}_d$ is the drag force per unit volume.

The fluid-phase stress tensor $\boldsymbol{\tau}^f$ combines molecular and turbulent contributions via an effective viscosity $\nu^f_{\text{eff}} = \nu^f + \nu_t$, where ν^f is the kinematic viscosity and ν_t the turbulent eddy viscosity:

$$\boldsymbol{\tau}^f = 2\,\beta\rho^f \, \nu^f_{\text{eff}} \, \mathbf{D}^f \tag{23}$$

$$\mathbf{D}^f = \frac{1}{2}\left(\nabla \mathbf{u}^f + (\nabla \mathbf{u}^f)^{\mathrm{T}}\right) \tag{24}$$

The granular-phase stress tensor $\boldsymbol{\tau}^p$ accounts for collisional, kinetic, and enduring-contact contributions:

$$\boldsymbol{\tau}^p = -p^p \mathbf{I} + 2\,\alpha\mu_p\,\mathbf{D}^p \tag{25}$$

$$\mathbf{D}^p = \frac{1}{2}\left(\nabla \mathbf{u}^p + (\nabla \mathbf{u}^p)^{\mathrm{T}}\right) \tag{26}$$

where p^p is the granular pressure and μ_p the granular viscosity. The constitutive models defining p^p and μ_p derive from kinetic theory in dilute conditions and from dense granular rheology as α approaches the maximum packing value $\alpha_{\max}$ [11]. A contact-pressure term, diverging near $\alpha_{\max}$, is included to prevent unphysical particle overpacking.

Interphase momentum exchange is modeled using a hindered-settling drag law:

$$\mathbf{f}_d = \beta^{-h_{\exp}}\,K\,\left(\mathbf{u}^f - \mathbf{u}^p\right) \tag{27}$$

where K is the Schiller–Naumann drag coefficient for isolated spheres [73], modified through the exponent $h_{\exp}$ to account for crowding effects in dense suspensions. Turbulent suspension is additionally represented by a drift flux term proportional to the concentration gradient,

$$\mathbf{j}_t = -\frac{\nu_t}{\mathrm{Sc}_t}\,\nabla\alpha \tag{28}$$

where Sc_t is the turbulent Schmidt number. This flux contributes to the particle-phase transport by enhancing turbulent mixing [30].

Together, Eq. 20 and 27 define the two-phase continuum model adopted in this work. This formulation enables the simulation of sediment-laden flows across a wide range of regimes, including dilute turbulent suspensions and dense granular transport, while maintaining both numerical stability and physical fidelity.

3.1.3 wall-functions

Compared to DNS, the LES approach, which explicitly resolves only the energy-containing turbulent scales, significantly reduces the required mesh resolution while still providing accurate predictions for many practical flows ([68]). However, in the near-wall region ($y^+ < 11$, with $y^+ = yu_\tau/\nu$, where u_τ is the friction velocity and y is the wall-normal coordinate), the flow is dominated by small, highly energetic structures that must be directly resolved to capture the steep gradients and intense shear typical of this layer. As a result, LES in this region behaves as a quasi-DNS, leading to prohibitive computational costs at high Reynolds numbers.

The structure of the near-wall flow is well described in classical turbulence theory ([70, 44]). Immediately adjacent to the wall, as illustrated in Figure 5, the

viscous sublayer ($y^+ \lesssim 5$) is characterized by a linear velocity profile, $u^+ = y^+$, where viscous effects dominate. Above it, in the buffer layer ($5 \lesssim y^+ \lesssim 30$), both viscous and turbulent stresses contribute, and the flow exhibits strongly anisotropic and intermittent structures. Farther from the wall, the logarithmic region is established, where the mean velocity profile follows the classical log-law,

$$u^+ = \frac{1}{\kappa} \ln\left(y^+\right) + B \tag{29}$$

with the von Kármán constant $\kappa \approx 0.41$ and $B \approx 5.0$.

The treatment of the near-wall region through numerical experiments is computationally demanding. Nevertheless, several methodologies have been developed to reduce the associated costs, as extensively discussed in the reviews by [67] and [68]. In particular, Piomelli (2008) classifies these approaches into three broad categories: equilibrium-stress models, zonal approaches, and hybrid RANS/LES methods (where RANS stands for the Reynolds-averaged Navier–Stokes equations). The first approach, which has been adopted in the present thesis for the resolution of the selected test cases, considers the near-wall region and the outer layer separately. In this framework, the centroid of the first off-wall cell is assumed to lie within the logarithmic region of the mean velocity profile. At this location, the shear stress is imposed according to the log-law, and this value is subsequently employed as a boundary condition for the computation of the stress in the outer layer (i.e., a prescribed constraint applied at the domain boundary that defines the behaviour of the flow variables, such as velocity or stress, at that location) . Thus, the two regions are treated independently, with the wall stress prescribed from the equilibrium assumption and the outer flow resolved by LES. The zonal approach, on the other hand, relies on simplified models (typically RANS) to represent the near-wall region, while the outer layer is simulated using LES. These two models are weakly coupled: the near-wall RANS calculation provides the shear stress required by the LES, whereas the LES solution supplies the boundary conditions for the RANS equations. This bidirectional exchange allows the two descriptions to coexist, albeit with limited interaction. Finally, hybrid RANS/LES methods treat the near-wall region directly with a complete RANS model, while the outer layer is resolved by LES. In this case, the coupling is strong and is achieved through blending functions or by modifying the characteristic length scale of the turbulence model. Such methods aim to ensure a smooth transition between the RANS and LES regions, mitigating inconsistencies in the representation of the logarithmic layer and improving the robustness of the simulation at high Reynolds numbers.

Because the correct prediction of these near-wall layers requires very fine resolution, wall-functions are commonly employed to relieve the computational burden. These models reconstruct the momentum transfer within the unresolved near-wall region using semi-empirical laws derived from the structure of the wall-bounded turbulent boundary layer (i.e., the thin region adjacent to the wall where viscous effects dominate and velocity gradients are highest, controlling shear and momentum exchange with the outer flow). Wall-function methodology originated within the RANS framework and has since been successfully extended

to LES ([67]). Although wall-functions are traditionally employed in RANS models, since they are derived from mean velocity profiles, they can also be used in LES under appropriate grid conditions. In LES, even though the wall-function is evaluated instantaneously, if the first off-wall cell is placed within the logarithmic layer and made sufficiently coarse, it represents a locally averaged flow rather than fully resolved instantaneous near-wall dynamics. As a result, the wall-function remains consistent with the underlying assumptions of LES in wall-modeled configurations, where only the outer flow is resolved and the inner layer is parameterized.

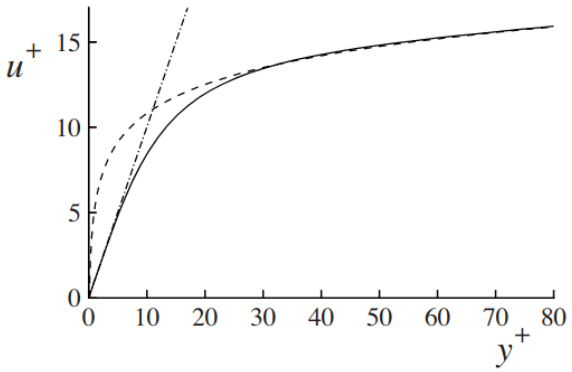

Figure 5: Near-wall profiles of mean velocity: solid line, DNS data of [40]: Re = 13,750; dot–dashed line, u+ = y+; dashed line, the log law. ([70])

In the present work, three wall-function formulations are considered. The first two, the Spalding law-of-the-wall-function ([80]) and a blended formulation ([80, 54]), impose constraints on the near-wall eddy viscosity ν_t to ensure consistency with the expected mean velocity profile. In many practical applications, it is desirable for the wall-function to reproduce the entire near-wall behaviour, including the viscous sublayer, the buffer layer, and the logarithmic region. Both the Spalding and blended models provide such a complete representation, making them suitable for cases where a unified profile across all wall-adjacent layers is required. The third one, the Jayatilleke wall-function ([37]), instead models the eddy diffusivity, making it suitable for heat and mass transfer in addition to momentum exchange.

In particular, the Spalding wall-function is based on the relation:

$$y^+ = u^+ + \frac{1}{E}[exp(ku^+) - 1 - ku^+ - 0.5(ku^+)^2 - \frac{1}{6}(ku^+)^3] \tag{30}$$

where $u^+ = u/u_\tau$ is the dimensionless velocity near the wall, k is equal to 0.41, and E is the wall roughness parameter, set as 9.8 for smooth walls. Then, the total viscosity, the sum of the molecular and the turbulent components, is calculated as a function of y^+ as:

$$\nu_{tot} = \frac{u_\tau y}{\frac{1}{k}\ln Ey^+} = \frac{y^+\nu}{\frac{1}{k}\ln Ey^+} = \nu_t + \nu \tag{31}$$

assuming that the molecular viscosity is proportional to the eddy viscosity:

$$\nu_t = \nu\left(\frac{ky^+}{\ln Ey^+} - 1\right) \tag{32}$$

The Blended wall-function uses a different approach for the calculation of y^+:

$$y^+ \ln Ey^+ - \frac{kyu_{wall}}{\nu} = 0 \tag{33}$$

where u_{wall} is the velocity in the first off-wall cell. ν_t is expressed as a function of u_τ in the following way:

$$\nu_t = max\left(0, \frac{u_\tau^2}{|\nabla u| + \zeta} - \nu\right) \tag{34}$$

where ζ is a parameter to avoid the floating number exception during the solver run. u_τ is dependent on y^+, as:

$$\begin{cases} u_\tau = (u_{\tau_{vis}}^n + u_{\tau_{log}}^n)^{\frac{1}{n}} \\ u_{\tau_{vis}} = \dfrac{u_{wall}}{y^+} \quad y^+ < 30 \\ u_{\tau_{log}} = k\dfrac{u_{wall}}{\ln Ey^+} \quad y^+ > 30 \end{cases} \tag{35}$$

where $u_{\tau_{vis}}$ is the friction velocity computed by the viscous sublayer assumptions, $u_{\tau_{log}}$ is the friction velocity computed by the inertial sublayer assumptions, and n is a blending exponent.

Finally, the Jayatilleke wall-function models the eddy diffusivity. It is based on the calculation of the scalar flux near the wall:

$$\begin{cases} s_{flux} = \rho k_t(\frac{s_{wall}-s_p}{y}) \quad y^+ > y_L^+ \\ s_{flux} = \frac{(s_{wall}-s_p)(\rho u_\tau)}{Sc_t(\ln Ey^+ + P_j)} \quad y^+ < y_L^+ \end{cases} \tag{36}$$

where y_L^+ is a threshold value, denoting the intercept between the linear part of the scalar profile and the logarithmic part, dependent on the turbulent Schmidt number($Sc_t = \nu_t/k_t$). s_{wall} and s_p are the salinity concentrations respectively at the wall and out of it. P_j is a parameter of the Jayatilleke model, calculated using the following relation:

$$P_j = 9.24\left[\left(\frac{Sc}{Sc_t}\right)^{\frac{3}{4}} - 1\right]\left[1 + 0.28e^{-0.007(Sc/Sc_t)}\right] \tag{37}$$

By comparing the two s_{flux} equations, it is possible to estimate the eddy diffusivity coefficient k_t.

The three models exposed in this chapter will be implemented in the study cases later exposed, to decrease the computational costs for high Re simulations.

3.2 Hyperpycnal flows: Experimental Setup

The experimental setup was developed and validated at LEGI on the Coriolis platform [50]. This facility is equipped with advanced technical installations and state-of-the-art measurement systems. Its large diameter (13 m) and basin area (130 m^2) are sufficient to reproduce the turbulent flow and mixing processes occurring at the Rhône–Lake Geneva interface while minimizing scale effects. Figure 6 illustrates the typical configuration of the Coriolis platform used in the present experiments.

The facility includes an inlet channel approximately 2.9 m long, with a variable width among the four experiments (0–W section in Figure 6). The channel is connected to two inlet pipes supplying a controlled discharge of saline water. Water is provided from external tanks, which are used both to fill the Coriolis platform and to feed an overhead reservoir (both not shown in Figure 6). The discharge is regulated and monitored through a LEGI proprietary Graphic User Interface (GUI). The flow exits the channel onto an inclined platform with a slope of approximately 8°, a length of 5.0 m, and a width of 8.0 m.

To ensure a uniform streamwise velocity profile at the channel outlet, flow-homogenization devices are installed upstream of the channel entrance. These consist of a combination of rolled plastic meshes, grids, a 0.5 m-thick honeycomb, coconut fibers, and hollow cylindrical tubes with a diameter of 2 cm (see Figure 6). Flow uniformity is assessed using an ADV, which traverses the channel width at a depth of 1.5 cm below the free surface. At each location, 10 s stationary velocity measurements of the three components (u, v, w) are recorded. The ADV transect spans only part of the channel width: 1.0 m, 0.9 m, 0.57 m, and 0.3 m for channel widths of 2.0 m, 1.0 m, 0.67 m, and 0.4 m, respectively. Several outlet drain pipes with diameters of 0.2 m and 0.1 m are distributed along the bottom of the platform to evacuate water. The different channel widths are implemented using a 4 m-long horizontal inlet channel positioned 0.68 m above the tank bottom. This channel transitions smoothly along a curved section starting 25 cm before the end of the straight reach and is centered on the inclined plate (5 m × 8 m), which reproduces the 8° bottom slope of the Rhône River inflow into Lake Geneva.

Flow illumination is provided by a 25 W Yttrium Aluminum Garnet (YAG) laser operating at a wavelength of 532 nm. PIV measurements are performed using two PCO cameras (Pioneer in Cameras and Optoelectronics) for vertical sections and one MX-25 camera (WESCAMS surveillance series) for horizontal sections, which are scanned successively.

Figures 7 and 8 show the horizontal and vertical slices from which the data were extracted for the analysis of each case study. The following sections report only the results from the surface horizontal slice and from the vertical slice taken

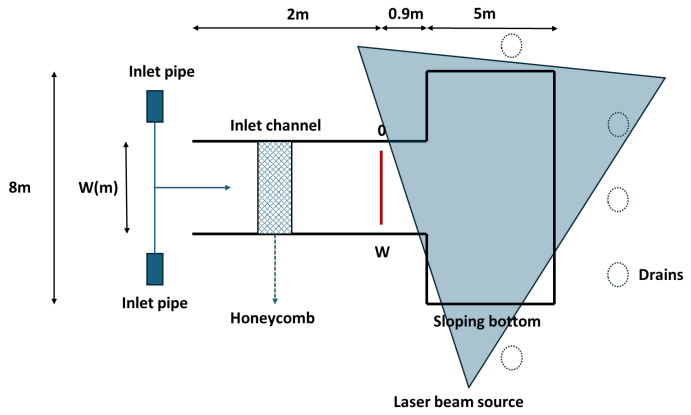

Figure 6: Sketch of the experimental setup for the saline plumes.

at the channel centre for each case. These two slices were selected because they provide the most informative view of the plunging dynamics.

The platform is equipped with state-of-the-art PIV instrumentation for velocity measurements, including laser scanners, PCO cameras, and MX-25 cameras. The PCO cameras used for vertical longitudinal measurements in the Ex-V configuration are equipped with a Camera Link interface, enabling software control of the lenses. They were operated at an acquisition frequency of 20 Hz with an exposure time of 20 ms. In this configuration, the laser sheets were oriented perpendicular to the inlet channel. In contrast, the MX-25 camera was employed for high-definition plan-view measurements in the Ex-H configuration, with laser sheets aligned parallel to the channel. Flow illumination was provided by a Yttrium Aluminum Garnet (YAG) laser. To ensure accurate particle tracking, the water was seeded with ORGASOL micro-particles. These tracer particles have a density nearly equal to that of the ambient water, minimizing buoyancy effects and allowing them to closely follow the fluid motion. Data post-processing was carried out using the UVMAT MATLAB toolbox. The resulting velocity fields were interpolated onto a regular grid with a spatial resolution of 0.25 cm $\times$ 0.25 cm for the vertical setup and 0.72 cm $\times$ 0.72 cm for the horizontal configuration.

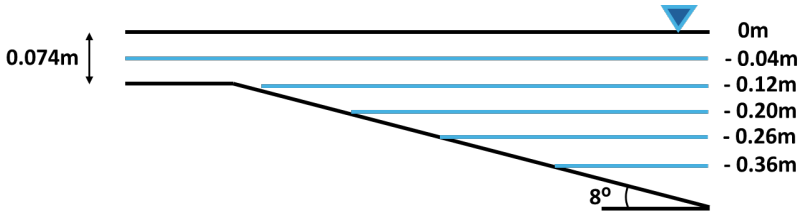

Figure 7: PIV laser positions and spacing, horizontal slices.

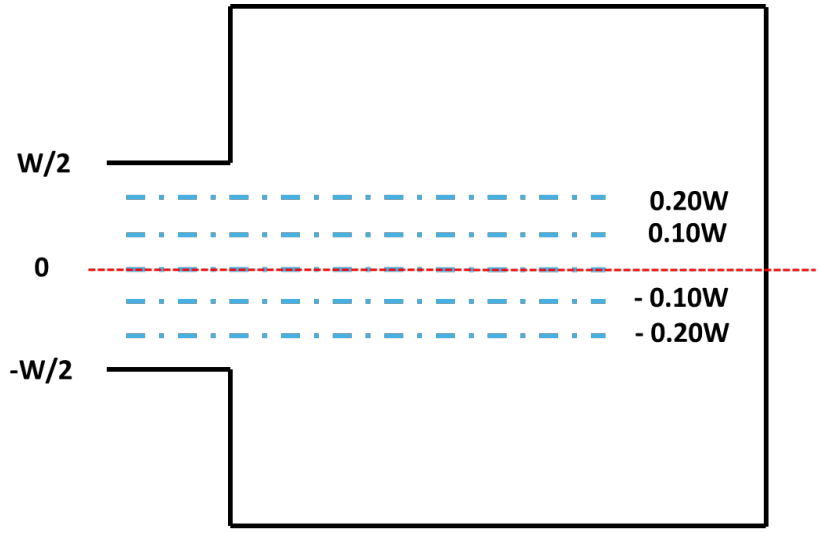

Figure 8: PIV laser positions and spacing, vertical slices.

4 Study Cases and Quality assessment

4.1 Gravity currents in lock-exchange

The analysis to verify the wall behavior of a gravity current and the potential advantage of using coarse grids was conducted on the lock-exchange configuration, see Figure 9. The domain is a box of height H and length L, with a partition wall at a distance x_0 from the left wall, which separates two fluids of different densities.

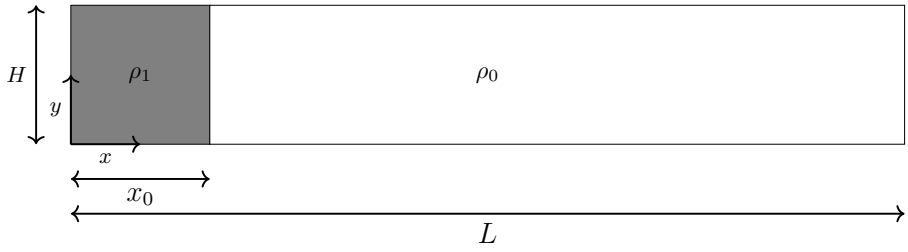

Figure 9: Lock-exchange configuration.

When the partition is removed, due to the horizontal pressure gradient, a flow is triggered, causing the denser fluid ρ_1 on the left side of the wall to move along the bottom relative to the surrounding fluid with ambient density ρ_0. The possible configurations are characterized in terms of aspect ratio R, reduced gravity g' and the Reynolds number, already defined in Section 2, Eq. 4 and 5. The Schmidt number is equal to 600, a reference value for salty water. At $t = 0$, the flow field is at rest in the domain.

This type of case study is commonly used to analyze the physics of gravity currents through numerical simulations and experiments (see, among others, [84, 63, 65, 35]).

Initially, a validation phase of the mathematical model presented in Section 3.1.1 is carried out using a benchmark case. The comparison is performed against the results reported in [63], where experimental and WR-LES simulation was reported. The selected benchmark corresponds to the Ottolenghi-FR case (where FR denotes Fully Resolved), which adopts the same physical and geometrical parameters as RUN2 and EXP2 in the reference study. Specifically, the governing parameters are $R = 2$, a reduced gravity $g' = 0.29\text{m/s}^2$, computed in the present work assuming densities $\rho_1 = 1030\text{kg/m}^3$ and $\rho_0 = 1000\text{kg/m}^3$, and a buoyancy velocity $u_b = 0.24\text{m/s}$, yielding a Reynolds number of $Re = 48{,}522$. Additional details of the validation setup are summarized in Table 1.

Subsequently, a series of additional simulations is carried out using wall-resolved configurations and the WALE turbulence model, to gain deeper insight into the near-wall flow behavior as a function of both the reduced gravity g' and the flow depth H. Based on the validation results, this analysis aims to assess whether a well-developed and stable boundary layer is established, thereby pro-

viding a physical justification for the subsequent application of wall modeling approaches. The main geometrical and physical characteristics of the additional simulations are summarized in Table 2, where they are presented alongside the validation case Ottolenghi-FR (G3H1) for comparison. In particular, the configuration with increased domain height is later employed to support the validation of the wall-modeling strategy (G3H2 in Table 2, later renamed HR-FR).

The grid spacing used for the validation phase and boundary characterization is $\Delta x = 0.01H$ and $\Delta z = 0.016H$, while Δy varies from $0.01H$ at the center of the domain to $0.002H$ near the boundaries. This grid configuration is consistent with the numerical experiments reported by [63]. From a posteriori analysis, using the time-dependent maximum wall shear stress during the evolution of the gravity current, it was possible to obtain $\Delta x^+ = 50$, $\Delta z^+ = 20$, while $\Delta y^+ = 1$ at the bottom, ensuring a correct solution of the viscous layer.

Table 1: Cases for validation.

Case	LxHxd [m]	*mesh resolution*	*LES model*
Ottolenghi et al. 2016	4.096x0.2x0.2	2048x128x64	*dynamicSGS*
Ottolenghi-FR	4.096x0.2x0.2	2048x140x64	*waleSGS*

The application of wall-functions requires a particularly coarse grid in all directions in terms of wall units, as discussed in [67]. At the same time, an adequate number of points along the wall-normal direction is necessary to properly resolve the boundary layer and the mixing ([9]). Therefore, the case used for validation, characterized by a low Reynolds number, does not allow the validation of wall models. To overcome these issues, the configuration of the HR-FR case (see Table 3) was considered. In this setup, the higher Reynolds number results from the elevated potential energy, which is later converted into kinetic energy after the lock release. This adjustment brings the test case closer to the real scale of the phenomenon (with Re on the order of 10^5, [55]) and is more suitable for wall modeling. The decision to modify the domain characteristics rather than the viscosity was made to allow potential future comparisons with experimental setups.

The new reference case HR-FR was performed at $Re_b = 136000$. The study by [66] presents, in the context of large-eddy simulation, an analysis of grid requirements for gravity currents generated by a lock-exchange configuration over a flat bottom. In particular, the authors simulate a case characterized by

Table 2: Cases for the boundary layer characterization.

Case	LxHxd [m]	*mesh resolution*	$g'[m/s^2]$	H [m]	*Re*
G1H1	4.096x0.2x0.2	2048x140x64	0.075	0.2	24495
G2H1	4.096x0.2x0.2	2048x140x64	0.150	0.2	34641
G3H1	4.096x0.2x0.2	2048x140x64	0.290	0.2	48166
G4H1	4.096x0.2x0.2	2048x140x64	0.590	0.2	68702
G1H2	4.096x0.4x0.2	2560x200x92	0.075	0.4	69282
G3H2	4.096x0.4x0.2	2560x200x92	0.290	0.4	136000

$Re_{b,H/2} = 60000$, where in the definition of both the Reynolds number and the bulk velocity, the characteristic length scale is taken as $H/2$. The finest grid employed in the study consists of 3150, 185, and 200 cells in the x, y, and z directions, respectively. The case analyzed herein, rescaled using $H/2$, yields $Re_{b,H/2} = 48166$, which is of the same order of magnitude as the previously cited case. A computational grid with a resolution of 2560, 200, and 92 cells in the x, y, and z directions, respectively, is employed. Considering the computational domain adopted, this resolution is greater than, or at least comparable to, that used in [66].

Accordingly, wall-modeled cases (denoted as WM) were simulated on a coarser grid using the same lock-exchange configuration, while employing the wall-modeling approaches described in Section 3.1.3. The details of the simulations are provided in Table 3. The HR-NR case refers to a simulation performed without wall resolution or wall-functions, to highlight the role of the adopted models.

Table 3: Cases for wall-model validation.

Case	LxHxD [m]	*mesh resolution*	u_b [m/s]	*Re*	*Wall approach*
HR-FR	4.096x0.4x0.2	2560x200x76	0.34	136000	*wall resolved*
HR-NR	4.096x0.4x0.2	1024x100x48	0.34	136000	*not resolved*
HR-WM-J	4.096x0.4x0.2	1024x100x48	0.34	136000	*Jayatilleke Wall Model*
HR-WM-S	4.096x0.4x0.2	1024x100x48	0.34	136000	*Spalding Wall Model*
HR-WM-B	4.096x0.4x0.2	1024x100x48	0.34	136000	*Blended Wall Model*

As shown in Table 3, the number of cells in the coarse grids cases is reduced by approximately 90% compared to the fully resolved simulations, passing from about 39 millions of cells to about 5 millions, with a significant reduction of the computational time (from about 10^2 hours (h) of the HR-FR case to 10^0 h of the HR-WM-S case, with 320 processors implied for both cases). To complete the study, additional cases, not reported in Table 3, have been analyzed, varying the grid resolutions in the x, y and z directions. These cases will be further referred to in Section 4.4.

4.2 Sediment-laden flows in lock-exchange

Compared with the configuration analyzed in the previous section, the present case considers the presence of a cylindrical structures located on the bottom boundary. This setup is intended to provide an idealized representation of subsea pipelines or cables, which are frequently exposed to and potentially damaged by the action of the investigated currents. To this end, a lock-exchange configuration was adopted to reproduce the laboratory experiment illustrated in Figure 10. Within this framework, both saline and turbidity currents were examined. For the saline cases, the numerical results were validated through direct comparison with the available experimental data, thereby enabling a quantitative assessment of the accuracy and reliability of the simulations.

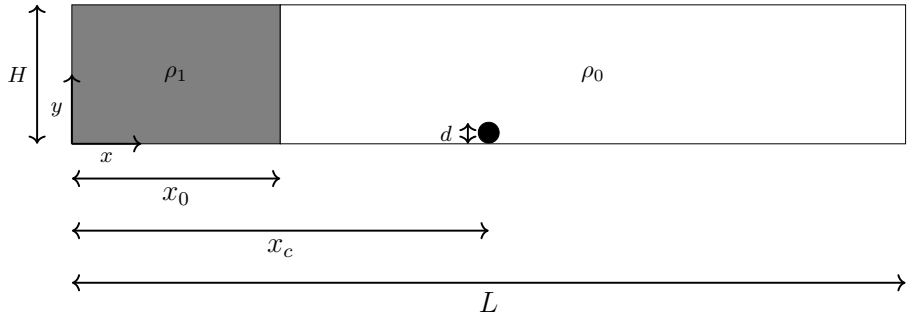

Figure 10: Lock-exchange configuration, with a cylinder settled at the domain bottom.

The main geometrical and physical characteristics are summed in Table 4.

Table 4: Geometrical characteristics of the experimental case

LxHxD [m]	x_0 [m]	x_c [m]	d [m]
3x0.27x0.2	0.3	$2.5x_0$	0.025

In this configuration, laboratory experiments were performed assuming a freshwater density of $\rho_0 = 1000$ kg m^{-3} and a saline-solution density of $\rho_1 = 1006$ kg m^{-3}. This yields a reduced gravity of $g' \approx 0.059$. Assuming $H_0 = 0.27$ m, the associated buoyancy velocity is $u_b \approx 0.126$ m s^{-1}, while the reference Reynolds number is $Re \approx 3.4 \times 10^4$, computed using a kinematic viscosity $\nu = 1.0 \times 10^{-6}$ m^2/s. These values indicate that the flow lies in a fully turbulent regime, for which LES modelling is appropriate.

From a numerical standpoint, three simulations were conducted, as summarized in Table 5. The first simulation, RUN 1 – B, reproduces the laboratory experiment using the modeling framework described in Section 3.1.1, which is based on a modified version of the *buoyantBoussinesqPimpleFoam* solver. This run serves as the baseline case for comparison with experimental measurements.

The second simulation, RUN 2 – S, is designed to model a turbidity current characterized by the same fundamental governing parameters as RUN 1 – B. In this case, the *SedFoam* solver is employed, implementing the sediment-transport model described in Section 3.1.2. This approach enables an additional validation of the *SedFoam* framework against the available experimental data. While the overall density contrast between the current and the ambient fluid is preserved, within the *SedFoam* formulation this contrast is not imposed through salinity; instead, it is achieved by introducing solid particles with density $\rho_s = 1100$ kgm^{-3}, diameter $d = 2 \times 10^{-5}$ m, shape factor equal to 0.85, and a volumetric concentration of 6%. Owing to the relatively low sediment concentration and density contrast, this configuration is therefore referred to as a low-concentration turbidity current.

The third simulation, RUN 3 – T, also relies on the *SedFoam* solver and is intended to represent a fully developed turbidity current. In this configuration, the mixture density is set to $\rho_1 = 1180$ kgm^{-3}. This value is obtained by prescribing a 11% volumetric concentration of solid particles with density $\rho_s = 2650$ kgm^{-3}, particle diameter $d_p = 2 \times 10^{-4}$ m, and shape factor equal to 0.85. Within *SedFoam*, the shape factor accounts for particle non-sphericity in the definition of sediment geometry and the associated drag properties.

Table 5: Characteristic parameters of the three numerical simulations considered.

Case	Current	Solver	$\Delta\rho$ [kg/m^3]	g' [m/s^2]	u_b [m/s]	Re
RUN 1 - B	Saline	*buoyantB..*	6	0.059	0.126	34020
RUN 2 - S	Low-concentration turbidity	*SedFoam*	6	0.059	0.126	34020
RUN 3 - T	Turbidity	*SedFoam*	180	1.770	0.690	186300

4.3 Hyperpycnal flows experiments

The laboratory experiments are designed to reproduce the inflow of a river into a larger basin, such as a lake (see Figure 11). Specifically, the experimental setup was built using the inflow of the Rhône River into Lake Geneva as the field-scale prototype, for which comprehensive data are readily available from the FOEN-operated measurement station at Porte du Scex (Swiss Federal Office for the Environment, https://www.hydrodaten.admin.ch/de/2009.html), located approximately 6 km upstream of Lake Geneva (see Figure 11c). Further details of the inlet geometry and flow conditions are as follows: inlet width $W_0 = 126$ m, inlet water depth $H_0 = 4.4$ m, inlet aspect ratio $W_0/H_0 = 28.6$, and inflow densimetric Froude number $\mathrm{Fr}_{d,0}$ in the range 3.98–4.08 (see [83]).

The laboratory experiments and numerical simulations reproduce a scaled version of the Rhône–Lake Geneva system. Flow conditions are scaled according to Froude similarity, and the geometry is reduced by a factor of 1:60, resulting in an aspect ratio of 27, representative of the actual inflow at Lake Geneva. The experiments are designed to isolate and examine the specific influence of

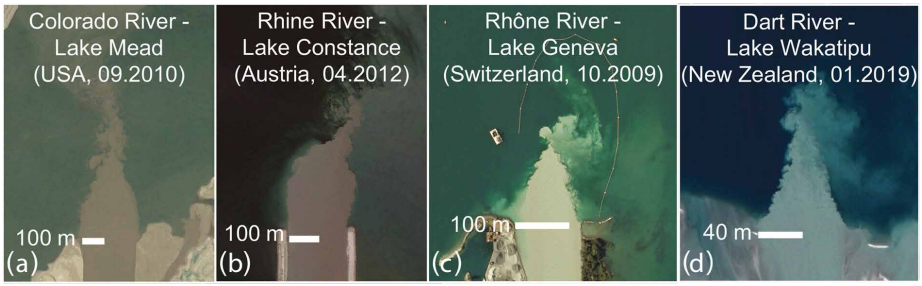

Figure 11: Field examples of unconfined hyperpycnal river plumes [83].

the inflow aspect ratio while keeping other key parameters constant, namely the densimetric Froude number $\mathrm{Fr}_{d,0}$, the inflow velocity U_0, and the inflow depth H_0. Table 6 summarizes the main characteristics of the laboratory experiments. Minor variations in the flow parameters are observed, which are typical of laboratory conditions.

The four experimental classes, distinguished by different inlet channel widths, were designed to investigate how variations in inflow geometry influence the subsequent evolution of the current after it enters the tank, where the flow may be considered unbounded. This approach allows the specific role of inlet width to be isolated and its impact on the governing physical processes to be assessed, with particular attention to the mixing-layer zone and the plunging region. These areas are of primary importance, as they regulate entrainment, shear-layer development, and the onset of turbulence, all of which are strongly affected by the inflow conditions. By systematically varying the inlet width while keeping the remaining flow parameters comparable, the experiments provide a consistent framework to evaluate how geometric differences at the source propagate downstream and shape the overall dynamics of the unbounded current.

The analyzed cases are summarized in Table 6, which reports the inlet channel width and the PIV configuration (V for vertical and H for horizontal measurements). Here, Q_0 denotes the inlet discharge, U_0 the mean inlet streamwise velocity, H_0 the inlet water depth, H_{tot} the total water depth in the Coriolis tank, W_0 the inlet channel width, and $\mathrm{Fr}_{d,0}$ the inflow densimetric Froude number.

Table 6: Summary of investigated conditions.

Case	H_0 [m]	W_0/H_0	Q_0 [m^3/s]	U_0 [m/s]	ρ_0 [kg/m^3]	ρ_a [kg/m^3]	$\Delta\rho_0$ [kg/m^3]	$\mathrm{Fr}_{d,0}$
2-H	0.074	27.0	0.018	0.12	1000.8	999.5	1.30	3.96
2-V	0.074	27.0	0.018	0.12	1002.7	1001.6	1.10	4.40
1-H	0.074	13.5	0.009	0.13	1001.7	1000.7	1.00	4.75
1-V	0.074	13.5	0.010	0.14	1002.0	1001.0	1.00	5.23
0.67-H	0.074	9.0	0.005	0.10	1002.2	1001.2	1.00	3.54
0.67-V	0.074	9.0	0.005	0.11	1002.1	1001.1	1.00	4.04
0.4-H	0.074	5.4	0.004	0.13	1002.2	1001.3	0.90	4.96
0.4-V	0.074	5.4	0.004	0.13	1002.5	1001.4	1.10	4.49

4.4 Spatial and Temporal Quality Assessment

Before analyzing the results, a set of preliminary assessments is conducted to evaluate the grid quality and the temporal independence of the numerical solutions.

4.4.1 Gravity currents in lock-exchange assessment

For the cases presented in Section 4.1, the analyses are carried out for the most demanding case among those listed in Table 2, namely the G3H2 configuration, which corresponds to the highest Reynolds number considered in this study.

To assess grid independence, several mesh resolutions are tested in all three spatial directions, as summarized in Table 7. The selection of the tested resolutions is also guided by the recommendations provided by [66], who offer specific guidelines on the mesh requirements necessary to achieve WR-LES in high-Reynolds-number gravity current simulations.

Table 7: Grid resolution.

x direction		**y direction**		**z direction**	
nx1	1536	ny1	160	nz1	64
nx2	2048	ny2	200	nz2	76
nx3	2560	ny3	–	nz3	92

Figure 12 shows the front evolution x_f for different grid resolutions, as indicated in the legend. The results appear similar, albeit with slight differences in the self-similar phase. Regarding the horizontal resolution, the case with nx1=1536 tends to be faster than the other cases. The latter, with resolutions in the x direction of nx2=2048 and nx3=2560, are comparable to, or even higher than, those used in [66], and exhibit differences, which can be attributed to the resolution adopted in the z direction, with the front slowing down as the spanwise resolution increases. In particular, the case with nz3=92 is consistent with that employed in [66] for the most refined grid.

With respect to vertical resolution, a posteriori analysis of the results revealed that both adopted vertical resolutions, ny1=160 and ny2=200, yield, on average, a first computational node located at a wall-normal distance of approximately y^+=1. However, the ny2=200 resolution ensures that, on average, the first 3–4 cells from the wall lie within the viscous sublayer (y^+<5), which constitutes an optimal condition for a WR-LES. Refer to Figure 13, which presents, in non-dimensional form, the linear velocity profile of the law of the wall and, at selected characteristic times, the streamwise velocity profiles along the wall-normal direction, averaged in the spanwise direction and over an ensemble of profile within the head of the current.

An additional test was also conducted using a grid with a vertical resolution of ny3 = 240. A posteriori analysis, performed after a few seconds of simulation, revealed that this resolution resulted in a number of points within the viscous sublayer ($y^+ < 5$) exceeding even the requirements for a Direct Numer-

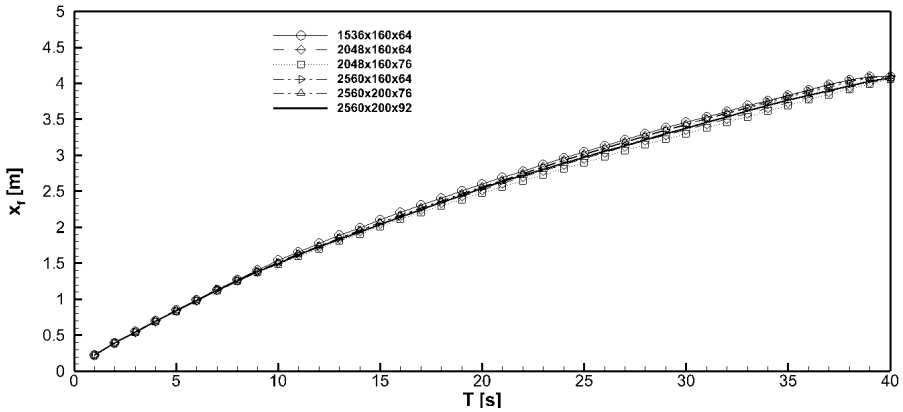

Figure 12: Front evolution in time for different grids.

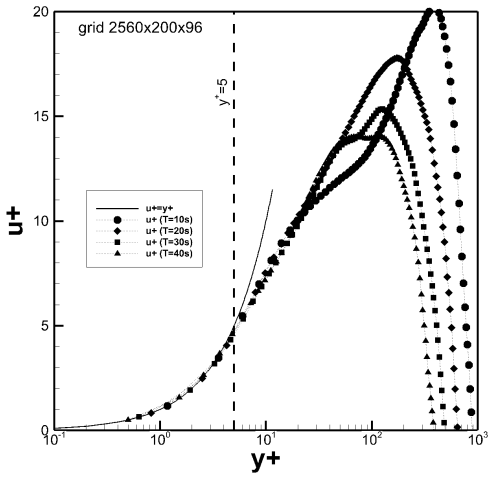

Figure 13: Streamwise velocity profile in wall normal direction in non-dimensional form at different times and linear profile from the law of the wall.

ical Simulation, see Figure 14, where an example of a profile averaged solely in the spanwise direction is shown, highlighting the excessive near-wall refinement. Consequently, this configuration was discarded. No further refinements were considered in the x-direction, as the nx3 case already exceeds the finest grid resolution used by [66]. Moreover an increase in the resolution in the x direction could introduce errors due to the resulting cell aspect ratio. The spatial resolutions nx2–ny1 and nx3–ny2 in x and y produce, except at the wall, cells with a length $\Delta x < \Delta y$, with a ratio Δx / $\Delta y \approx 0.5$, meaning that Δy is twice Δx. Increasing the number of cells in the x direction would lead to aspect ratios even farther away from unity. This may affect the representation of subgrid-scale stresses when using a Smagorinsky model, since the model employs a single length scale for all directions, potentially introducing errors in the accurate representation of the problem's physics [39]. In light of the above considerations, it was deemed appropriate to adopt a reference grid with resolutions nx3=2560, ny2=200 and nz3=92, as can be observed in Table 2.

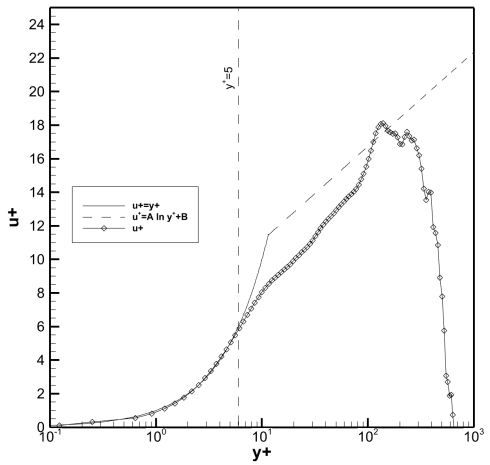

Figure 14: Number of cells within the viscous layer in case of ny=240.

Finally, a test was performed to assess the time independence of the simulations. Figure 15 shows the front evolution for the 2560×200×76 grid case, comparing three simulations performed with Courant numbers of 0.45, 0.6, and 0.9, respectively. It can be observed that the front evolution profiles are nearly superimposed. A Courant number below 0.5 has also been adopted in previous studies of gravity currents involving more complex physical phenomena than the present case (see [92, 93]).

With regard to the guidance on grid resolution for WF-LES, Figures 16, 17, and 18 present a comparison between the results of the fully resolved case and those obtained for the HR-NR case and the HR-WM-S model, varying the resolution in the x, y, and z directions, respectively. In Figure 16, it can be observed

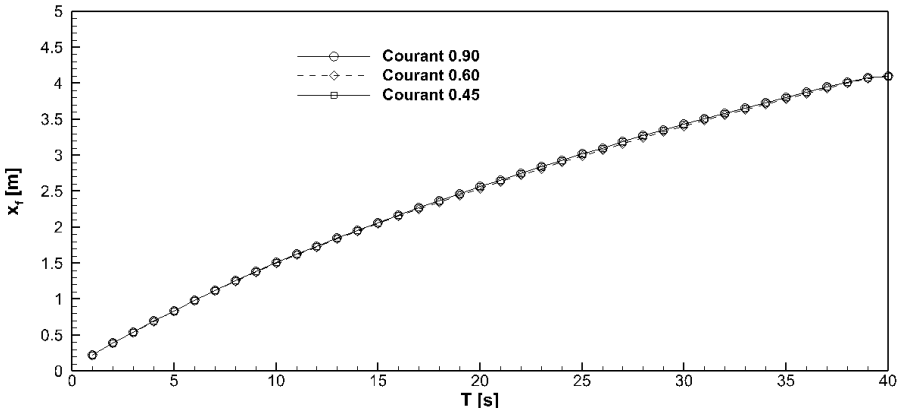

Figure 15: Front evolution in time considering three different Courant numbers, namely 0.45, 0.6 and 0.9 using the grid 2560x200x76.

that the results in terms of front evolution are similar between HR-WM-S and HR-NR; however, as the x-resolution decreases, the results tend to deteriorate, leading to a slowing of the front. The grid is likely too coarse in the horizontal plane to capture mixing during the slumping phase. The reduction in vertical resolution, however, has a different effect: in the coarsest case (ny=60), HR-NR tends to accelerate with respect to the reference case, whereas HR-WM-S tends to slow down. In both cases, the wall stress is therefore not correctly reproduced. For HR-NR, this is due to the lack of sufficient turbulent viscosity at the first cell, with the stress being compensated by an increase in the velocity gradient. For HR-WM-S, the slowdown can instead be attributed to an excessive turbulent viscosity at the first cell; this behavior is likely related to the adopted profile, which was designed for wall-bounded flows under steady-state conditions.

A similar behavior is observed when varying the z-component, namely, acceleration for the HR-NR case and deceleration for the HR-WM-S case. For HR-WM-S, the differences from the fully resolved case appear to be more limited. For HR-NR, acceleration of the front is observed only in the finest-resolution case. References to the grid resolution are reported in the flow topology analysis and in the entrainment analysis. Therefore, the optimal condition was found to be the configuration with a mesh resolution of $1024\times100\times48$, as reported in Table 3.

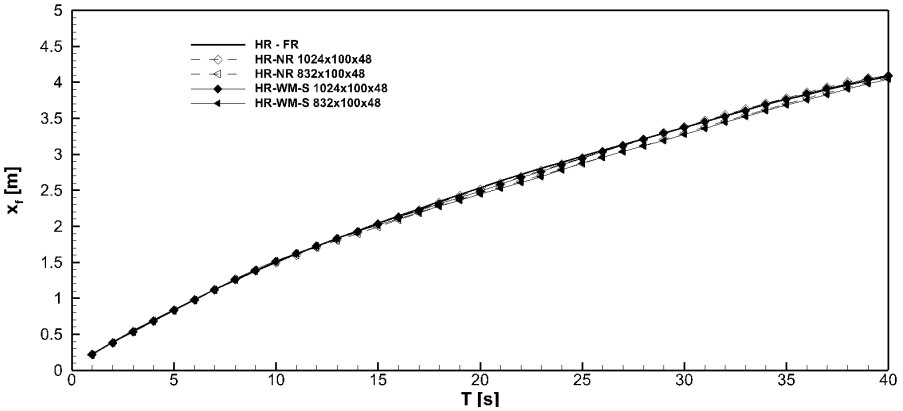

Figure 16: Front evolution in time for different grids resolution, x variation.

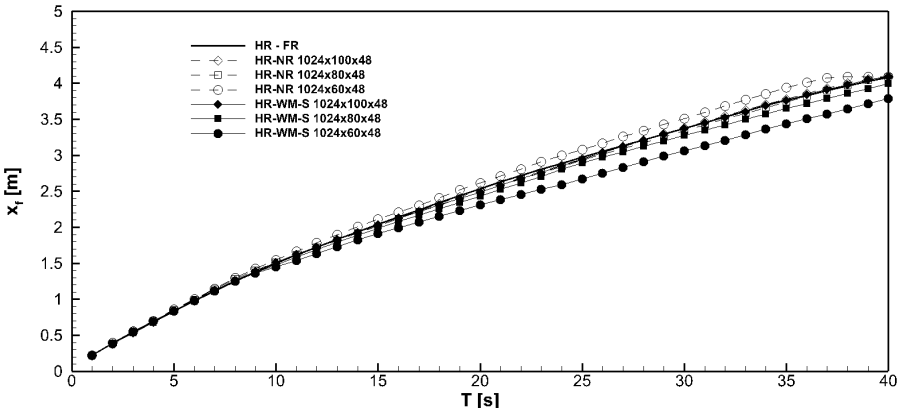

Figure 17: Front evolution in time for different grid resolutions, y variation.

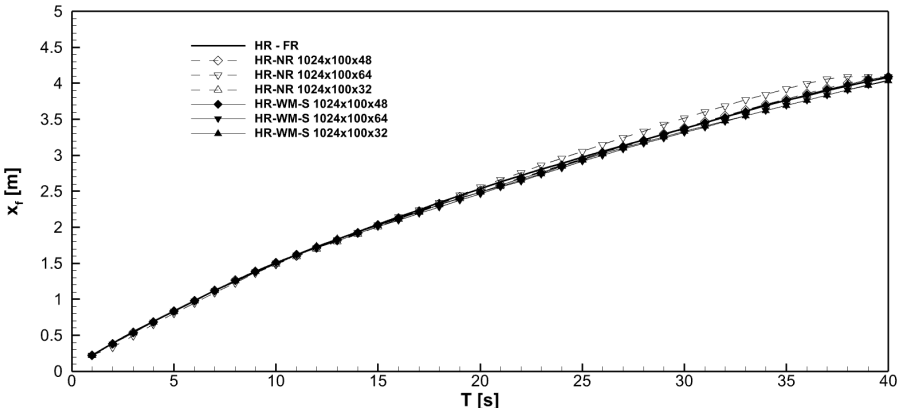

Figure 18: Front evolution in time for different grid resolutions, z variation.

4.4.2 Sediment-laden flows in lock exchange assessment

For the cases discussed in Section 4.2, the independence of the results from the computational grid was also assessed. To this end, three computational grids with different spatial resolutions were tested in order to evaluate mesh quality and its impact on the simulations. The main characteristics of the tested grids are summarized in Table 8.

Table 8: Grid resolution.

	x direction		**y direction**		**z direction**	
A	nx1	1500	ny1	160	nz1	64
B	nx2	1852	ny2	178	nz2	75
C	nx3	-	ny3	-	nz3	85

The three grids feature a y-directional grading applied to both the lower and upper 20% of the domain height, corresponding to a total of 40% of the overall vertical extent. In the central region, a constant cell size of $\Delta y = 0.0074H$ was maintained across all three grids. The main differences concern the height of the first cell near the wall: in Grid A, $\Delta y = 0.003H$, whereas in Grids B and C the reference value $\Delta y = 0.002H$ was adopted. In the streamwise (x) direction, the discretisation length is $\Delta x = 0.0074H$ for Grid A, and $\Delta x = 0.006H$ for Grids B and C. Along the spanwise (z) direction, three different resolutions were chosen, namely $0.0116H$, $0.0098H$, and $0.0087H$, resulting in a progressive grid refinement across the three cases.

As in the previous section, the front position evolution in time was evaluated.

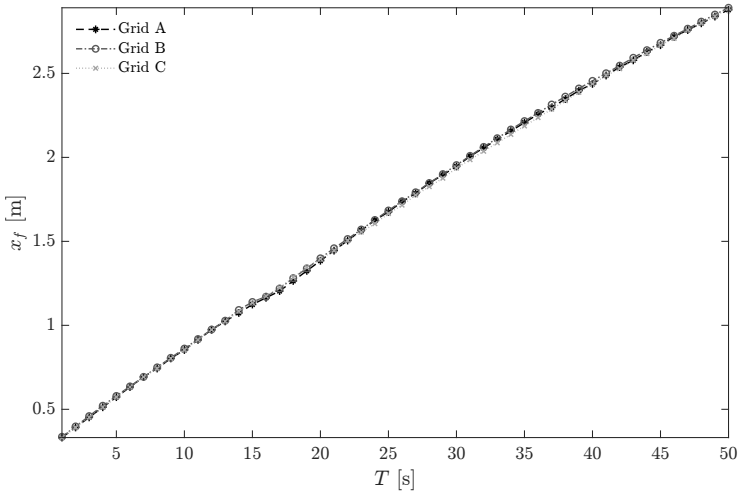

Figure 19: Front evolution in time for different grid resolutions.

As shown in Figure 19, all the analyzed grids yield acceptable results in terms of the front position x_f. The discrepancies among the three spatial discretizations remain within acceptable limits and do not significantly influence the overall evolution of the current. Moreover, the observed stability of the solutions and the consistency of the derived flow quantities indicate that the adopted spatial resolution is adequate to capture the dominant flow features. Specifically, the relative error in the front position is $\leq 1\%$, confirming that the grid is sufficiently refined to resolve the front propagation accurately.

However, an analysis of the wall shear stresses revealed moderate differences among the grids. Consequently, the finest mesh was selected for all subsequent simulations, as the present study also aims to accurately assess erosion and deposition processes, which are particularly sensitive to near-wall resolution.

5 Results for gravity current: boundary layer and wall modeling

The numerical experiments were conducted in a lock-exchange configuration, as will be illustrated in section 4, using an Eulerian formulation for salinity transport. In this approach, the fluid properties are computed at fixed points in space, allowing accurate resolution of concentration gradients and mass fluxes. This method ensures consistency with the laboratory and numerical experiments used as validation benchmarks [63, 65], while providing a robust framework for capturing the dynamics of density-driven flows.

5.1 Validation

This section addresses the validation phase, comparing the results obtained from the model presented in Section 4.1 (Ottolenghi-FR) with the reference results reported by [63, 65].

5.1.1 Flow topology

The evolution of the front position over time allows for the analysis of the gravity current across different regimes. The front, denoted as x_f, is defined as the frontmost position of the current nose located 0.02H above the bottom surface, as in [59] and [63]. To define the interface between the current and the ambient fluid, a characteristic isopycnal is defined by a threshold value of $\langle \rho^* \rangle = 0.02$, as in [63], where $(\langle\rangle)$ represents the averaging operator in the spanwise direction, while ρ^* is the dimensionless density field calculated as:

$$\rho^* = \frac{\rho(x, y, z, t) - \rho_0}{\rho_1 - \rho_0} \tag{38}$$

Figure 20 shows a comparison between the results of the Ottolenghi-FR simulation and those of Ottolenghi et al. (2016), both numerical (RUN2) and experimental (EXP2), for the dimensionless front position ($x_f^* = (x_f - x_0)/x_0$) over dimensionless time ($T^* = t \cdot u_b/x_0$), in logarithmic scale.

It can be seen that the results obtained with the model presented in Section 4.1 agree with the reference numerical results and are very similar to the experimental ones. Using the logarithmic scale, the different phases of the gravity current can be easily observed, as described in the introduction. During the slumping phase, the current front velocity remains approximately constant. The curve in this phase displays a linear trend with a unitary slope (dashed dot line with slope=1 in Figure 20). This phase also marks the onset of Kelvin-Helmholtz instabilities, as described by [6], which are evident in Figure 21a, where the dimensionless density contour is shown during the initial stage of the current, $T^* = 7.7$. As the current advances, it enters into the so-called self-similar phase; the front begins to decelerate because of the entrainment of ambient fluid into its head (see also Figure 21c at $T^* = 31.3$). This entrainment alters the slope of the curve, with a progressive transition from T^* to $T^{*2/3}$

(light gray dashed dot line slope=2/3 in Figure 20). The density field (see Figure 21c) reveals a thinning of the current, resulting from the continued decline in density concentration. For the analyzed case, due to the adopted aspect ratio and reduced gravity, the domain is too short to observe the viscous phase; in this phase, the front velocity slows down further and the curve slope tends to 1/5 [72].

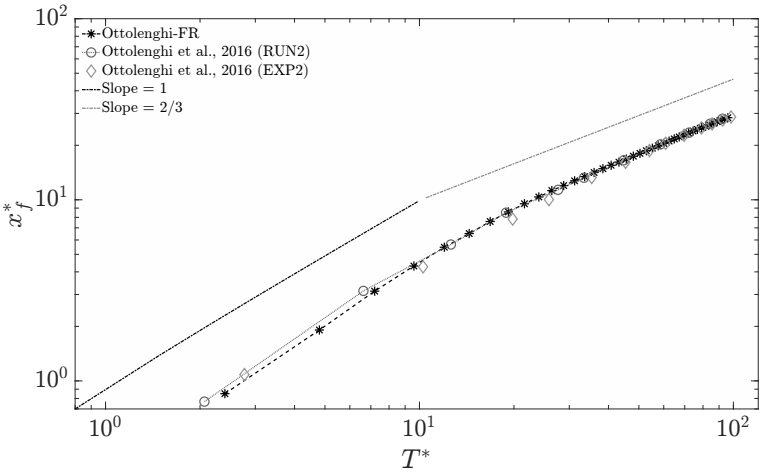

Figure 20: Dimensionless front position evolution in time, in logarithmic scale, comparison between the Ottolenghi-FR case and the [63] results.

5.1.2 Wall-shear stresses

Wall stress is an important parameter in evaluating gravity currents, as it provides an indication of the flow's ability to erode the bottom and potentially sustain the gravity current itself. It is defined as:

$$\tau_w = \mu \frac{d\langle u \rangle}{dy}|_{y=0} \tag{39}$$

where μ is the dynamic viscosity. The friction velocity is related to the wall stress through the following equation:

$$u_\tau = \sqrt{\frac{|\tau_w|}{\rho}} \tag{40}$$

Figure 22 shows a comparison with the reference data for the friction velocity along the streamwise direction, averaged along the spanwise direction, and non-dimensionalized using the buoyancy velocity u_b. The plots refer to two time instants, representative of the self-similar phase described above. Figure 22a corresponds to $T^* = 31.3$, while Fig. 22b corresponds to $T^* = 65.4$.

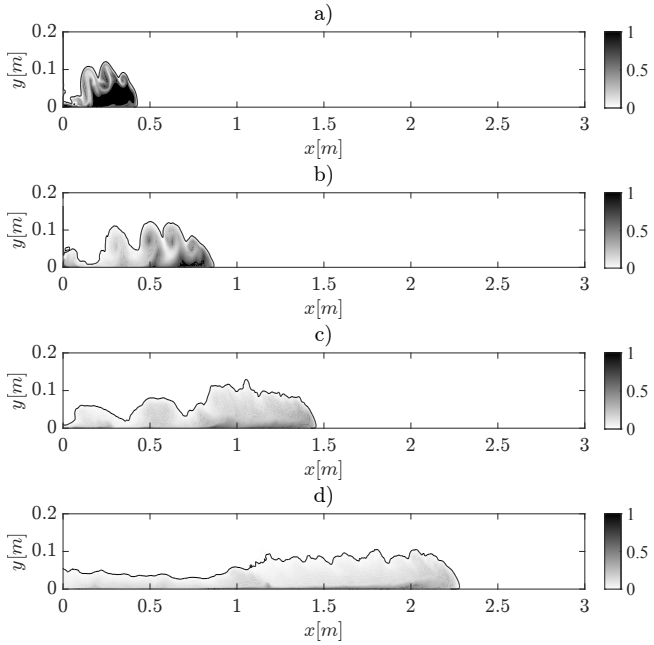

Figure 21: Contour of $\langle \rho^* \rangle$ at different runs for the Ottolenghi-FR case: a) time $T^* = 7.7$, b) time $T^* = 18.6$, c) time $T^* = 31.3$, d) time $T^* = 65.4$.

The results agree well with the reference data. In both plots, higher values are observed at the head of the gravity current, with peaks near the front, followed by a decrease towards the tail of the current. The higher values at the head are attributed to the structures forming in the mixing layer at the interface between the denser fluid and the ambient fluid, specifically the Kelvin-Helmholtz billows.

It can also be observed that during the transition from the slumping phase to the self-similar phase, the wall stress decreases, leading to a corresponding reduction in the current sediment transport capability.

Additionally, in Figure 23, the Hövmoller diagrams (which represent the evolution in time of the dimensionless friction velocity trend along the streamwise direction) of Ottolenghi-FR case confirms that in any instance of time, the highest values of friction velocity are observed at the head of the current.

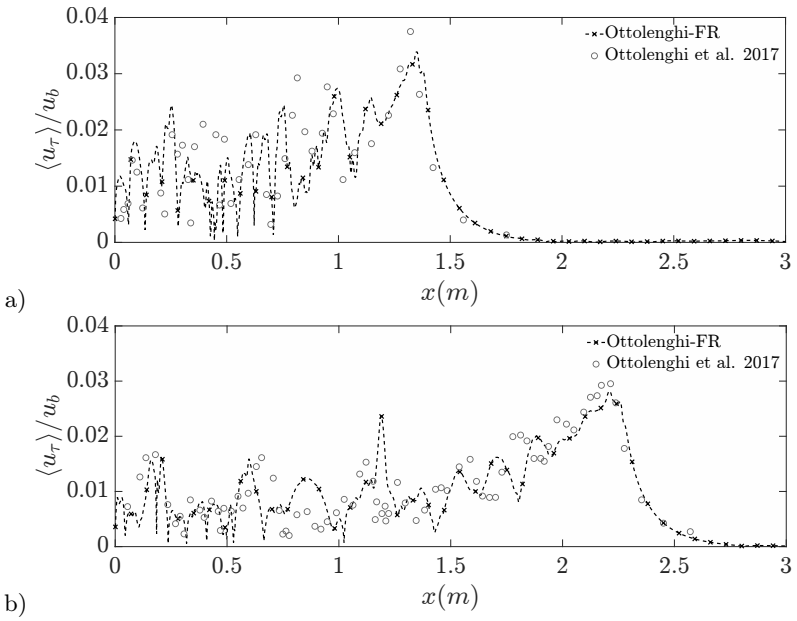

Figure 22: Streamwise evolution of dimensionless friction velocity at different times, a confrontation between Ottolenghi-FR (dashed lines and crosses) and the [65] case (dashed lines and circles): a) time $T^* = 31.3$, b) time $T^* = 65.4$.

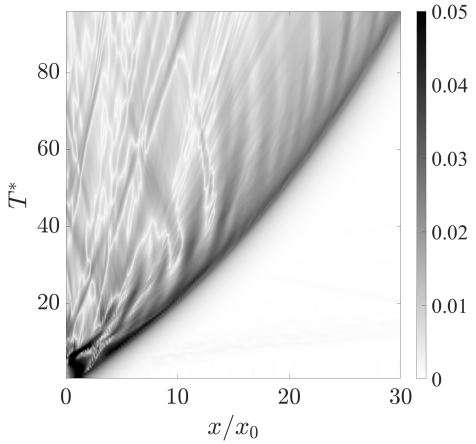

Figure 23: Hövmoller diagrams of the dimensionless friction velocity field for the Ottolenghi-FR case.

5.2 Boundary layer

The application of wall models relies on the assumption that a well-defined boundary layer exists and that, in the near-wall region, the flow exhibits a linear profile within the viscous sublayer, followed by a logarithmic profile [70]. In this section, the characteristics of the boundary layer are assessed for the fully resolved case; the analysis was conducted at the head of the current. Various approaches can be employed to define its spatial extent (see, for example, [60]). In the present study, a definition based on density was adopted. For each position i along the x-direction, the following quantity was computed:

$$\langle \rho_j^*(i) \rangle = \frac{\sum_{j=1}^{nh} \langle \rho^*(i,j) \rangle \Delta y(j)}{\sum_{j=1}^{nh} \Delta y(j)} \tag{41}$$

where j denotes the wall-normal direction, and $j = nh$ corresponds to the height of the gravity current, evaluated with respect to the reference value $\langle \rho^* \rangle = 0.02$. A mean value was then computed along the x-direction over the entire gravity current:

$$\langle \rho_{ij}^* \rangle = \frac{1}{nl} \sum_{i=1}^{nl} \langle \rho_j^*(i) \rangle \tag{42}$$

where $i = nl$ represents the position of the front. The head is a region characterized by high density values; the criterion adopted for its definition was therefore to identify the first occurrence for which $\langle \rho_j^*(i) \rangle < \langle \rho_{ij}^* \rangle$ holds. This criterion was applied starting from the head and moving in the direction opposite to the current. Figure 24 illustrates, at t=13 s, the height of the current, the variables described above, and the start and end points of the head as identified by this method.

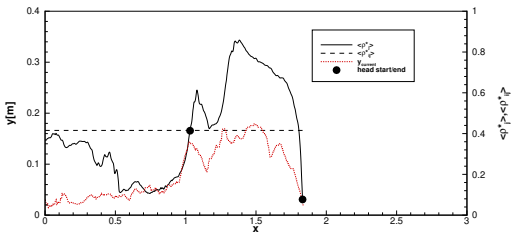

Figure 24: Example of gravity current head identification based on density.

Within the head region, the velocity profile along the wall-normal direction was computed by first averaging the data in the spanwise direction and subsequently performing an ensemble average over the profiles obtained along $i - direction$. Figure 25 shows an example of the resulting non-dimensional velocity profile. In addition, the corresponding velocity gradient profile du/dy is presented, together with a representative near-wall behavior consisting of a linear profile, valid in the viscous sublayer ($u^+ = y^+$), and a logarithmic profile of

the form $y^+ = A\ln(y^+) + B$ where $A = 1/\kappa = 1/0.41 = 2.439$ and $B = 5.5$. In a $u^+ - \log(y^+)$ plane, these two coefficients correspond, respectively, to the slope and the intercept. From the figure, it can be observed that the first computational point is located at $y_1^+ = 1$, and the first three points lie approximately within the viscous sublayer ($y^+ < 5$); the inner layer then extends to about 20 wall units. This is followed by a logarithmic trend up to approximately 70 wall units. Compared to the canonical logarithmic profile shown, the present case exhibits a steeper slope and a lower intercept.

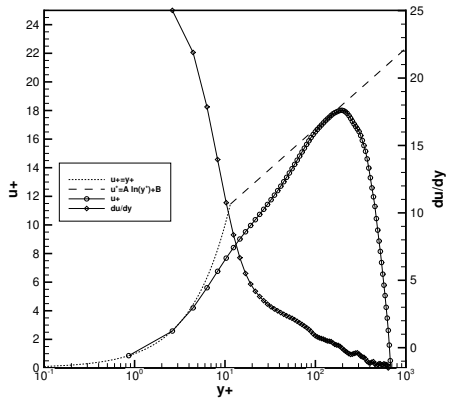

Figure 25: Mean streamwise velocity profile along wall normal direction in non-dimensional form and velocity gradient along wall normal direction.

The regions described above can be analyzed in terms of the velocity gradient dU/dy. In a canonical wall-bounded flow under neutrally stratified conditions, the inner layer is characterized by strong vertical velocity gradients, which then tend to attain a nearly constant value within the logarithmic region. At the outer edge of the boundary layer, the velocity gradients approach zero, indicating that the velocity approaches the undisturbed free-stream value. A similar behavior is observed in the present case, see Figure 25 for the profile of du/dy, although the profile is subsequently influenced by the mixing region and the counterflow velocity of the ambient fluid. The criterion adopted to define the thickness of the boundary layer was du/dy=0. In addition, the possible extent of the logarithmic profile was also estimated through the quantity $du/d(logy+)$.

Figure 26 presents the boundary layer height determined, the friction velocity and the logarithmic extent at one-second intervals, expressed in non-dimensional terms. The initial instants are not reported, as a strong variability of the profiles is observed along the x-direction and the head is not yet well defined. It is observed that during the initial slumping phase, a boundary layer develops and progressively increases in vertical extent, reaching a maximum at approximately six seconds. Subsequently, as mixing processes with the ambient fluid are initiated, the boundary layer thickness decreases toward an asymptotic value. The logarithmic region initially occupies a limited fraction of the bound-

ary layer; during the self-similar phase, it progressively extends over a larger portion, and in the final phase, it seems to stabilize at a constant value.

By analyzing the different cases and considering the evolution of the boundary-layer thickness shown in Figure 26 for the G3H2 configuration, one can assess how the governing variables influence its temporal development. In particular, Figure 27a shows that, as the domain height increases from 0.2 to 0.4 m, the boundary-layer thickness grows by approximately the same amount throughout most of the simulation. An exception occurs toward the end of the run, where the flow is likely influenced by its proximity to the right boundary of the domain. When g' is reduced from 0.59 to 0.075 while keeping the domain height fixed at $H = 0.2$ m, the maximum boundary-layer thickness decreases progressively, and its occurrence shifts to later times. This behavior indicates that a lower initial density contrast delays the attainment of a stabilized regime.

When the boundary-layer thickness is non-dimensionalized as $\delta^* = y_{bl}/(u_b^2/g')$ and time as T^* (see Section 5.1.1), thereby accounting for both effects, note that u_b depends directly on g' and H, as shown in Equation 2, the resulting trends become characteristic of gravity-current dynamics (Figure 27b). Specifically, all cases exhibit a peak in δ^* at the same T^*, although cases G1H2 and G3H2, with $H = 0.4$ m, display a slightly lower peak. Subsequently, all curves collapse onto a common plateau, indicating that once the current enters the self-similar regime, the boundary-layer thickness remains essentially constant.

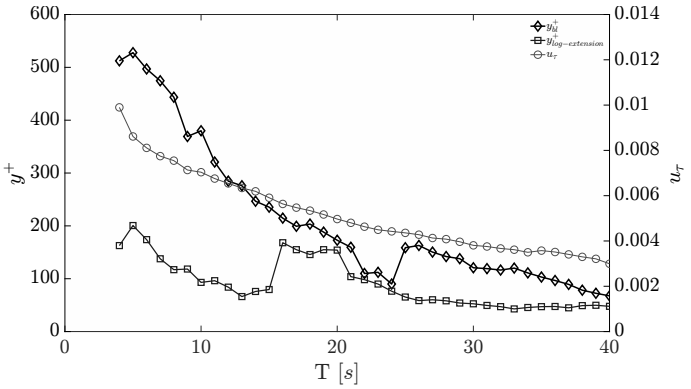

Figure 26: Evolution of the boundary layer and of the friction velocity over time at the head of the gravity current for the G3H2 case.

Once the head of the current was identified (see Figure 24) and the temporal evolution of the boundary-layer and log-layer heights was determined (see Figure 26), the time evolution of the velocity profiles at the head was analyzed and compared with the canonical logarithmic law, $u^+ = A \ln y^+ + B$, for all cases listed in Table 2. As shown in Figure 28a, the velocity profiles expressed in inner scaling (u^+ versus y^+) show a great variability and a strong deviation in comparison with the canonical logarithmic profile. By examining the profiles throughout the self-similar phase (Figure 28b), a clear convergence trend

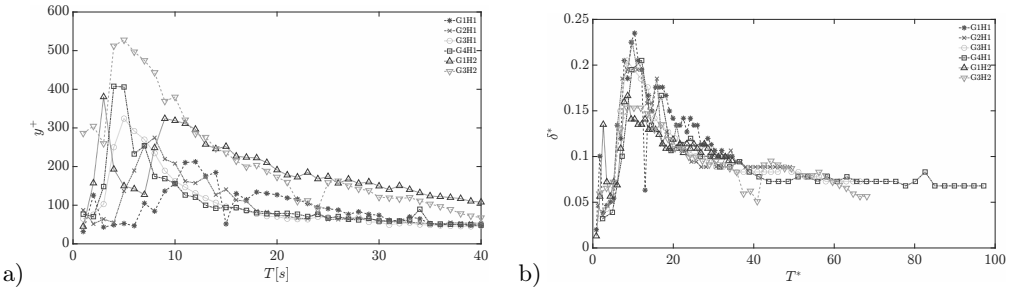

Figure 27: Dimensional a) and Dimensionless b) temporal evolution of the boundary layer.

is observed, and the presence of a logarithmic profile can be inferred, although with characteristics that differ from the canonical one. In particular, the viscous sublayer behavior ($u^+ = y^+$) is preserved at very small y^+, while the overlap/log region shows a marked tendency to align with the logarithmic law, with reduced scatter across different times and cases. This collapse in inner scaling indicates that the near-wall dynamics are consistently captured across the tested configurations. Consequently, representing the near-wall region using wall-functions, rather than fully resolving the viscous sublayer, is justified as a pragmatic compromise: wall-functions reproduce the essential inner-layer behavior while allowing coarser near-wall meshes and substantially lower computational cost.

A more complete view of this convergence trend is provided in Figure 29, where the cases are presented separately.

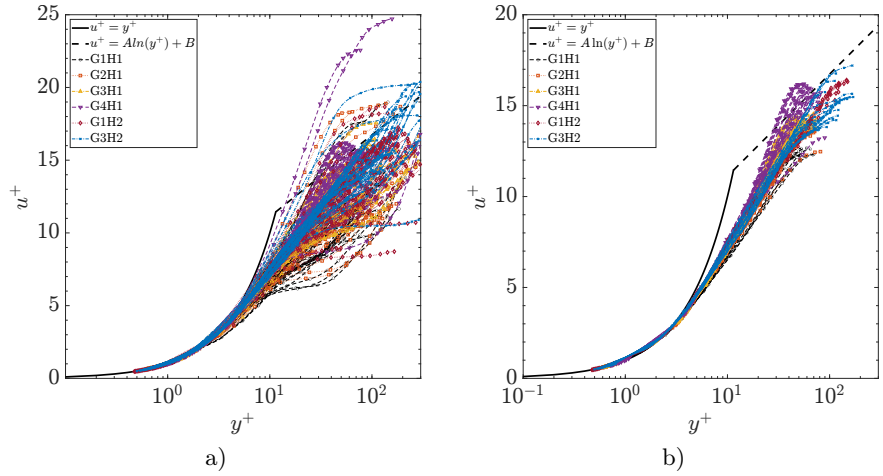

Figure 28: Temporal evolution of the dimensionless velocity profiles u^+ measured at the head of the current. a) shows the profiles collected for all the 40s of simulation, b) only in the self-similar phase

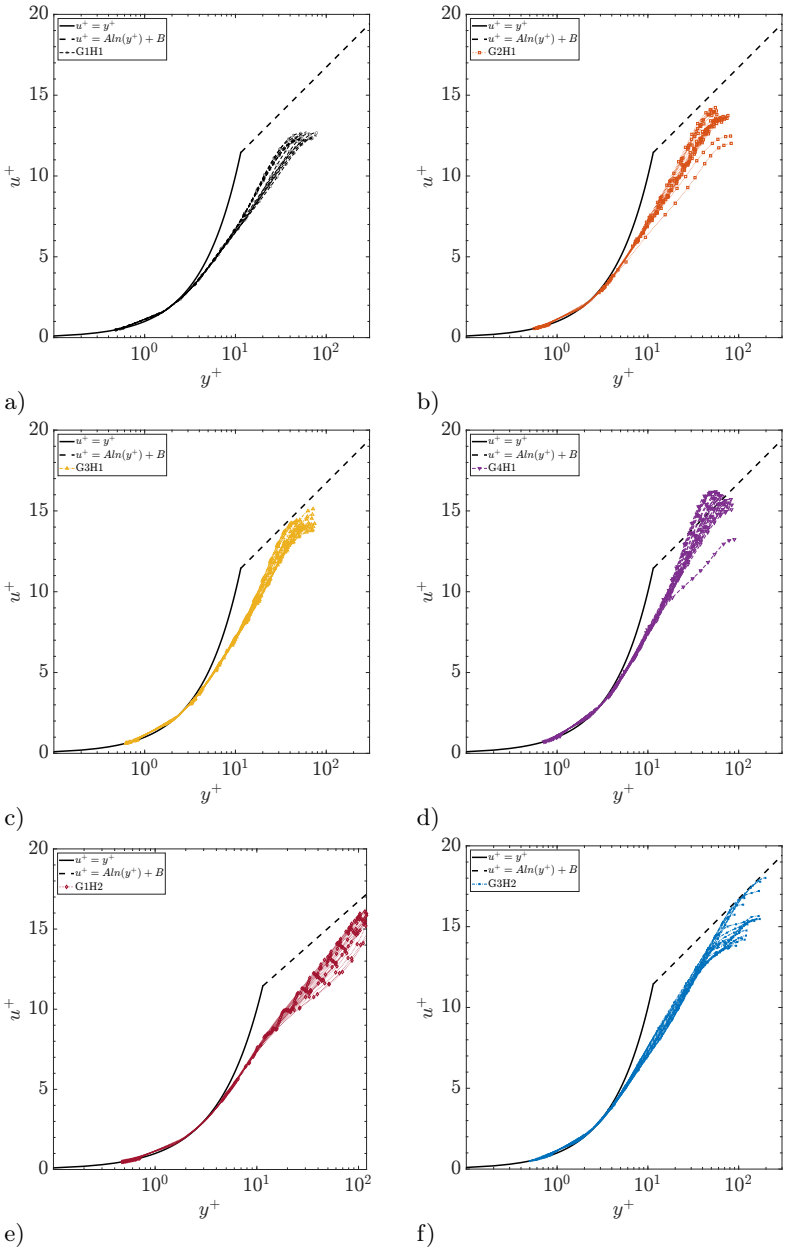

Figure 29: Temporal evolution of the dimensionless velocity profiles u^+ measured at the head of the current, in the self-similar phase, for the singular cases observable in Table 2.

Table 9: Log-law fitting parameters for the analyzed velocity profiles.

Case	g' [m/s^2]	H [m]	κ	A	B
G1H1	0.075	0.2	0.2712	3.6878	-1.6745
G2H1	0.150	0.2	0.2429	4.1168	-2.2348
G3H1	0.290	0.2	0.2056	4.8649	-4.0799
G4H1	0.590	0.2	0.1827	5.4744	-5.4679
G1H2	0.075	0.4	0.2866	3.4896	-0.4596
G3H2	0.290	0.4	0.2803	3.5577	-0.8892

Further insight into the evolution of the velocity profiles can be drawn from the study [4], which investigates near-wall behavior in a plane channel flow under stable stratification. Although this configuration differs from those considered in the present study, several of the reported findings are relevant for interpreting the behavior observed during the self-similar phase of the gravity currents analyzed here, as illustrated in Figure 29. In particular, the Figure shows that the velocity profiles differ substantially from those of the canonical logarithmic law, as anticipated. For each case presented in Figure 29, a logarithmic profile was fitted by minimizing the error relative to a mean velocity profile representative of the self-similar phase. The results were presented in terms of von Kármán constant κ, together with the slope coefficient A and the intercept B, are reported in Table 9. The results indicate that increasing stable stratification, associated with larger values of the reduced gravity g' and, consequently, larger density differences $\Delta\rho$, leads to a systematic decrease in the von Kármán constant κ. Accordingly, the slope coefficient A, which is inversely related to κ, increases, while the intercept B, representing the offset between the linear and logarithmic portions of the velocity profile, shifts toward lower values. This behavior admits a clear physical interpretation. As g' increases, buoyancy effects progressively suppress turbulence production and vertical momentum transfer. This suppression promotes a preferential redistribution of kinetic energy toward the streamwise direction, increasing the streamwise velocity component u. Consequently, the logarithmic velocity profile becomes steeper, reflected by an increase in A, and undergoes a downward shift, manifested by a decrease in B. As a result, the extent of the logarithmic layer is reduced, and its parameters lose universality, becoming dependent on the degree of stratification and, therefore, on g'.

5.3 High Reynolds cases and wall models

This section presents the results obtained using wall models for the case at $Re = 136,000$ and compares them with a fully resolved simulation.

5.3.1 Flow topology

The increase in available potential energy, from that corresponding to $H = 0.2$m to that corresponding to $H = 0.4$m, results in an acceleration of the flow, as it is possible to observe in Figure 30. In the validation case, the front position was determined based on a prescribed height, for consistency with the reference study. In the present case, in order to avoid potential ambiguities associated with the choice of a prescribed height, the position of the nose was computed by averaging, along the wall-normal direction, the values of $\langle \rho^* \rangle$.

Figure 31 compares the front position evolution over time between the WR-LES case (HR-FR) and the cases run on a coarser grid. Overall, in the initial stage, the simulations provide similar results. Subsequently, in comparison with the resolved case, it is observed that the HR-WM-B case tends to exhibit a slower evolution of the front. For the other cases, a similar behavior is observed: a slight deceleration in the central phase, followed, in the HR-NR and HR-WM-J cases, by a slight acceleration towards the end of the simulation. The different phases of the motion are described in detail below.

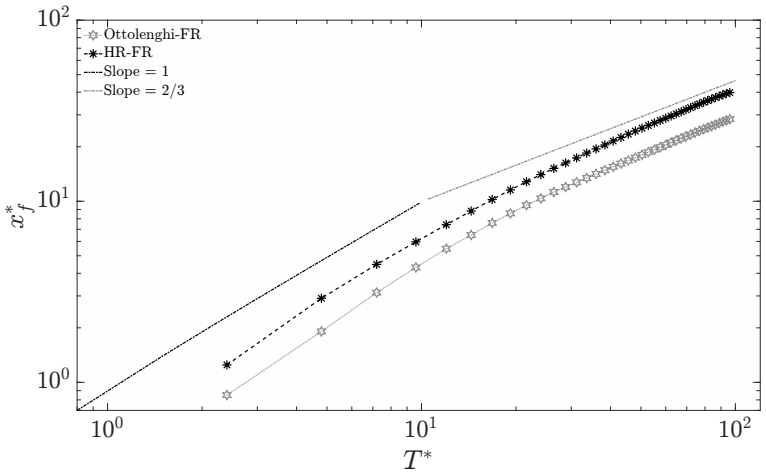

Figure 30: Dimensionless front position evolution in time, comparison between HR-FR (asterisk markers) and Ottolenghi-FR (hexagram markers) cases.

During the slumping phase, both the wall-function and not resolved cases exhibit behavior comparable to the fully resolved case (HR-FR), characterized initially by a nearly constant front velocity, followed by a gradual decrease between 7 and 10s. In the self-similar phase, the HR-FR case continues to decelerate, primarily due to the dilution of the saline water into the surrounding

freshwater. This deceleration is also observed in all the other cases, although in the HR-WM-B case it is excessively pronounced.

In the final portion of the self-similar phase, the deceleration observed in the resolved case persists and is accurately captured by the HR-WM-S case. Conversely, the other case based on increased eddy viscosity, HR-WM-B, maintains the excessive slowing previously noted. The unresolved case and the one based on the modification of eddy diffusivity, on the other hand, exhibit a slight acceleration of the front compared to the resolved case. In these two cases, the use of a coarse grid leads to an increase in velocity gradients near the wall, compensating for the lower eddy viscosity values in the wall-stress computation.

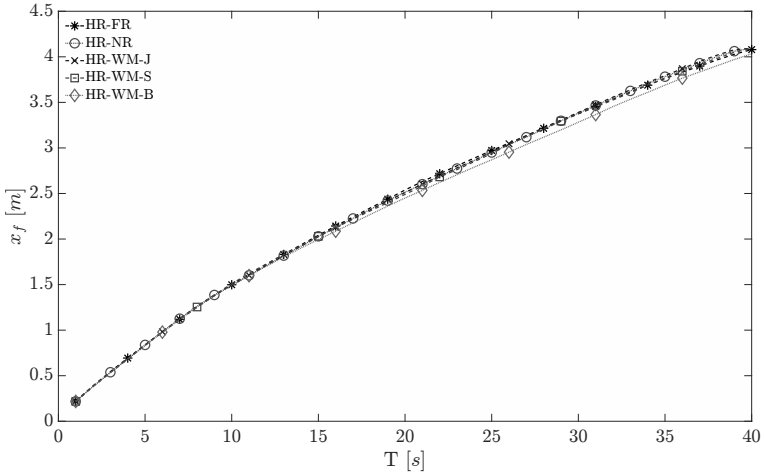

Figure 31: Front Position evolution in time, comparison between HR-FR case and the HR case with a coarser mesh.

in Table 10, a quantitative analysis of the coarse grid cases performance relative to the fully resolved case (HR-FR) is presented through the computation of percentage errors. These errors were first evaluated over the entire simulation time and then subdivided into three distinct temporal intervals to assess the model behavior across different flow regimes. This error was computed as follow ([63]):

$$Err = mean\left(\left|\frac{x_{f(HR-FR)} - x_{f(WM)}}{x_{f(HR-FR)}}\right|\right) \tag{43}$$

From Table 10, It can be observed that, among the various cases, although the difference with respect to HR-FR is minor (never exceeding 2.70%), all cases perform similarly during the slumping phase ($T^* = 3.4$–34). In contrast, in the self-similar phase, the HR-WM-B configuration begins to deviate from the reference case and achieves its peak error between $T^* = 34$ and 102, subsequently decreasing in the final 10 seconds. The HR-NR configuration, after the initial seconds, maintains an almost constant error trend, oscillating between

0.67% and 0.52% over the last 30 seconds of the simulation. The HR-WM-J case, namely, the other case without eddy viscosity intensification, exhibits behavior similar to that of HR-NR, except in the final phase, where the error tends to increase slightly. The HR-WM-S case, after a divergence peak from HR-FR between $T^* = 34$ and 102, exhibits only a minimal deviation in the closing seconds (approximately 0.25%). Overall, albeit by a narrow margin, the HR-WM-S configuration achieves the lowest total error among all the cases considered. Moreover, as time progresses, the error exhibits a decreasing trend.

Table 10: Cases with percentage error, in comparison with HR-FR.

Case	$Err_{tot}\%$	$Err\%$ $(T^* = 3.4 - 34)$	$Err\%$ $(T^* = 34 - 102)$	$Err\%$ $(T^* = 102 - 136)$
HR-NR	0.71	0.95	0.67	0.52
HR-WM-J	1.83	0.91	0.64	0.84
HR-WM-S	0.68	1.00	0.80	0.25
HR-WM-B	1.88	1.00	2.70	1.94

The observed behavior can be interpreted in light of the underlying dynamics of gravity currents. The phenomenon exhibits intrinsic temporal and spatial unsteadiness, which is likewise reflected in the evolution of the wall-bounded flow.

In the initial instants, the flow can be qualitatively approximated as inviscid. A viscous layer develops at the wall; however, the influence of friction has not yet propagated in the wall-normal direction, and the velocity gradients along the vertical are negligible. In this situation, it is to be expected that the use of coarse grids, both with and without wall models, can accurately reproduce the behavior of the flow. As the current evolves, the viscous effects in the vicinity of the wall become increasingly pronounced, leading to the formation of a boundary layer. In this case, an accurate representation of the near-wall flow dynamics becomes crucial. In the HR-WM-B case, for example, the excessive wall eddy viscosity results in a deviation from the resolved case. For the other cases, only in the final phase, regarding the evolution of the front, there is a slight improvement observed when employing a wall model.

The analysis also considered other coarse grid configurations (here not shown). It was observed that a reduction in the number of cells along the x-direction (from 1024 to 832) leads, for the various cases analyzed, to an overall slowing of the front compared to the resolved case. A reduction in resolution along the y-direction (to 60 and 80 cells) determines a different trend between the cases without eddy viscosity intensification, HR-NR and HR-WM-J, and the cases HR-WM-S and HR-WM-B. The former tend to accelerate with respect to the resolved case, whereas the latter tend to decelerate. For the latter cases, the model evidently yields an excessive eddy viscosity at the first off-wall cell. In contrast, for the HR-NR and HR-WM-J cases, the absence of eddy viscosity intensification results in an increased velocity gradient in order to maintain force balance. Finally, an opposite trend is also observed when modifying the resolution in the z-direction (32 and 64 cells), albeit to a lesser extent.

Figure 32 shows, on an xy plane and at four time instants, a contour of

the dimensionless density averaged in the spanwise direction for cases HR-FR, HR-NR and HR-WM-S. As noted in the front-position analysis, the HR-WM-S and HR-WM-NR configurations show slightly better performance than the other cases in terms of front evolution.

Analyzing the shape of the current, it is observed that, in general, the head size is qualitatively captured reasonably well, while the tail appears thicker in the coarse grid cases compared to the reference case. At time $T^* = 23.8$, as shown in Fig. 32a, during the slumping phase, Kelvin–Helmholtz instabilities are visible. Despite the reduced grid resolution, the HR-NR seems to preserve the head shape of the reference case better than HR-WM-S, maintaining it more compact and dense.

At $T^* = 47.6$, as the current progresses, the tail becomes more extended. Here, the HR-WM-S case shows slightly better results compared with the reference case than HR-NR. Indeed, in the HR-NR case, the structures appear sharper and exhibit reduced mixing, particularly near the bottom and close to the front of the current, where the salinity concentration remains higher compared to HR-FR.

At $T^* = 91.8$, The HR-WM-S case exhibits improved performance in terms of current-head extension and mixing. Unlike HR-NR, it maintains the elongated head shape characteristic of the reference case. This behavior is likely due to the increased viscous contribution to the flow during this simulation phase, which is effectively represented by the Spalding model.

At $T^* = 119$, as viscous effects become more relevant, the current shape in the HR-WM-S case closely matches that of the HR-FR case, whereas HR-NR continues to exhibit a more compact head with reduced mixing with the ambient fluid.

In general, as the current evolves into the self-similar phase ($T^* = 47.6$, 91.8, 119), the differences between the resolved case and the HR-WM-S cases diminish, while the HR-NR case appears to maintain the behavior observed in the slumping phase over time.

5.3.2 Wall-shear stresses

Similarly to what was analyzed during the validation phase, the evolution of wall stress in space and time is evaluated, through the friction velocity, see Eq. 40. This parameter is important because it defines the model's ability to accurately represent potential bed erosion.

Figures 33a, b, c and d show the trend of the mean friction velocity made non-dimensional with u_b, along the streamwise direction at the dimensionless time instants T^* of 23.8, 47.6, 91.8 and 119 respectively, corresponding to the slumping and the self-similar phase.

Unlike Figure 22, a higher deviation is observed between the coarse grid cases compared to the reference case. On the other hand, this behavior is expected, considering the different numerical schemes adopted near the wall and the grid resolution. Qualitatively, it can be observed that the cases exhibit

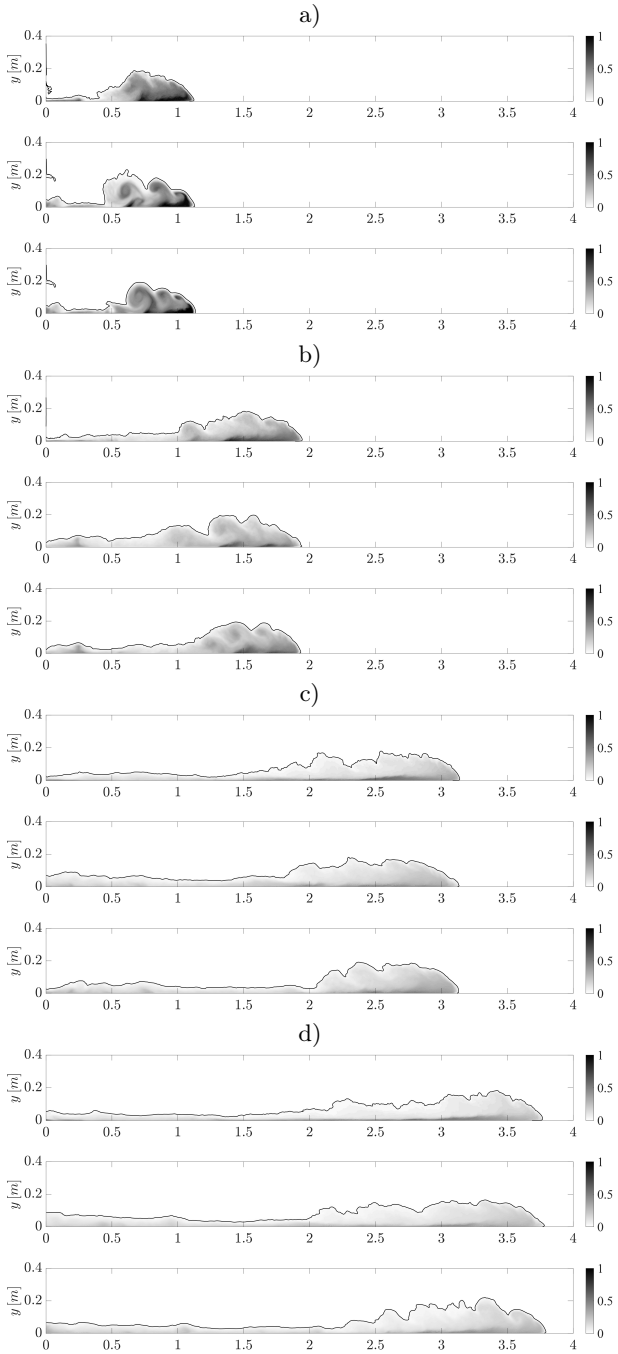

Figure 32: $\langle \rho^* \rangle$ fields, a confrontation between HR-FR (top), HR-WM-S (center) and HR-NR (down) at different time steps: a) time $T^* = 23.8$, b) time $T^* = 47.6$, c) time $T^* = 91.8$ and d) time $T^* = 119$.

similar average values, in terms of magnitude, at the head and tail of the gravity current.

During the slumping phase, the coarse-grid cases exhibit peaks that are in phase with the wall-resolved case, although lower peak values are observed, particularly for the cases involving eddy viscosity intensification (HR-WM-S and HR-WM-B).

This behavior can be explained by what was previously observed. The slumping phase is strongly characterized by the formation of Kelvin-Helmholtz structures, which are then reflected in the wall stress. In the coarse grid case, these structures are not properly modeled (see the Figure 32a with the density contour and the section on entrainment), and this is reflected in the peaks observed in Figure 33a. This is particularly true for the HR-WM-S and HR-WM-B cases, where the assumption of a wall-law (valid under steady conditions) also plays a role, whereas the slumping phase is strongly unsteady.

As time progresses and the flow enters the self-similar phase, the friction velocity values decrease. The values obtained with coarse grids are more consistent with the resolved case, at least in the head region of the gravity current, while they tend to deviate with higher values in the tail, as shown in Figures 33b, and c. This is consistent with the thicker tail observed in the contours of Figure 32b,c, and d. In particular, a larger deviation is observed for the cases without eddy viscosity intensification (HR-NR and HR-WM-J), whereas a clear slowing of the current is evident in the HR-WM-B case. The observations are confirmed in the final phase (Figure 33d); in particular, it is noted that the HR-WM-S case, excluding the tail, tends to be more consistent with the resolved case. It should be recalled that in this phase, this case exhibits the smallest error compared to HR-FR with regard to the evolution of the front.

The general trend of friction velocity over time and space can also be observed in Figure 34, which presents the Hövmoller diagram for the HR-FR and HR-WM-S cases. The behavior is similar, with the highest values consistently appearing at the head or, during the slumping phase, in correspondence with the Kelvin-Helmholtz structures.

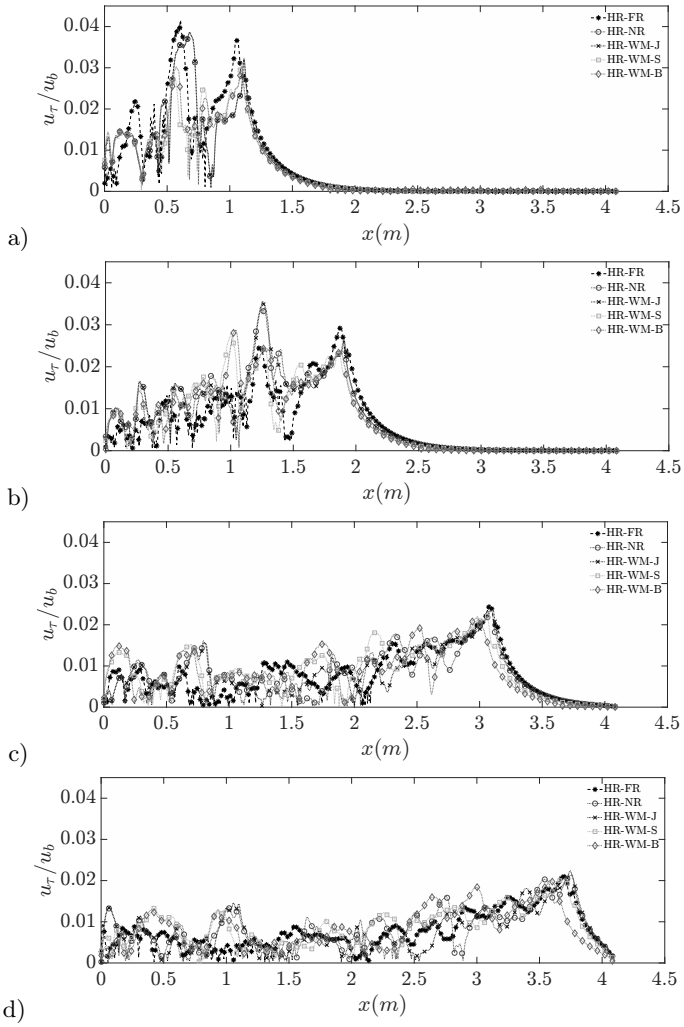

Figure 33: Dimensionless friction velocity at different times, a confrontation between HR-FR and the HR-WM cases: a) time $T^* = 23.8$, b) time $T^* = 47.6$, c) time $T^* = 91.8$, and d) time $T^* = 119$.

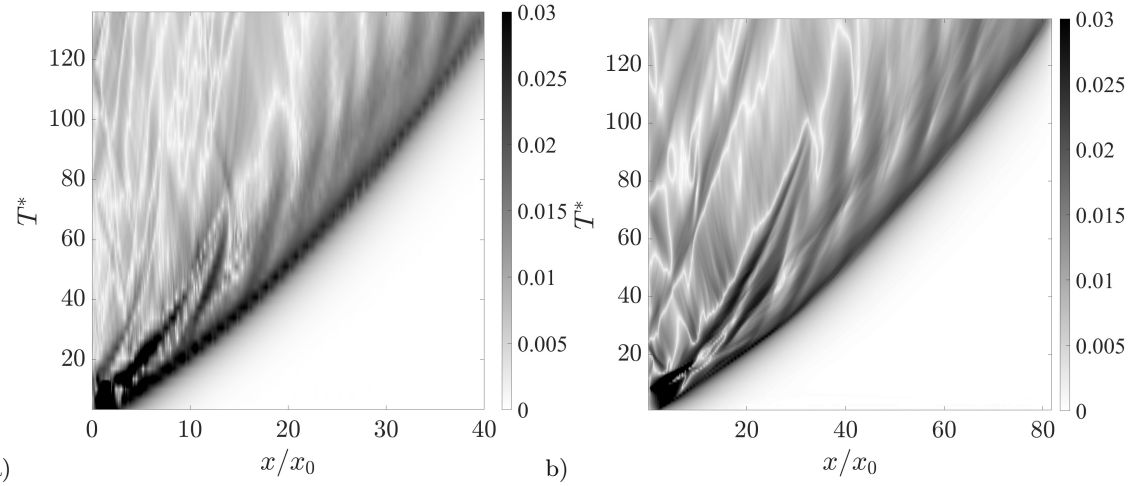

Figure 34: Hövmoller diagrams of the dimensionless friction velocity field $\langle u_\tau \rangle / u_b$ for HR-FR a) and HR-WM-S b) cases.

5.3.3 Entrainment

The use of a coarse near-wall grid inevitably affects the spatial discretization within the computational domain, particularly in the interface region between the denser fluid and the ambient environment, where most of the mixing occurs. Consequently, it is essential to evaluate the model's capability to accurately capture both the entrainment process and the characteristic density of the gravity current in space and time.

Figure 35a shows the time evolution of the averaged density over the complete gravity current at every instance of time (with the isopycnal threshold value $\langle \rho^* \rangle = 0.02$).

During the slumping phase, the coarse-grid cases tend to diverge from the reference case due to reduced mixing, resulting from the lower accuracy in representing Kelvin–Helmholtz structures (see Figure 32a) and the current tail. In the transition from the slumping phase to the self-similar phase, the results for the HR-NR and HR-WM-J cases are consistent with those of the resolved case. In contrast, for the cases with increased near-bottom eddy viscosity (HR-WM-S and HR-WM-B), a greater deviation is observed, with an integral density value significantly lower than in the other cases; only in the final phase the profiles tend to realign with the other solutions. This discrepancy can be attributed to the fact that the wall models are applied to the entire current, including the tail region, where they are likely not suitable.

As evidence of this, see Figure 35b, where the integral density is shown only in the head region, as identified in 5.2. It should be noted that, for the figure, as well as for the subsequent figures referring to the head of the current, the initial seconds are not shown, as the head is not yet fully defined. The results show

that, during the slumping phase and the transition to the self-similar phase, all coarse grid cases produce excessive mixing (and consequently a lower current density). Subsequently, it is observed that, in the self-similar phase, the cases employing viscosity-based wall models more accurately reproduce the reference case. As mentioned in the flow topology analysis (see section 5.3.1), additional cases were run with even coarser grids in the x-direction, which exhibit an overall slowing of the current. In these cases, the reduction in current density during the slumping and transition phases is even more pronounced. This suggests that the coarse meshes are unable to adequately capture the mixing processes between saline and freshwater during the slumping phase, not because of the model itself, but due to insufficient spatial resolution. This leads probably to an excessive decrease in horizontal pressure gradients, and consequently, to a reduction in the front velocity, which is not subsequently recovered.

The observations described above can also be related to the dimensions of the gravity current. Figure 36a and b show the area of the current enclosed by the reference value $\langle \rho^* \rangle = 0.02$, for the entire current and for the head only, respectively. Figure 36a clearly shows that the HR-WM-S and HR-WM-B cases deviate markedly from the reference case during the transition from the slumping to the self-similar phase, exhibiting a larger area and, consequently, a lower density; subsequently, they maintain a slope similar to that observed for the resolved case. By contrast, the HR-NR and HR-WM-J cases tend to deviate from the resolved case only in the final part of the self-similar phase. Considering only the head region (Figure 36b), it can be noted that the HR-WM-S and HR-WM-B cases generally display behavior closer to that of the resolved case.

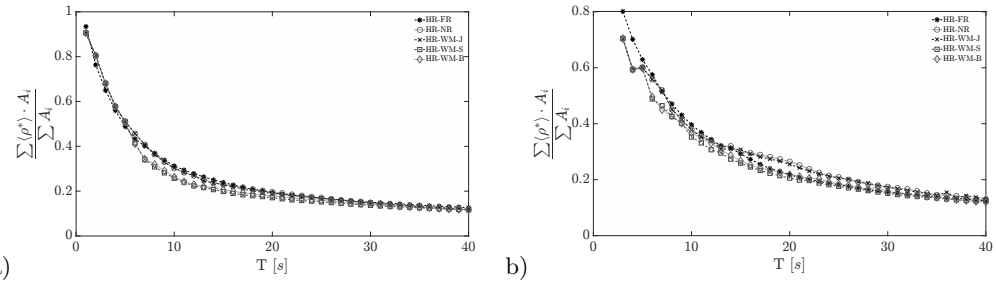

a) b)

Figure 35: Evolution in time of the dimensionless surface mass of the total current a) and of the head b).

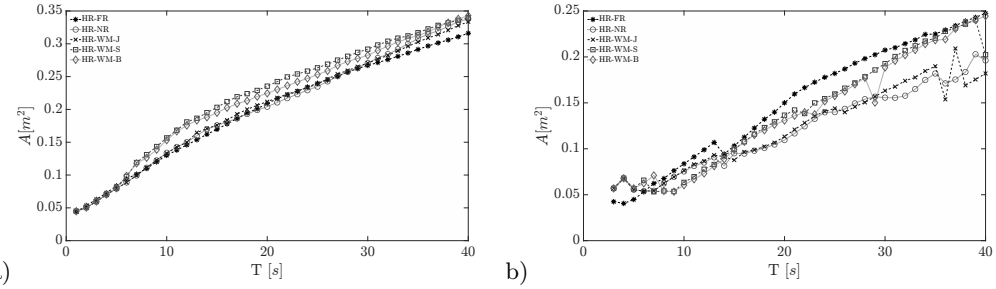

a) b)

Figure 36: Evolution in time of the total current Area a) and of the head Area b).

The behavior described in terms of current density and area can also be effectively quantified in terms of entrainment as performed in the reference study [64]. At time $t_0 = 0$, V_0 was defined as the initial volume of the gravity current. At a successive time, $t_i = t_0 + \Delta t$, the volume of the current will increase by a quantity ΔV_i with respect to V_0, due to entrainment. This increment can be defined as:

$$\Delta V_i = (A_i - A_0)d \tag{44}$$

Where d denotes the spanwise length of the channel, while A_i is the area below the isopycnal $\langle\rho^*\rangle = 0.02$ in a x-y plane. A_0 is the area of the gravity current at t_0, i.e. $A_0 = Hx_0$. Starting from ΔV_i, it is possible to calculate the bulk entrainment discharge as:

$$Q_{ei} = \frac{\Delta V_i}{\Delta t_i} \tag{45}$$

and the bulk entrainment velocity for every time step as:

$$W_{ei} = \frac{Q_{ei}}{S_i} \tag{46}$$

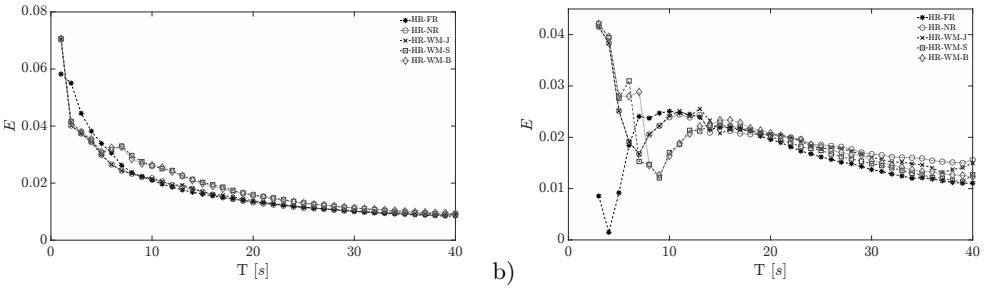

Figure 37: Evolution in time of the total current Entrainment a) and of the head b).

where S_i is the interface between the two fluids, and can be estimated as $S_i = d \cdot x_f$. Lastly, a dimensionless number for the entrainment can be defined as:

$$E_i = \frac{W_{ei}}{2U_{i-bulk}} \tag{47}$$

where the bulk entrainment velocity is made non-dimensional with the velocity scale $U_{i-bulk} = V_1 - V_2$ ([64]), with V_1 the bulk velocity of the gravity current, calculated as $(x_f - x_0)/(t_f - t_0)$, (where t_f denotes the time in which the gravity current has reached the position x_f) and V_2 is the bulk velocity of the ambient fluid.

Fig. 37a shows the entrainment as a function of the front position of the gravity current. Entrainment is highest during the initial phase, particularly in the slumping phase, where Kelvin–Helmholtz structures promote intense mixing between the current and the ambient fluid. As the flow evolves toward the self-similar phase, entrainment gradually decreases, following an approximately exponential trend.

The trends previously identified for density and current area are confirmed. During the transition from the slumping to the self-similar phase, the HR-WM-S and HR-WM-B cases are characterized by substantial entrainment. Subsequently, in the remaining part of the self-similar phase, entrainment decreases and tends to align with that of the HR-FR case, although it remains consistently higher. The HR-NR and HR-WM-J cases remain in agreement with the reference case throughout the self-similar phase. The overall behavior of the coarse-grid cases changes, however, when considering only the head of the current (see Figure 37b). In this region, during the self-similar phase, the cases with increased eddy viscosity tend to exhibit behavior more consistent with that of the HR-FR case. As the current evolves, the HR-NR case is observed to diverge increasingly from the reference case.

5.3.4 Near-wall region

The analysis of the near-wall region provides valuable insights into the streamwise velocity fluctuations ($u' = u - \langle u \rangle$) within this zone. Figure 38 presents these fluctuations at the first computational cell above the bottom wall, comparing the results of HR-FR (top), HR-WM-S (center), and HR-NR (bottom) at four distinct time instances.

In the HR-FR case, near the head of the current, elongated turbulent structures are clearly identifiable (Figure 38). These streaks are typical of wall-bounded flows ([70]) and are commonly observed during the evolution of gravity currents as well (see [62, 65]).

These coherent structures suggest that bed erosion is primarily driven along their longitudinal axes, with their fluctuations indicating regions of elevated shear stress. These types of structures are characteristic of the flow regime under investigation and are examined in detail in [58], where numerical simulations were performed using a configuration comparable to that adopted in the present study. The authors report that after the initial slumping phase (occurring at approximately $T^* = 8$ in their simulation), the current develops pronounced three-dimensional instabilities, particularly at its head. These "lobe-and-cleft" instabilities display strong morphological and dynamical similarities to the elongated structures identified in this thesis. By amplifying streamwise velocity fluctuations, these structures lead to increased shear stress, resulting in the formation of flow features described by the authors as "streaky patterns". As the flow progresses downstream, these structures progressively dissipate, eventually vanishing within the tail of the current. This spatial decay pattern, corroborated by the distribution of friction velocity (Figure 33), implies that the maximum erosive potential is concentrated at the leading edge of the current.

The presence of these specific structures provides insight into the current's ability to entrain bed particles along their paths, offering a better understanding of the sediment redistribution caused by this type of flow. Furthermore, the observed shortening of these structures over time indicates a reduction in the erosive potential of the current, as it evolves from the slumping phase (Figure 38a) to the self-similar phase (Figure 38b,c,d). Regarding the comparison with the coarse grid cases, Figure 38a shows that during the slumping phase, the HR-NR struggles to capture the majority of velocity fluctuations near the current head, in contrast to the reference case. As a result, the simulation fails to accurately reproduce the erosive potential of the current during this phase. Conversely, the HR-WM-S case exhibits improved performance in this region. Although HR-WM-S reproduces the characteristic elongated structures, the near-wall region reveals structures that are larger in the spanwise direction. This is a common effect of wall-functions, due to the resolution, artificially amplified turbulent structures develop near the wall, exhibiting unphysical characteristics in the horizontal directions ([68, 9]). At later time instances, the HR-NR configuration exhibits enhanced capability in reproducing velocity fluctuations, particularly in the vicinity of the current head.

The behavior approaches that observed for the HR-WM-S case, with both

deviating from the resolved case in terms of the spanwise extent of these structures. It is also evident that the coarse grid cases exhibit high fluctuation levels even in the tail of the current, compared to the HR-FR case. This aspect is consistent with the greater tail thickness observed in Figure 32 and with the friction velocity shown in Figure 33.

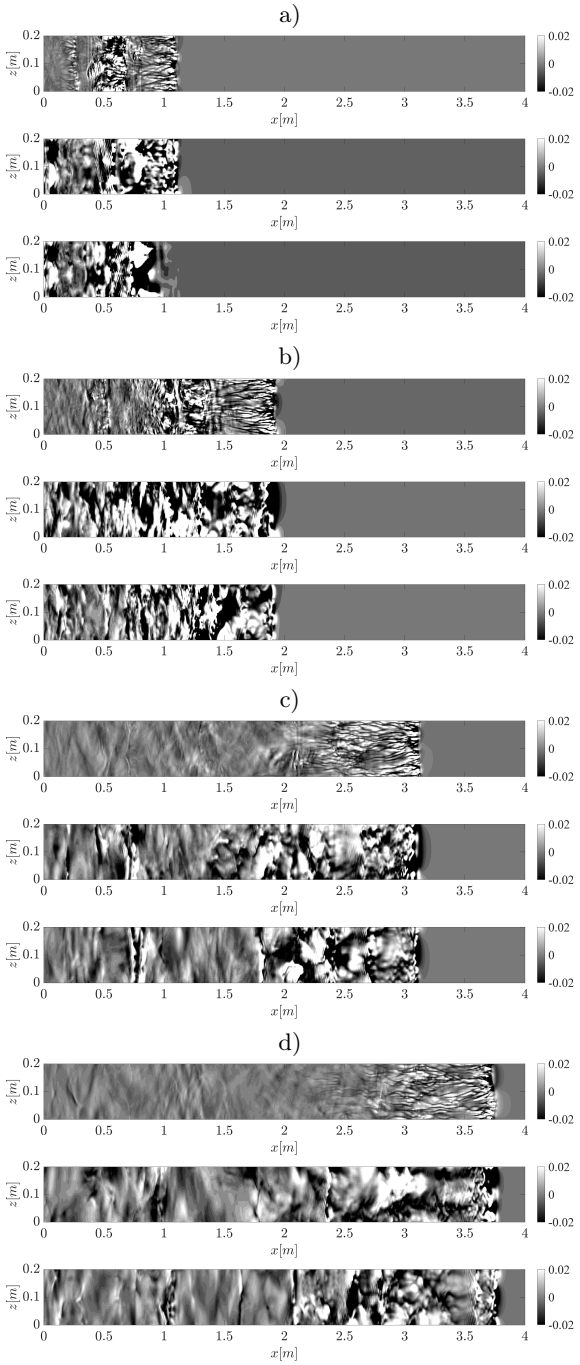

Figure 38: Dimensionless velocity fluctuation at the first cell above the bottom wall, at different times, a confrontation between HR-FR case (top), HR-WM-S case (center) and HR-NR case (down): a) time $T^* = 23.8$, b) time $T^* = 47.6$, c) time $T^* = 91.8$, d) time $T^* = 119$.

6 Results for sediment-laden flow: interaction with bottom structure

6.1 Saline and low-concentration Turbidity Currents

This chapter analyses the results of a lock-exchange gravity current interacting with a submerged cylindrical obstacle. The analysis begins with a comparison between the simulated front positions, obtained using two different numerical solvers (see Section 3), and experimental measurements, obtained by the experiments done in Roma Tre University (see [51]), to assess the model's ability to reproduce the temporal evolution of the flow. This is followed by a qualitative comparison of two-dimensional density fields to verify the consistency of the simulated current structure with laboratory observations. Finally, the results are analysed in terms of entrainment, providing deeper insight into the temporal evolution of the current area and its dilution through mixing with the ambient fluid.

6.1.1 Flow Topology

This section compares the simulated front position, obtained with two different solvers, with experimental data provided by the Hydraulics Laboratory of Roma Tre University. Results from *buoyantBoussinesqPimpleFoam* and *SedFoam* are labelled as *RUN 1 - B* (saline current) and *RUN 2 - S* (low-concentration turbidity current with identical $\Delta\rho$ but generated using light particles), respectively.

In the numerical simulations, the front position x_f is determined following the procedure described in Section 5.3.1. In the experimental analysis, $x_f(t)$ is identified as the maximum streamwise coordinate measured along the lateral section at which the normalized density $\rho^* = 0.02$ is reached. Although the same density threshold is employed in both approaches, the methodologies differ: numerical simulations involve spatial averaging in the spanwise direction, whereas experiments rely on local measurements within the lateral plane. The temporal evolution of the front position is presented in Figure 39.

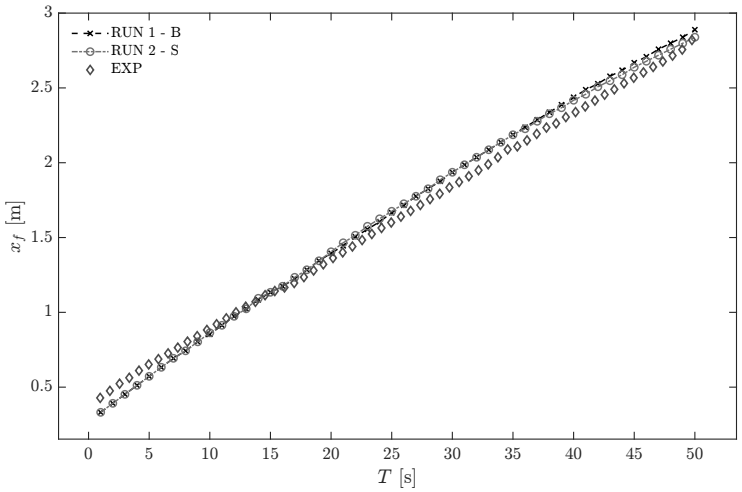

Figure 39: Temporal evolution of the front position from *buoyantBoussinesqPimpleFoam (RUN 1 - B)*, *SedFoam (RUN 2 - S)*, and experimental data (*EXP*).

In Figure 39 the temporal evolution of the front obtained from the numerical simulations is compared with the front position tracked during the laboratory experiments. A maximum discrepancy of approximately 5% is observed between the two, with a slightly lower deviation for **RUN-2-S**.

This discrepancy can be attributed to several contributing factors. First, *cyclic* boundary conditions were imposed on the lateral boundaries of the computational domain. This choice was made to avoid further refinement of the mesh in the spanwise direction, which would have led to a significant increase in computational cost. The `cyclic` condition enforces perfect field periodicity, allowing the outflow to re-enter the domain without energy dissipation due to wall friction. As a result, the simulated current retains a higher level of kinetic energy and propagates slightly faster than its experimental counterpart. This effect becomes evident after the interaction with the cylinder (approximately at $T \approx 15$ s), beyond which the numerically predicted fronts are marginally ahead of those observed experimentally. When the comparison is restricted to this post-interaction phase, the discrepancy is reduced to approximately 3.7% for both numerical solvers.

A second source of error is associated with experimental uncertainty in front detection, arising from both the finite resolution of the measurement instruments and the adopted detection methodology. In addition, the aforementioned differences in the definition of the front position introduce a systematic bias: a local, pointwise measurement tends to underestimate the front location when compared with a spanwise-averaged position, which is more representative in light of the intrinsic spatial inhomogeneity of the current head.

A third factor concerns the initial release mechanism. In the experiment, the

sudden removal of the gate imparts momentum to the current, accelerating its propagation during the early stages. In contrast, the numerical simulations initialise the flow field statically, without reproducing this dynamic impulse, which results in a slower initial propagation and a consequently more attenuated evolution. The influence of a physical gate is clearly addressed in [75], where it is shown that modeling the removal of a physical gate induces a vertical displacement of the adjacent water column, generating an impulse that accelerates the gravity current and promotes the early formation of its head. Accordingly, the largest discrepancies are observed within the first few seconds; when the initial 10 s are excluded, the mean global error decreases to approximately 3.5%. This behaviour is clarified in the dimensionless log-scale representation (see Figure 40).

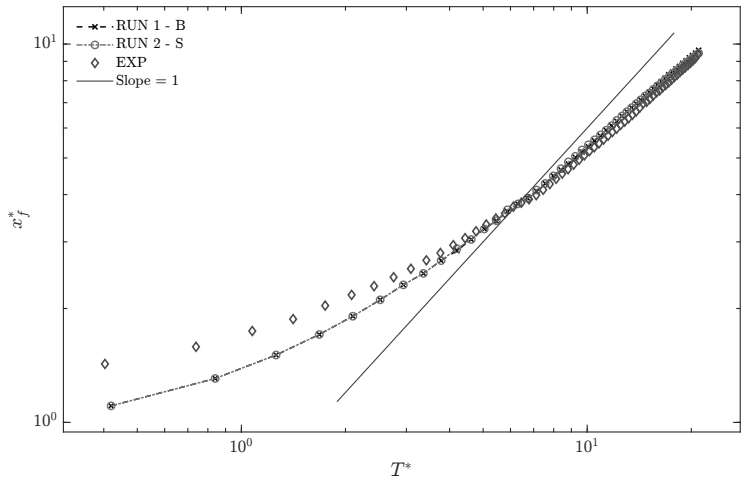

Figure 40: Dimensionless temporal evolution of the front position in log–log scale: *buoyantBoussinesqPimpleFoam (RUN 1 - B)*, *SedFoam (RUN 2 - S)*, and experimental data (*EXP*).

Figure 40 confirms that the initial discrepancy in the release of the heavier fluid contributes to its slower early propagation. However, this effect gradually diminishes over time, and the numerical and experimental cases converge between $T^* \approx 4.2$ and 6.7, corresponding to the period during which the current interacts with the cylinder.

A closer examination of Figure 39 reveals that at $T = 15$ s the flow undergoes a local deceleration due to the collision with the cylinder, after which it rapidly accelerates again. This deceleration occurs as the current climbs over the obstacle, enhancing mixing and turbulence, which dissipates kinetic energy and reduces the subsequent slope of the front position curve. As noted by [51], submerged obstacles induce sequences of climbing and plunging motions in gravity currents, wherein the front rises and then falls back, generating energetic oscillations and increased mixing in the cylinder wake. Returning to Figure 40, it is evident that the slopes of the front position curves are slightly lower than the theoretical slope expected during the slumping phase ($x_f \sim T$), as reported by [34]. This reduction reflects the energy loss associated with the cylinder interaction, which temporarily slows the front.

Overall, the front-position analysis provides a validation of the numerical models. Despite the aforementioned sources of error, the global discrepancy remains limited to approximately 5.0%, and decreases to 3.5% when the initial phase is excluded. These results demonstrate that the implemented LES model accurately captures the overall dynamics of the gravity current, offering a reliable framework for the subsequent analysis of turbulent structures, fluid–obstacle interactions, and derived quantities such as wall-shear velocity and drag coefficient, which are discussed in the following sections.

6.1.2 Density Fields

In this section, the temporal evolution of the nondimensional density fields is compared at selected time instants to assess whether the gravity current dynamics reproduced by the numerical simulations are qualitatively consistent with those observed in the laboratory experiments. The results of this comparison are presented in Figure 41 for six successive time instants, with particular emphasis on the interaction between the current and the cylinder and on the immediately subsequent stages (T^* ranging from 5.04 to 8.40).

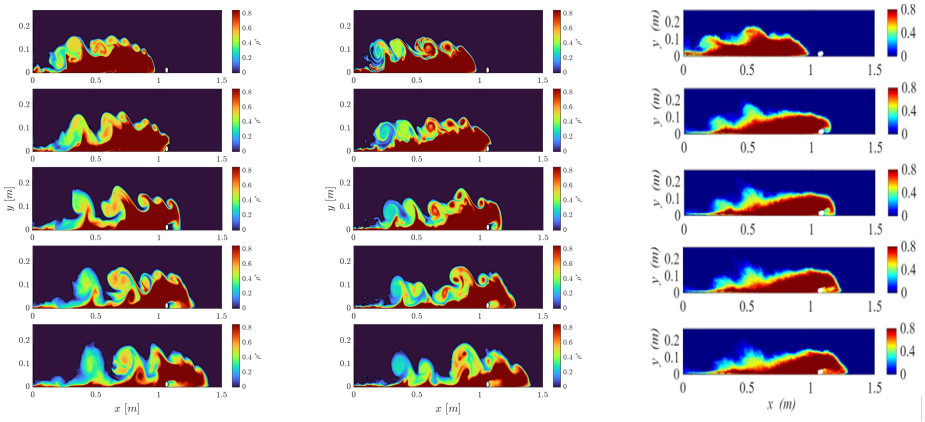

a) b) c)

Figure 41: Comparison of two-dimensional dimensionless density fields at times $T^* = 5.04, 5.88, 6.72, 7.56, 8.40$: a) RUN 1 - B, b) RUN 2 - S, and c) Experimental data.

As described in [51], the experimental density fields in Figure 41 were obtained from lateral recordings of the vertical mid-plane of the channel using an optical light-attenuation technique. The resulting maps show the instantaneous density distribution in the lateral tank plane, enabling comparison with the numerical fields, which are averaged in the spanwise direction.

The morphology of the gravity current remains consistent with that observed in the laboratory experiments. Although the mixing layer appears slightly more diffusive over time, in comparison to the experimental results for both numerical solvers, the bulk structure of the current evolves in close agreement with the reference case. Before impacting the cylinder, the current exhibits a compact head, with interfacial instabilities developing at the boundary with the ambient fluid. These instabilities can be identified as Kelvin-Helmholtz billows, similar to those observed in the experimental configuration and characteristic of the slumping phase.

Upon interaction with the obstacle at $T^* = 5.04$, the current undergoes a pronounced deformation, giving rise to the climbing phenomenon described previously in Section 6.1.1. In all cases, this phase is accompanied by the formation of a recirculation region immediately downstream of the cylinder. This is followed by the so-called plunging phase, during which the current collapses toward the bed and subsequently re-establishes a flow configuration comparable to that observed prior to the impact.

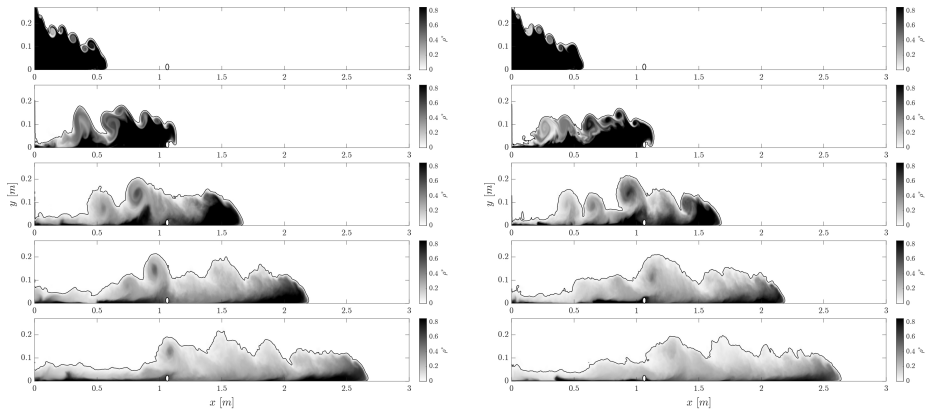

a) b)

Figure 42: Overall evolution of the spanwise-averaged dimensionless density field ρ^* at times $T^* = 2.10, 6.30, 10.50, 14.70, 18.90$: a) RUN 1 - B and b) RUN 2 - S. The $\rho^* = 0.02$ iso-density contour is highlighted.

Focusing now on a broader temporal interval to provide an overall view of the phenomenon, Figure 42 illustrates the evolution of the gravity current obtained with both numerical solvers. Although minor discrepancies are observed, the current simulated with *SedFoam* (Figure 42b), which includes a sediment phase, albeit with small grain size, within the body of the flow, appears less diffusive overall. In this case, the mixing layer at the interface with the ambient fluid is more vortical, and the current is generally more compressed toward the bottom boundary. This behaviour is attributable to the sediment-laden fraction of the flow, which remains relatively compact and tends to deposit along the bed.

In contrast, the simulation performed with *boussinesqPimpleFoam* (Figure 42a) exhibits a slightly more diffuse mixing layer and a greater overall current thickness at all analysed time instants, particularly in the interval $T^* \in [2.10, 10.50]$. At later times, despite the persistence of small differences, the two solutions tend to converge, both displaying a weak reflection of the current toward the left boundary, induced by the interaction with the cylinder.

In conclusion, the qualitative agreement among all datasets confirms the capability of the adopted LES model to reproduce the key physical phenomena related to fluid–obstacle interaction and the mixing processes governing gravity current dynamics. The following section will estimate the entrainment parameter.

6.1.3 Entrainment

The following analysis extends the methodology described in section 5.3.3 for gravity currents by incorporating local quantities. Specifically, the entrainment rate and associated coefficients are evaluated not only in their cumulative (bulk) form but also as local variations between successive time steps t_i and t_{i-1}.

The area A_i is defined as the two-dimensional portion of the current bounded by the contour $\rho^* > 0.02$ at time t_i. The temporal evolution of A_i is shown in Figure 43. For *buoyantBoussinesqPimpleFoam*, the area increases almost linearly throughout the simulation, with slight slope changes near the cylinder. In contrast, *SedFoam* exhibits a more irregular trend and a smaller final area; the reasons for this behaviour are discussed below.

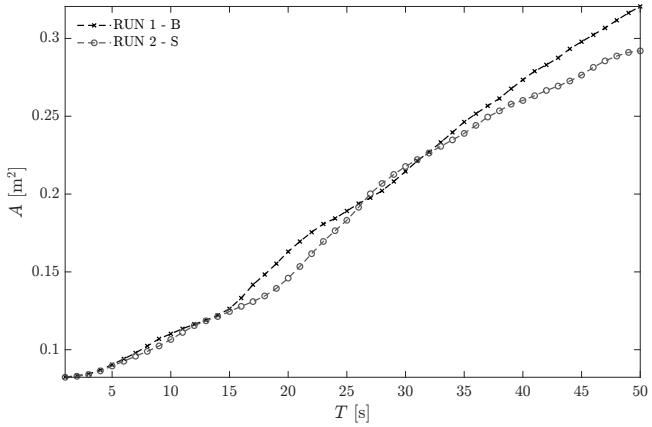

Figure 43: Evolution of the current area $A(t)$ bounded by the $\rho^* = 0.02$ contour for the two solvers.

The temporal evolution of the entrainment rate, reported in Figure 44, is highly irregular and displays substantial differences between the two numerical solvers. During the initial stage of the flow, Q_{ei} increases in an approximately linear manner, consistent with the quasi-steady development of the gravity current. At around $T \approx 14$ s, a marked decrease in the entrainment rate is observed. This reduction corresponds to the climbing phase, during which the current ascends the upstream face of the cylinder, converting part of its kinetic energy into potential energy and thereby reducing its capacity to entrain ambient fluid.

After the current overtops the obstacle, the flow enters the plunging phase, characterised by the descent of dense fluid toward the bed. This phase is associated with the generation of intense turbulence and strong velocity gradients, which significantly enhance mixing processes. In addition, the formation of a vortex wake downstream of the cylinder further promotes entrainment by increasing the interfacial area between the gravity current and the surrounding fluid. The combined effects of plunging and wake-induced turbulence result in a pronounced peak in the local entrainment rate Q_{ei}^{local}, as well as in the

entrainment coefficients E_{bulk} and E_{local}, as shown in Figure 45.

A notable difference between the two solvers is the timing of this peak, which occurs approximately 8 s later in the *SedFoam* simulations than in the *buoyantBoussinesqPimpleFoam* results. Furthermore, in agreement with earlier observations, *SedFoam* systematically predicts lower entrainment levels. This behaviour is attributable to the two-phase formulation of the solver: sediment particles possess inertia, do not instantaneously follow fluid fluctuations, and tend to settle toward the bed. Consequently, a fraction of the available energy is expended in mobilising and redistributing the sediment phase, which delays the development of turbulent structures and slightly attenuates their intensity.

The enhanced entrainment observed in both solvers constitutes the main qualitative difference between the present obstructed configuration and the unobstructed cases analysed by [63] and [51], where entrainment evolves in a more regular and monotonic fashion. In the present study, the interaction with the cylinder fundamentally modifies the current dynamics, in line with previous investigations of gravity currents interacting with submerged obstacles ([94, 2]). These findings highlight the strong sensitivity of entrainment processes to bed topography and obstacle geometry, demonstrating that even a single morphological discontinuity can exert a significant influence on the mixing intensity of a gravity current.

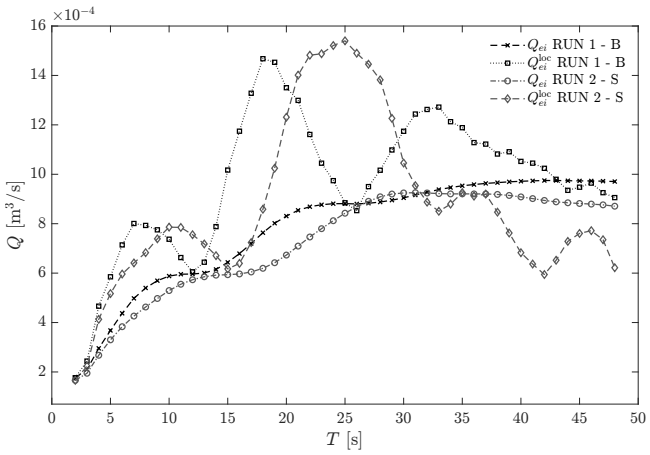

Figure 44: Global $Q_{ei}(t)$ and local Q_{ei}^{local} entrainment rates over time for the two solvers.

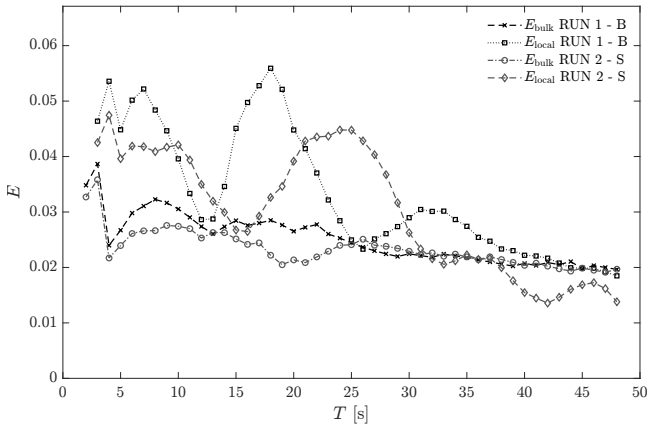

Figure 45: Temporal evolution of the global and local entrainment coefficients for the two solvers.

6.2 Turbidity Current

Once both numerical solvers had been validated, the two-phase solver was selected to reproduce a turbidity current in a lock-exchange configuration (**RUN-3-T**). In particular, *SedFoam* is well suited for this type of flow, as it explicitly accounts for the presence of sediments within the body of the current through an Eulerian two-phase modelling approach (see Section 3.1.2).

As in the two previous simulations, the front position was first analysed as a function of time and then compared with the other cases to assess how the increased density affects the current dynamics. To this end, the analysis of the density fields and the entrainment behavior proved to be especially informative.

Subsequently, the wall-shear velocity and the Shields parameter are examined to estimate the erosive capacity of the current. Finally, the drag and lift forces exerted by the flow on the cylinder are evaluated.

6.2.1 Flow topology

The first parameter analysed is the front position. For the turbidity current simulation, a density increment of $\Delta\rho = 180\ \mathrm{kg\,m^{-3}}$ was imposed, which is significantly larger than in the saline cases. This increase results in a buoyancy velocity of $u_b \approx 0.690\ \mathrm{m\,s^{-1}}$, approximately six times greater than that of the saline currents, and consequently leads to a markedly faster propagation.

The enhanced buoyancy force induces a substantial acceleration of the front, which reaches the obstacle in approximately 2.5 s. Over this time span, the turbidity current travels a distance comparable to that covered by the **RUN-1-B** and **RUN-2-S** experiments in about 8 s, i.e. roughly 32 s less than in the saline cases. This behaviour is clearly illustrated in Figure 46, where a local deceleration of the front—albeit less pronounced owing to the higher current velocity—is again observed at around $T \approx 2.5$ s, corresponding to the impact of the current

head with the cylindrical obstacle. During the quasi-steady propagation phase, the mean bulk velocity of the turbidity current is $U_{\text{bulk}} = 0.266\ \text{m}\,\text{s}^{-1}$, which is approximately five times larger than the values obtained for the saline cases ($U_{\text{bulk}} \approx 0.05\ \text{m}\,\text{s}^{-1}$).

In contrast to the saline currents, the turbidity current exhibits a more pronounced deceleration during the final stage of propagation. This behaviour is associated with the progressive deposition of sediment, which leads to a gradual loss of momentum and a reduction in the front propagation speed.

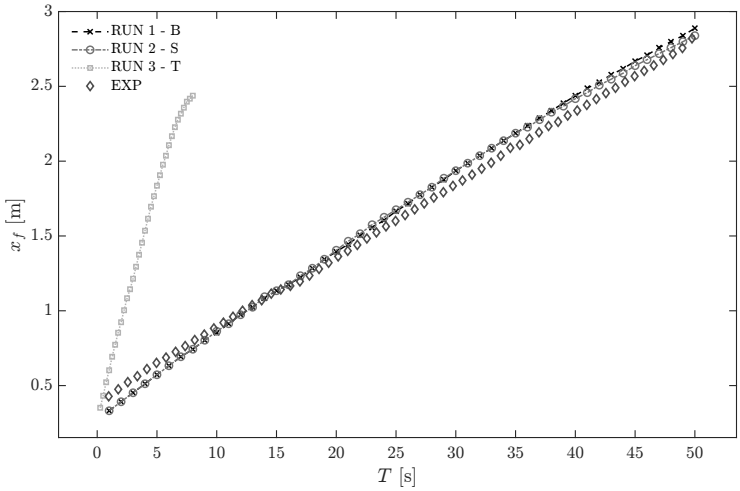

Figure 46: Temporal evolution of the front position for *RUN 1 - B*, *RUN 2 - S*, experimental data (EXP), and the turbidity current *(RUN 3 - T)*.

Turning to the logarithmic representation of the front position (Figure 47), it can be observed that the front evolution curve lies entirely within the slumping phase and that the data correctly converge toward the expected scaling behaviour. The slope of the nearly linear segment is slightly smaller than unity, in agreement with the previous cases and attributable to the interaction with the cylindrical obstacle.

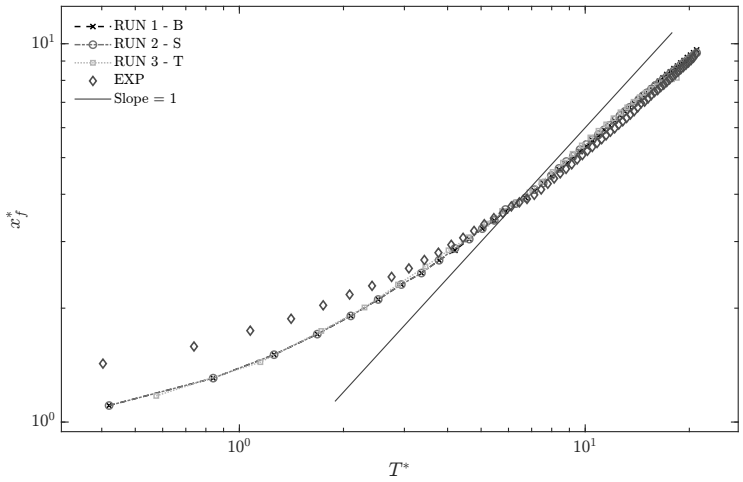

Figure 47: Dimensionless temporal evolution of the front position on a logarithmic scale for *RUN 1 - B*, *RUN 2 - S*, experimental data (EXP), and the turbidity current *(RUN 3 - T)*.

6.2.2 Density Fields

As in the previous cases, the analysis now focuses on a qualitative examination of the density fields, which are particularly informative for describing the evolution of the gravity current. The interaction between the current and the cylinder is first examined (see Figure 48a), followed by an assessment of the global behaviour of the flow, illustrated in Figure 48b.

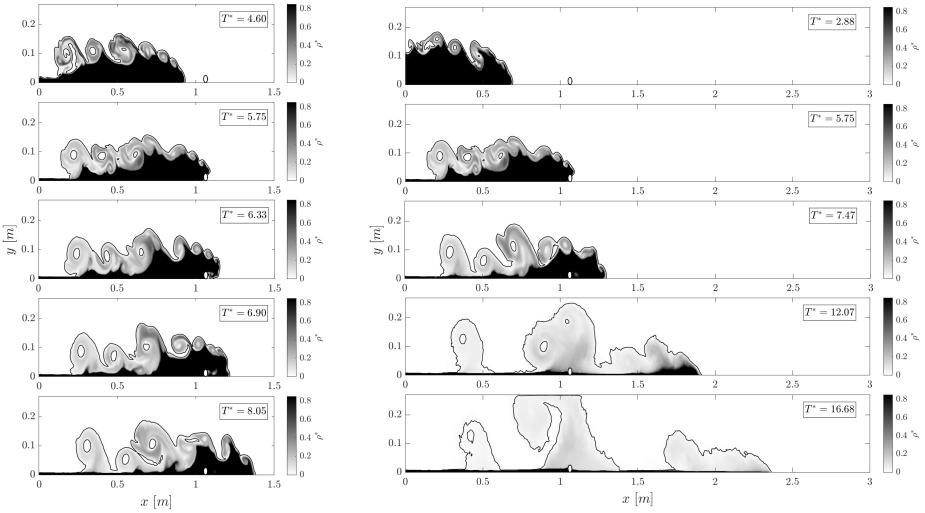

a) b)

Figure 48: Two-dimensional density fields averaged along the z-direction: a) focus on the cylinder-interaction phase (from $T^* = 4.6$ to $T^* = 8.05$) and b) wide-range temporal evolution (from $T^* = 2.88$ to $T^* = 16.68$).

Figure 48a shows that the processes described in Section 6.1.2 also occur in the turbidity current, although with marked differences due to the higher propagation velocity and the presence of a solid phase. Before interacting with the cylinder, the current front is well defined and inclined, with a compact head characterized by a sharp density gradient. At $T^* = 5.75$, the climbing phase is clearly observed, as the current ascends the upstream face of the obstacle. This stage is followed by the plunging phase at $T^* = 6.33$, during which dense fluid collapses toward the bed downstream of the cylinder. After the interaction, the front gradually recovers its original shape and inclination.

Once the cylinder is overtopped, the impact with the bed occurs farther downstream compared to the saline cases. The higher propagation velocity allows suspended particles to be transported over longer distances before settling, delaying the onset of deposition.

The local dynamics observed in the vicinity of the obstacle are embedded within a broader temporal evolution, illustrated in Figure 48b, which highlights how the cylinder interaction influences the structure of the current at later stages. During the early phases, $T^* = 2.88$ and 5.17, the turbidity current exhibits a well developed head and a dense basal layer flowing along the bed, in close analogy with the saline cases. At $T^* = 7.47$, immediately after the obstacle is overtopped, the front undergoes a pronounced deformation and a dense wake develops downstream of the cylinder, where larger and more coherent vortical structures emerge and the near bed dense layer progressively thickens as sediment begins to accumulate.

In the later stages, $T^* = 12.07$ and 16.68, the current progressively loses its initial compactness. The head fragments into multiple lobes and the density field becomes increasingly irregular and diffuse. In the final snapshot, the densest material is no longer concentrated within a single coherent core, but is instead distributed across several regions of the domain, indicating an advanced stage of mixing and sediment deposition. This behavior is consistent with the high initial intensity of the turbidity current, which enhances mixing processes and accelerates the breakdown of the original current structure during the final stages of the evolution.

6.2.3 Entrainment

Turning now to the temporal evolution of entrainment, the parameter is evaluated following the same approach adopted in the previous cases, by distinguishing between a local contribution, associated with instantaneous variations in the area occupied by the current, and a bulk contribution, derived from the overall evolution of the dense-fluid volume within the domain.

Figure 49 reveals a behavior that reflects the strongly impulsive nature of the turbidity current. Entrainment increases rapidly during the very early stages, reaching initial values that are higher than those observed in the saline cases. After the peak associated with the passage of the current over the cylinder ($T \approx 2.75$ s), the local contribution does not exhibit a pronounced decrease; instead, E_{local} tends to stabilise, remaining at nearly constant values in the range 0.015–0.020. This trend indicates that, although the current progressively loses coherence, a sustained level of mixing persists over a significant portion of the simulation.

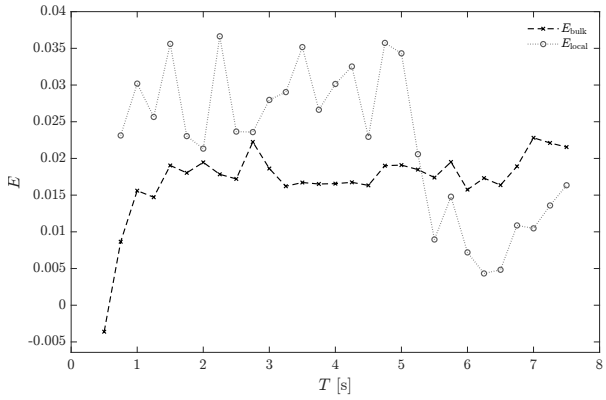

Figure 49: Temporal evolution of bulk and local entrainment for the turbidity current.

The evolution of the two-dimensional area A is shown in Figure 50. The area increases almost linearly until about $T = 5$ s, consistent with the intense initial entrainment and the entrainment action exerted by the current head. Beyond

this phase, A tends to stabilize: the current elongates, fragments, and progressively loses compactness, as already observed in the density fields. Only in the final instants is a slight area reduction noted, attributable to sedimentation and the dissipation of mixing motions.

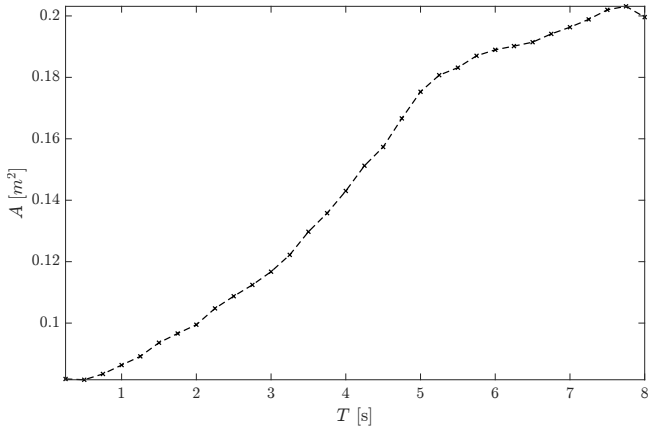

Figure 50: Two-dimensional current area A as a function of time.

The bulk entrainment rate, $Q_{e,i}$, is reported in Figure 51. Its evolution is more variable than in the saline cases: following an initial rapid increase, the parameter continues to grow more gradually, reaching maximum values around $T \approx 5$–5.5 s. In the later stages of the simulation, $Q_{e,i}$ decreases, reflecting the progressive loss of head coherence and the irregular distribution of suspended material downstream of the cylinder. In contrast to the local contribution, $Q_{e,i}$ does not exhibit a well-defined quasi-steady phase, instead capturing the highly dynamic and fragmented evolution of the current in its advanced stages.

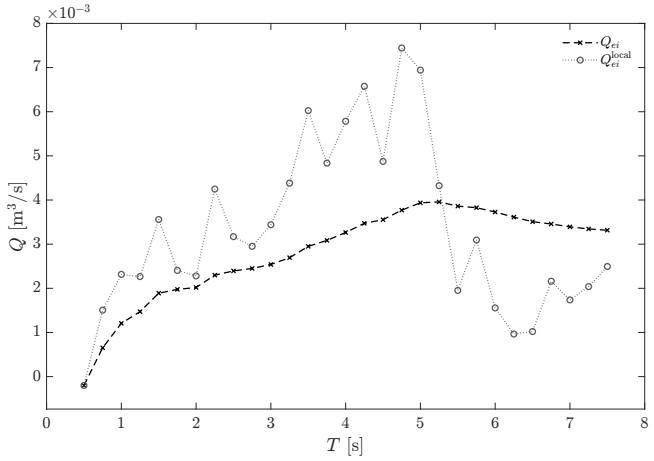

Figure 51: Temporal evolution of the entrainment parameter $Q_{e,i}$ for the turbidity current.

Overall, the entrainment behavior of the turbidity current is characterized by substantially higher magnitudes and significantly shorter characteristic times compared with the saline cases. The local entrainment contribution stabilizes shortly after the initial peak, indicating that intense mixing persists throughout a considerable portion of the current's evolution. In contrast, the bulk entrainment measure exhibits a more irregular pattern, reflecting the rapid loss of coherence in the current structure. Interaction with the cylinder temporarily enhances mixing, yet the inherently energetic nature of the turbidity current concentrates the bulk of entrainment activity within the early propagation stages, emphasizing the dominant role of the initial impulsive dynamics.

6.2.4 Wall-Shear Stresses

Streamwise distribution: The following analyses aim to assess the erosive potential of the turbidity current. In particular, investigating the wall-shear velocity, u_τ, allows identification of regions where peaks occur due to gradients of the streamwise velocity along the y-direction, corresponding to locations of elevated tangential stress at the bed, as discussed in Section 5.1.2.

Figure 52 presents the evolution of $u_\tau(x)$, averaged along the z-direction and normalised by the buoyancy velocity u_b.

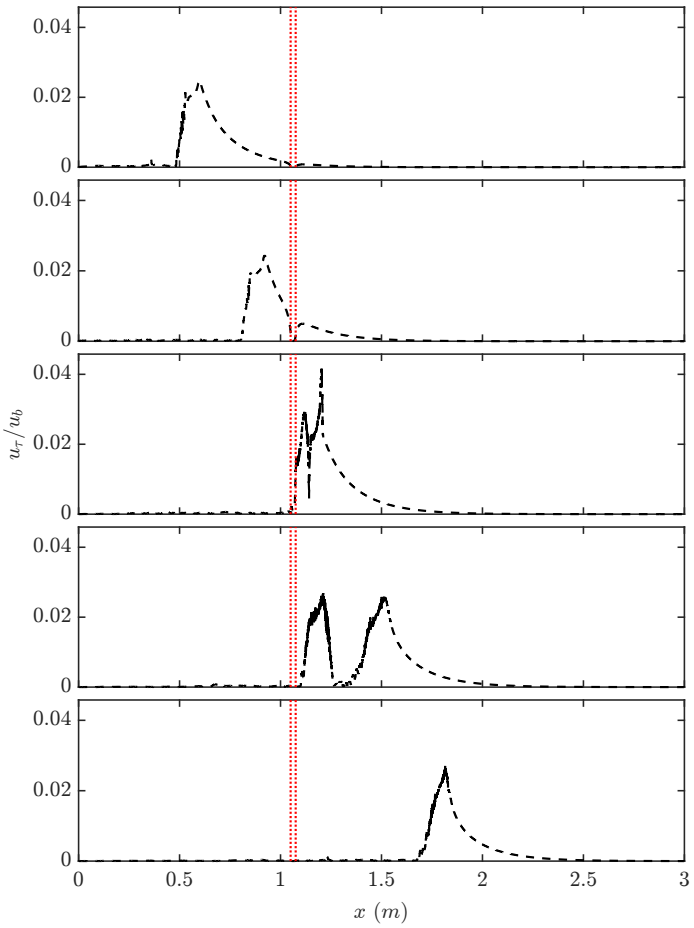

Figure 52: Temporal evolution of the normalised wall-shear velocity u_τ/u_b, averaged along the z-direction, plotted from $T^* = 2.88$ to $T^* = 16.68$. Vertical red lines indicate the position of the cylindrical obstacle.

Figure 52 illustrates that the turbidity current attains its maximum erosive potential at the head, with u_τ reaching peak values of approximately 0.01 just

before impacting the cylinder. In the subsequent instants, particularly at $T =$ 3–4 s, u_τ generally has a slight increase. Moreover, a distinct region of elevated wall-shear forms downstream of the cylinder, which is not associated with the current head but is likely caused by the recirculating flow generated immediately after the current overtops the obstacle. This downstream high-stress region will be analyzed in detail in the following sections.

Planar Distribution at the Bed: Figure 53 presents the distribution of the normalised wall-shear velocity on the x–z bed plane at the same time instants.

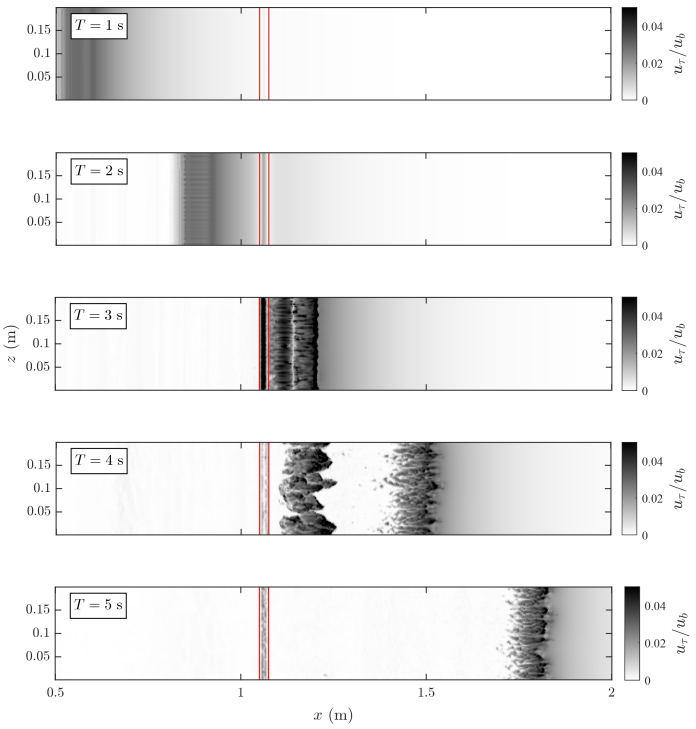

Figure 53: Temporal evolution of the normalised wall-shear velocity u_τ/u_b on the x–z plane. Vertical red lines indicate the position of the cylindrical obstacle.

The trend highlights a clear pattern, with the current's erosive potential concentrated at the head and immediately downstream of the cylinder, where two fronts of erosion are observable, due to the plunging action that amplifies wall-shear. This behaviour is consistent with what was observed in the previous cases. In contrast, the tail of the current shows a sharp decline in u_τ, which can be attributed to rapid sediment settling. The relatively dense particles ($\rho_s = 2650\ \mathrm{kg\,m^{-3}}$) deposit quickly, dissipating energy and reducing the wall-shear velocity in the calmer regions of the flow.

6.2.5 Shields Parameter

Given the spatial distribution of the wall-shear velocity, the erosive potential of the flow can be assessed using the Shields parameter, θ, defined as

$$\theta = \frac{\tau_w}{(\rho_1 - \rho_0)\, g\, d} = \frac{\rho_0\, u_\tau^2}{(\rho_1 - \rho_0)\, g\, d_p} \tag{48}$$

where d_p is the mean particle diameter at the domain bottom. Introduced by [78], this dimensionless parameter represents the ratio between the destabilising drag exerted by the flow and the stabilising submerged weight of the particles, providing a classical criterion for estimating the onset of sediment motion. Under the present conditions, fully turbulent flow, a uniform grain-size distribution, and a flat bed, the critical threshold can be taken as $\theta_{cr} = 0.056$, a representative value for turbulent flows [78].

As the Shields parameter must be evaluated with reference to a specific grain-size class, the analysis was performed for four representative sand diameters, $d_p = 0.2$ mm, 0.5 mm, 1.0 mm, and 2.0 mm, covering the range from fine sand to the upper limit of coarse sand. An analogous assessment was carried out for the previous cases, and in all instances, the results indicate that the currents are not capable of inducing erosion of the domain bed.

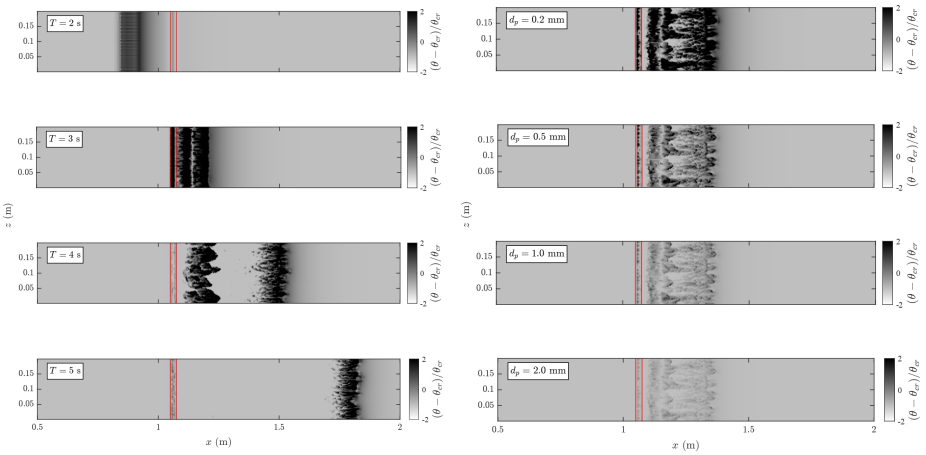

a) b)

Figure 54: Two-dimensional fields of the normalized Shields excess: a) temporal evolution at $d = 0.2mm$; b) dependence on the mean bed-sediment diameter at $T = 3.5s$.

Figure 54 provides a clearer representation of the regions where the flow exhibits erosive or depositional behavior through the normalized Shields excess, $(\theta - \theta_{cr})/\theta_{cr}$. Positive values identify areas where the critical threshold for

sediment motion is exceeded, and erosion is expected, whereas negative or zero values correspond to depositional regions.

The temporal evolution of the normalized Shields excess is shown in Figure 54a. The turbidity current potential erosion on the bed increases during the passage of the head and in the region downstream of the cylinder, in agreement with the wall-shear stress analysis (see Section 6.2.4). A noteworthy feature appears at $T = 4$ s: in the immediate vicinity of the obstacle, the Shields parameter remains below the critical threshold, while erosion develops slightly farther downstream. As previously discussed in the context of wall-shear stresses, this behaviour suggests that during the plunging phase, the dense fluid mass overshoots the obstacle, generating a localized recirculation region immediately downstream of the cylinder. This recirculation promotes deposition very close to the obstacle and shifts the zone of maximum erosion slightly further downstream.

The effect of the mean bed-sediment diameter on the erosive potential is illustrated in Figure 54b for $T = 3.5s$. As the particle size increases, the extent and intensity of the erosive regions progressively decrease, reflecting the higher critical stress required to mobilise coarser material.

This behavior is further illustrated in Figure 55, which shows the temporal evolution of the maximum normalized Shields excess for different mean bed diameters. Before the interaction with the cylinder, θ remains low for all sediment sizes. At $T = 2.5$ s, a sharp increase is observed, leading to a peak around $T = 4$ s, which corresponds to the phase during which the interaction with the obstacle produces the strongest enhancement of wall shear stresses. For all analyzed diameters, the critical threshold is exceeded in at least limited portions of the bed, although the spatial extent of erosion progressively decreases with increasing particle size. Notably, after the cylinder interaction, the Shields excess values remain systematically higher than in the pre-impact phase. This indicates that the obstacle not only intensifies the immediate erosive capacity of the flow downstream but also sustains elevated shear stresses in subsequent stages, thereby prolonging the temporal extent of the current's erosive influence.

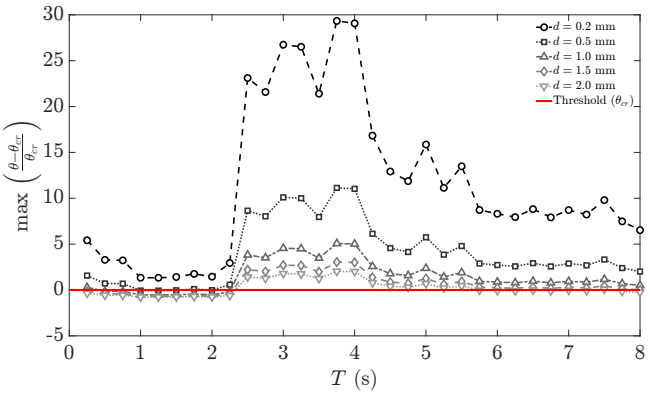

Figure 55: Temporal evolution of the normalized Shields excess for varying diameters, compared with the critical value (red line).

To gain further insight into the flow dynamics around the cylinder, it is instructive to examine the distribution of the solid volume fraction, α_a, defined as the proportion of the local volume occupied by particles relative to the total volume. Regions with high α_a indicate either significant sediment accumulation or intense particle suspension, whereas values approaching zero correspond to zones effectively free of solid material.

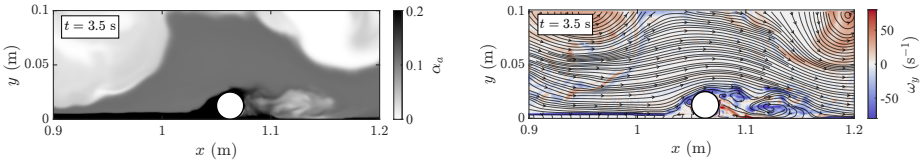

a) b)

Figure 56: Evolution of the flow field at $T = 3.5$ s: a) solid volume fraction α_a on the x–z plane at the central section; b) streamlines superimposed to the vorticity field during cylinder interaction.

Figure 56 shows that, after passing the cylinder, the current generates a vortex cell in the region immediately downstream. This recirculation strongly influences sediment distribution: part of the material is transported back toward the cylinder, forming a well-defined accumulation visible in the α_a map, while another portion is carried further downstream, contributing to sediment transport and redistribution in the central area immediately behind the obstacle.

The streamlines clearly illustrate this behaviour, showing how the flow circulates within the wake and redistributes solid material both near the cylinder and along the primary current path.

These observations confirm a consistent pattern: a localized accumulation of

sediment along the cylinder edge, a reduction of the solid fraction in the central wake region, and intense erosion immediately downstream, all consistent with the recirculation generated by the obstacle. From this analysis, it is evident that interaction with the cylinder not only enhances the current's erosive capacity during impact but also creates a zone of elevated scour risk downstream, where the recirculating flow produces maximum shear values.

6.2.6 Drag and Lift Forces

The following section presents the analysis of the forces exerted by the current on the cylinder, a fundamental quantity for assessing potential impacts on structural stability. The total force imparted by the current is defined as

$$\mathbf{F} = \int_{A_{\mathrm{cyl}}} \Big[-\, p_d\, \mathbf{n} \;+\; \boldsymbol{\tau} \cdot \mathbf{n} \Big]\, \mathrm{d}A; \qquad \boldsymbol{\tau} = \mu_{\mathrm{eff}} \left(\nabla \mathbf{u} + \nabla \mathbf{u}^T \right) \tag{49}$$

where A_{cyl} is the wetted surface of the cylinder, p_d is the hydrodynamic pressure on the wall, and $\mathbf{n}$ is the outward-pointing unit normal. The total force $\mathbf{F}$ can be decomposed into streamwise and vertical components to obtain the drag and lift, respectively:

$$F_D = \mathbf{F} \cdot \mathbf{e}_x; \qquad F_L = \mathbf{F} \cdot \mathbf{e}_y \tag{50}$$

where $\mathbf{e}_x$ is aligned with the current propagation direction and $\mathbf{e}_y$ is oriented vertically. The corresponding dimensionless drag and lift coefficients, which allow a scale-independent comparison, are defined as

$$C_D = \frac{F_D}{\frac{1}{2}\,\rho_0\, U_{\mathrm{bulk}}^2\, A_{\mathrm{ref}}}; \qquad C_L = \frac{F_L}{\frac{1}{2}\,\rho_0\, U_{\mathrm{bulk}}^2\, A_{\mathrm{ref}}} \tag{51}$$

with $A_{\mathrm{ref}} = d\, L_z$ representing the projected cylinder area, based on its diameter $d = 0.025$ m and length $L_z = 0.2$ m normal to the flow direction.

Figure 57 compares the drag and lift forces for the present turbidity current simulation (*RUN-3-T*) and the previous low-concentration turbidity case (*RUN-2-S*). The two cases are compared using the dimensionless time T^* to ensure consistent temporal scaling. The drag (F_D) and lift (F_L) forces are plotted on a logarithmic scale. A constant shift C was applied to the signals to avoid negative values and enable logarithmic representation. This approach facilitates a clearer comparison between the two cases and highlights differences in both magnitude and temporal evolution of the forces. Note that the density difference in the low-concentration case was $\Delta\rho = 6\ \mathrm{kg\,m^{-3}}$, whereas in the present turbidity current case it is approximately thirty times larger.

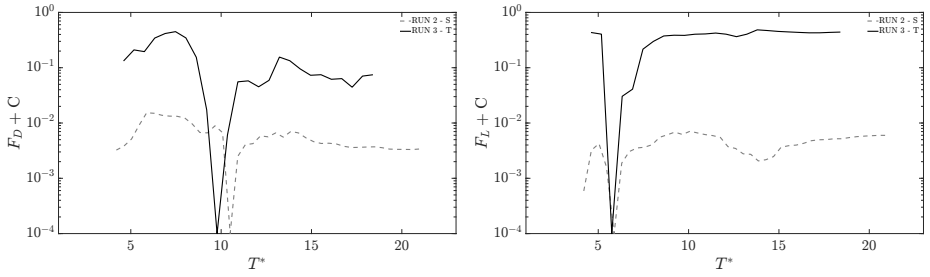

a) b)

Figure 57: Comparison of drag a) and lift b) forces, shifted by a coefficient C to be plotted in logarithmic scale from the two simulations (*RUN 2 – S, RUN 3 – T*).

Forces in the turbidity current case are substantially larger than in the low-concentration turbidity current. The markedly higher density gradient ($\Delta\rho \approx 180\ \mathrm{kg\,m^{-3}}$) leads to thrust values that are approximately three orders of magnitude greater, reflecting both the increased weight of the dense fluid and the resulting intensification of the flow in the vicinity of the cylinder.

Despite the substantial difference in force magnitude, the temporal evolution of drag and lift is qualitatively very similar in the two cases. In both simulations, a pronounced positive peak in the lift force F_L occurs as the turbidity current approaches the cylinder. This peak is associated with the displacement of the ambient fluid in the wall-normal direction induced by the advancing current head, which generates an upward vertical force on the obstacle. During this approach phase, the drag force F_D remains comparatively steady.

When the turbidity current subsequently impacts the cylinder, F_D reaches its maximum value, while F_L rapidly decreases and attains a minimum, assuming negative values when the logarithmic shift is removed. This minimum corresponds to a strong downward vertical force whose magnitude is comparable to that of the horizontal drag. In the post-impact phase, the two force components evolve in a largely specular manner, reflecting the unsteady wake dynamics and the vortex structures generated by plunging downstream of the obstacle. As the turbidity current propagates farther downstream, both F_D and F_L gradually approach a plateau and tend toward values close to zero, neglecting the constant shift C introduced solely for logarithmic representation.

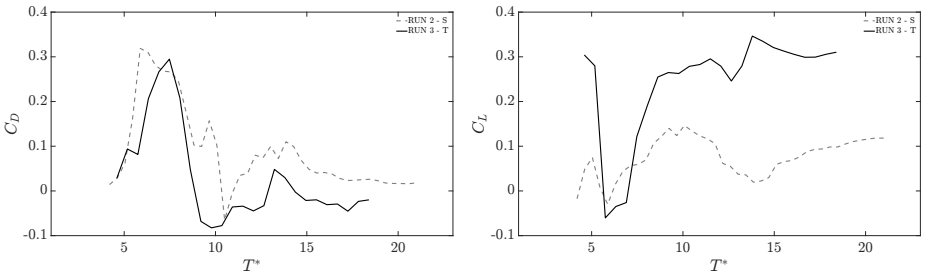

a) b)

Figure 58: Dimensionless drag and lift coefficients from $T = 2s$ onward.

Figure 58 presents the same comparison discussed above, now expressed in terms of the dimensionless drag and lift coefficients, C_D and C_L, normalized by the respective bulk velocities of the two cases. This normalization enables a direct comparison between the low-concentration turbidity case and the present turbidity current by placing the force responses on a common, non-dimensional scale.

The turbidity current exhibits a temporal evolution of both coefficients that is qualitatively consistent with the low-concentration turbidity case, characterized by a distinct peak at the moment of head impact followed by oscillations associated with the development of a vortex wake downstream of the cylinder. The peaks in C_D are slightly shifted in dimensionless time, an effect that can be attributed to differences in temporal resolution between the two datasets, namely a sampling interval of 1 s for the saline plume and 0.25 s for the turbidity current. Despite this minor phase shift, the peak values of both C_D and C_L remain of comparable magnitude in the two cases.

Consistent with the logarithmic representation of the dimensional forces, the maximum lift coefficient assumes negative values, indicating the presence of a downward vertical force whose intensity is comparable to that of the horizontal drag. This downward thrust arises from the fall-back of the dense current during its interaction with the obstacle and is closely linked to the plunging dynamics and the formation of coherent vortical structures. Such behavior is in agreement with observations reported in the literature for high-density gravity currents [16], where vortex-induced pressure fluctuations are shown to amplify both horizontal and vertical force components.

Overall, these results demonstrate that, in turbidity currents, the lift force cannot be neglected. When combined with the enhanced scouring processes discussed previously, the vertical loading may play a critical role in modifying basal support conditions and in determining the structural loads experienced by submerged obstacles.

7 Results for hyperpycnal flow: plunging point and mixing layer

This chapter presents an analysis of plunging dynamics based on data from laboratory experiments conducted at the LEGI laboratory in Grenoble. The analysis was performed during a seven-month research stay abroad undertaken as part of the doctoral programme, which included direct observation of the experiments but no involvement in their design, execution, or data acquisition.

7.1 Determination of the plunging point

As discussed in Section 1, determining the plunging point of a hyperpycnal plume generated by river inflow is essential for understanding how inflow dynamics vary with changes in channel width. Conventionally, this point is identified using the layer-averaged plume thickness, h_0, as defined in Eq. 52, following the approach proposed by [18] and later applied in [77]:

$$h_0 = \frac{\left(\int_{z_b}^{z_0} \bar{u}\, dz\right)^2}{\int_{z_b}^{z_0} \bar{u}^2\, dz} \tag{52}$$

here, z_b denotes the depth of the bottom boundary, and z_0 represents the elevation at which $\bar{u}$, the time-averaged longitudinal velocity, reduces to zero. Ideally, the h_0 profile exhibits a clear peak followed by a sharp decline, with the peak corresponding to the plunging point (see Figure 59). However, when this method is applied to the central vertical slice of the experimental dataset (see Figure 8), where the leading edge of the inertial current leaving the channel becomes permanently detached from the free surface, the longitudinal velocity does not decay to zero. Consequently, the h_0 trend continues to increase without showing a subsequent decrease, rendering this approach unreliable for the present case.

For this reason, a key contribution of this work lies in the analysis of the first horizontal data slice (see Figure 7), corresponding to the surface layer of the domain, with the objective of developing a robust method to identify the point at which the current completely detaches from the surface.

To achieve this, the main flow was characterized to identify the dominant turbulence field, thereby enabling the localization of the detachment region of the main flow. For an effective visualization of turbulence associated with vorticity and strain, the Q-criterion was employed.

The Q-criterion [33, 12] is a well-established method for identifying vortical structures in turbulent flows. It relies on the decomposition of the velocity gradient tensor, $\nabla \mathbf{u} = \mathbf{S} + \mathbf{\Omega}$, where $\mathbf{S}$ is the symmetric rate-of-strain tensor (S_{ij} see Section 3.1.1) and $\mathbf{\Omega}$ is the antisymmetric rotation tensor, $\Omega_{ij} = \frac{1}{2}\left(\frac{\partial u_i}{\partial x_j} - \frac{\partial u_j}{\partial x_i}\right)$. The Q-criterion is defined as:

$$Q = \frac{1}{2}\left(\|\mathbf{\Omega}\|^2 - \|\mathbf{S}\|^2\right)$$

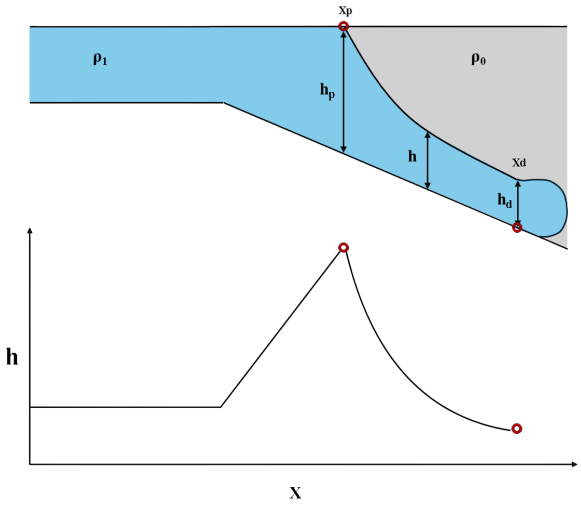

Figure 59: Qualitative trend of the plume height along the streamwise direction. x_p and h_p denote the plunging point and plunging depth, marking where the plume fully detaches from the surface, while x_d and h_d indicate the position and depth at which the saline plume has completely decayed along the sloping bed.

where $\|\mathbf{S}\|^2 = S_{ij}S_{ij}$ and $\|\mathbf{\Omega}\|^2 = \Omega_{ij}\Omega_{ij}$. Regions where $Q > 0$ correspond to zones in which the local rotation rate exceeds the strain rate, indicating the presence of coherent vortical structures. For incompressible flows, Q can also be expressed in terms of the vorticity vector, $\omega_i = \epsilon_{ijk}\partial u_k/\partial x_j$, as

$$Q = \frac{1}{8}\omega_i\omega_i - \frac{1}{2}S_{ij}S_{ij}$$

Compared to other vortex-identification methods, such as the λ_2 and Δ criteria [38], the Q-criterion provides a direct, Galilean-invariant measure of the local flow topology and effectively highlights coherent structures within turbulent regions. By applying this approach, the primary flow regions are identified as zones where $Q \approx 0$, corresponding to regions of dominant strain rather than rotation. In contrast, the mixing layer exhibits elevated vorticity, indicative of strong shear and enhanced turbulent entrainment at the interface between the dense and ambient fluids. This distinction allows for a clear identification of the onset of current decay, both along the lateral margins and within the central core of the gravity current, thereby elucidating the spatial transition from organized flow structures to dissipative turbulent motion. In Figure 60, the time-averaged fields of the Q-criterion, computed for all the experiments performed in this study, are presented.

As expected, the core of the main flow, where turbulent activity is relatively weak, is characterized by values of Q $\approx$ 0. In contrast, elevated magnitudes of Q appear along the periphery of the main flow. These higher values indi-

cate regions of intensified rotational motion associated with instabilities generated by the plume's descent toward the bottom and by the development of Kelvin–Helmholtz billows. This approach allows us to distinguish between the main flow and the mixing layer by defining the perimeter of the plume. Specifically, for each $y \neq 0$, the plume boundary is identified as the first point where $Q \neq 0$. This boundary forms the characteristic triangular shape of a hyperpycnal inflow, with the vertex of the triangle corresponding to the plunging point. In the region where the two more turbulent sides of the flow merge, the plume has fully decayed along the inclined bottom, transitioning into a gravity current.

This is also confirmed by the computation of Turbulent Kinetic Energy (TKE) [70], which formula is:

$$\mathrm{TKE} = \frac{1}{2}\left(u_i'^2 + u_j'^2\right) \tag{53}$$

where u_i' and u_j' denote the fluctuating components of the velocity in the i- and j-directions, respectively, defined as deviations from the corresponding mean velocities. As observable in Figure 61, the distribution of TKE closely follows the behavior highlighted by the Q-criterion.

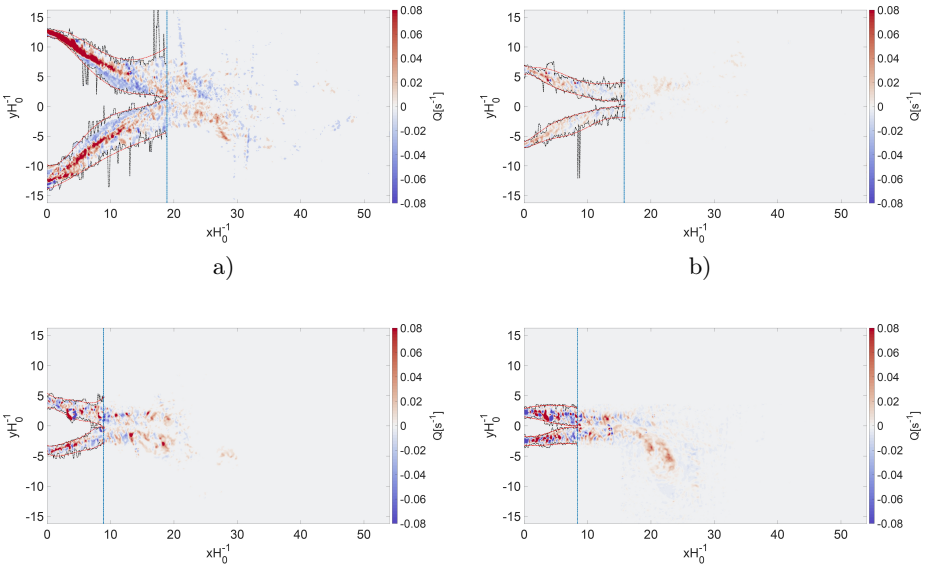

Figure 60: Q-criterion based evaluation of plunging location for a) $W_0 = 2.0$ m, b) $W_0 = 1.0$ m, c) $W_0 = 0.67$ m, d) $W_0 = 0.4$ m. Blue dotted lines indicate the plunge location and red dotted lines indicate the smoothed vortex boundaries.

Within the core of the main flow, both quantities have lower values, indicating that this region is dominated by relatively stable turbulent activity. In contrast, the lateral boundaries of the plume exhibit a pronounced increase in TKE, related to the inflow condition. This rise corresponds to the zones where strong shear develops between the high-momentum jet core and the surrounding ambient fluid. The resulting velocity gradients enhance turbulent production, leading to the formation of energetic eddies and a progressive mixing of the plume with the environment. These high-TKE regions are also associated with the downward deflection and eventual decay of the plume as it entrains ambient water. Notably, the position of the plunging point, previously estimated through the analysis of the Q-criterion, roughly coincides with the location where the two lateral shear layers of the plume converge. This merging of the plume sides corresponds to the maximum observed TKE, confirming that intense turbulent interactions and enhanced mixing characterize the plunging point.

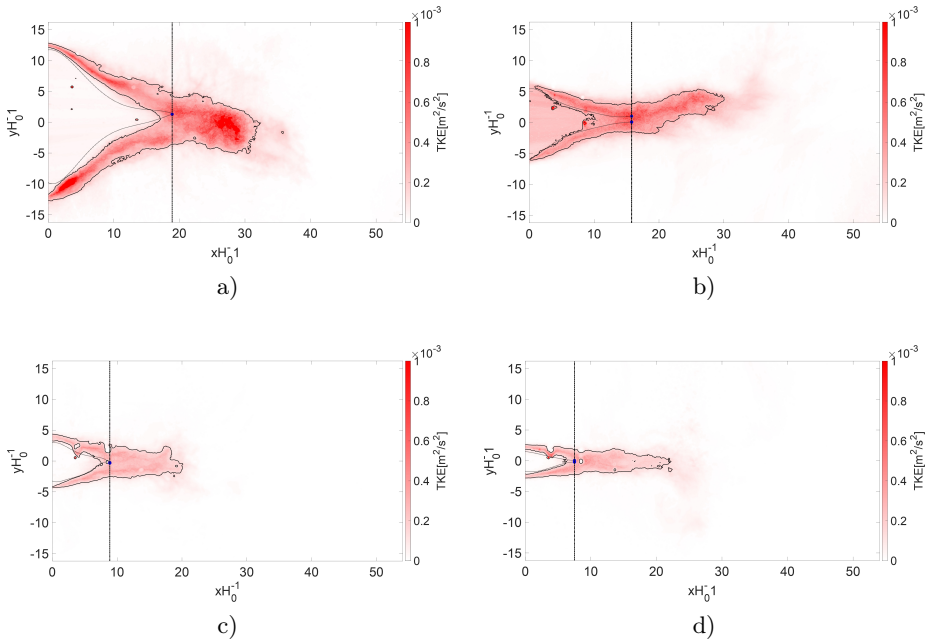

Figure 61: Near-surface experimental Turbulent Kinetic Energy (TKE) fields with qualitative comparison with the plunge location obtained from Q-criterion for a) $W_0 = 2.0$ m, b) $W_0 = 1.0$ m, c) $W_0 = 0.67$ m, d) $W_0 = 0.4$ m.

Using this approach for all the experiments conducted in this study, it is possible to precisely identify the plunging point as can be observed in Table 11.

In all experimental configurations, the volumetric flow rate injected into the tank is maintained approximately constant. However, by increasing the inlet channel width while maintaining the same inflow velocity, a larger mass of saline water enters the tank. This additional incoming mass results in a greater distance between the channel outlet and the plunging region. Indeed, as shown in Figure 62, increasing the channel width leads to a downstream shift of x_p with respect to the channel outlet, demonstrating an almost linear increasing trend (red dotted line in 62), this behavior is characteristic of this class of currents and has been extensively discussed in [46].

Table 11: Plunge point position for the different channel widths. $W_0 H_0^{-1}$ is the channel aspect ratio. $x_{p,exp}$ represents the plunge locations obtained experimentally.

W_0 [m]	W_0/H_0	$\mathrm{Fr}_{d,0}$	$x_{p,exp}$ [m]	$x_{p,exp}/H_0$
0.4	5.40	5.0	0.56	7.56
0.67	8.90	3.5	0.62	8.37
1	13.50	4.8	0.86	11.61
2	27.00	4.0	1.41	19.04

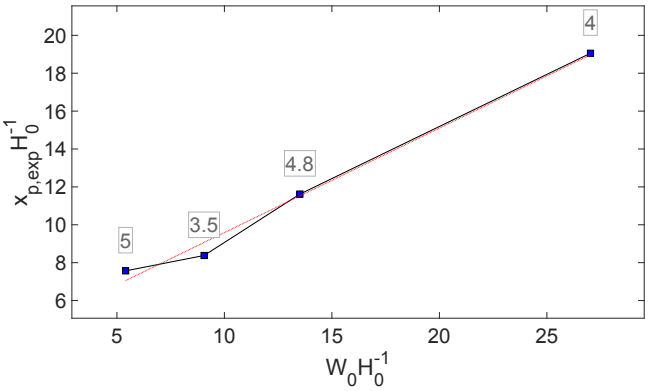

Figure 62: Variation of plunge position with inlet aspect ratio, showing the trend line (dashed red) and each data point annotated with its respective inflow densimetric Froude number.

7.2 Surface velocity vs Plunging Point

Once the plunging point was identified, the streamwise velocity trends were analysed for each case. The velocity field was sampled on the near-surface slice

of the domain, along a reference centreline located at the mid-span of the domain (see Figure 63, blue line). From these data, it can be clearly observed that at the channel outlet ($x = 0$) the flow exhibits an initial region in which the streamwise velocity remains approximately constant, with only a slight decreasing trend. Moving downstream from the outlet, the streamwise velocity undergoes a rapid decay, eventually reaching a plateau well upstream of the plunging point (see Figure 64a). All four cases display a qualitatively similar behaviour, although characterised by different decay lengths and slopes. However, when the streamwise coordinate and velocity are non-dimensionalised using x_p and U_{ref} (where U_{ref} denotes the streamwise velocity measured along the reference centreline immediately upstream of the channel outlet), all velocity profiles collapse onto a common trend (see Figure 64b). This collapse indicates that, despite the differences in channel width, the underlying flow dynamics follow a common behavior across the analyzed cases.

An exception is observed for the case with $W = 2\,\text{m}$, for which, even after non-dimensionalisation, the velocity decay exhibits a steeper slope. This discrepancy may be attributed to the increasing relevance of the ratio between the channel width and the domain width, which begins to significantly influence the flow development.

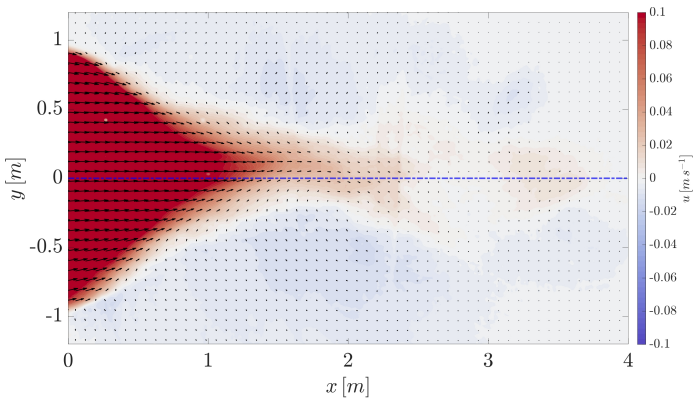

a)

Figure 63: Velocity contour of the case $W = 2m$, the blue line indicate longitudinal centre-line of the domain

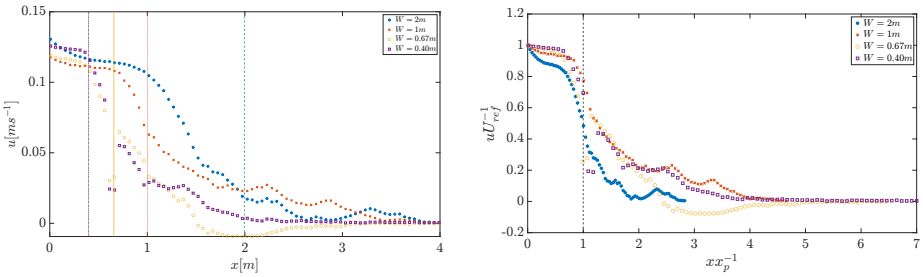

Figure 64: Superficial Streamwise velocity trends at the longitudinal centre-line of the domain.

7.3 Transient Fields

Considering the time-averaged Q-criterion fields, the mixing layer developing along the lateral boundaries of the main current can be clearly identified. In Figure 60, a **lower boundary** is defined as the interface separating the core of the main flow from the surrounding mixing region, as discussed in the previous section. An **upper boundary** is instead identified at the outer edge of the current, where the Q-criterion approaches zero ($Q \approx 0$), and is therefore interpreted as the upper limit of the mixing layer. Both boundaries are indicated by red dashed lines.

To investigate the temporal evolution of the dominant features of the mixing layer, a **central reference** line is defined midway between the lower and upper boundaries. This line, shown in green in Figure 65, follows the region where mixing is most intense and where the Q-criterion reaches its largest values, thus providing a representative path for the analysis of the unsteady dynamics.

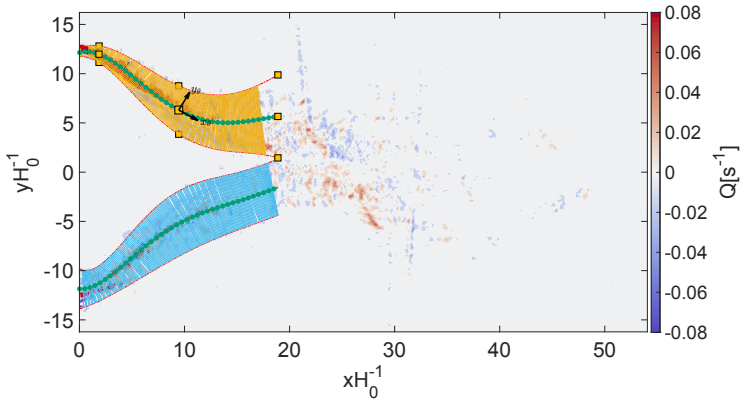

Figure 65: Identification of the mixing layer for $W_0 = 2.0m$ at the lateral boundaries of the main flow. The central reference line is shown in green, yellow squares indicate the sampling points employed for the extraction of the velocity components, and the local reference frame (x_θ, x_θ) is also reported in black.

The process described in the previous sections leads to the formation of coherent mixing structures that strongly characterise the physics of the problem. For instance, [42], with reference to the gravity current once fully developed along the bed, analyses the contribution to mixing associated with the formation of Kelvin-Helmholtz and Rayleigh-Taylor structures, also proposing a criterion to distinguish their respective contributions based on their characteristic time scales. In contrast to these horizontally oriented structures, the present study focuses on surface instabilities, analogous to KH structures but characterized by a vertical axis of rotation, that develop between the inlet region and the plunging point.In order to further identify and characterise the coherent structures typical of gravity currents, such as Kelvin-Helmholtz billows, the temporal evolution of the velocity components was analysed.

For this purpose, three sampling points, extracted from the PIV velocity measurement, were placed along the reference lines defined above: one located close to the channel outlet, one positioned in the vicinity of the plunging point, and one at an intermediate location between these two regions. These probes were selected to capture the characteristic dynamics of the flow in three distinct zones of the configuration: the outlet region, the plunging region, and a midstream region where the decay of the current is not directly affected by the boundary conditions associated with either the inlet or the plunging point (Upstream, Midstream, and Downstream probes).

Near the channel outlet, the flow dynamics are strongly influenced by the discharge of the denser fluid, whereas in the plunging region, the motion is affected, particularly near the lower boundary, by the interaction between the currents originating from both sides of the triangular main flow. The velocity time series extracted at the probe locations were analysed in terms of instantaneous signal amplitude and Power Spectral Density (PSD).

The PSD analysis represents a fundamental diagnostic tool for identifying

the dominant frequencies in turbulent flows. By transforming the velocity time series into the frequency domain via Fourier analysis, the PSD quantifies the distribution of kinetic energy across different frequency bands [70]. Peaks in the spectrum are associated with characteristic oscillatory phenomena, such as coherent structures or flow instabilities, whose temporal scales are directly linked to the underlying dynamics. In the present study, the identification of spectral peaks within specific frequency ranges enables the detection of Kelvin–Helmholtz billows and other coherent features developing within the mixing layer, providing a quantitative measure of their dominant timescales.

Figures 66 and 67 show the velocity signals recorded by the three probes located along the characteristic reference lines, for the tangential and normal velocity components, u_θ and v_θ, respectively. The signal measured at the Midstream probe along the central reference line (see, for instance, Figure 66, row b, column 2) is characterised by reduced noise levels, both in terms of instantaneous amplitude and spectral content. In this case, the PSD (Figures 68 and 69) exhibits a clear and well-defined dominant frequency for both velocity components.

A comparable behaviour is observed only for the v_θ component at the Midstream probe located along the upper boundary (row a, column 2 in Figures 66–69). In these regions, the spectral energy remains sufficiently high to allow the identification of characteristic frequencies associated with the dominant unsteady dynamics of the flow.

In contrast, at the lower boundary (row c in Figures 66–69), corresponding to the interface with the core of the main flow, the velocity fluctuations are significantly weaker and do not yield clearly identifiable spectral peaks. This behaviour reflects the more stable nature of the flow in this region, which is only marginally affected by the unsteady motions developing within the mixing layer and remains largely dominated by the relatively steady core of the gravity current.

Overall, these results demonstrate that in the region where the saline plume is injected into the tank, shear-induced instabilities arise due to the interaction between fluids of different densities. These instabilities evolve both spatially and temporally along the mixing layer, progressively losing coherence and eventually dissipating into a diffuse wake in the downstream portion of the flow, particularly in the vicinity of the plunging point.

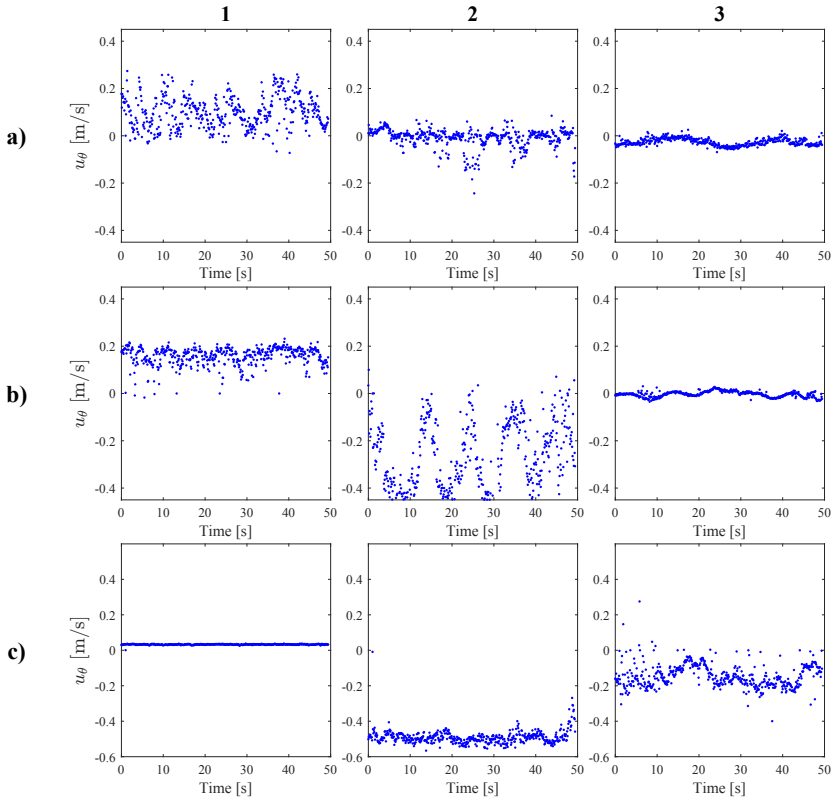

Figure 66: Time-series amplitude of the component u_θ for the $W_0 = 2\,\mathrm{m}$ case. The spectra are computed at the (1) upstream, (2) midstream, and (3) downstream probes, corresponding to the (a) upper boundary, (b) central reference line, and (c) lower boundary locations.

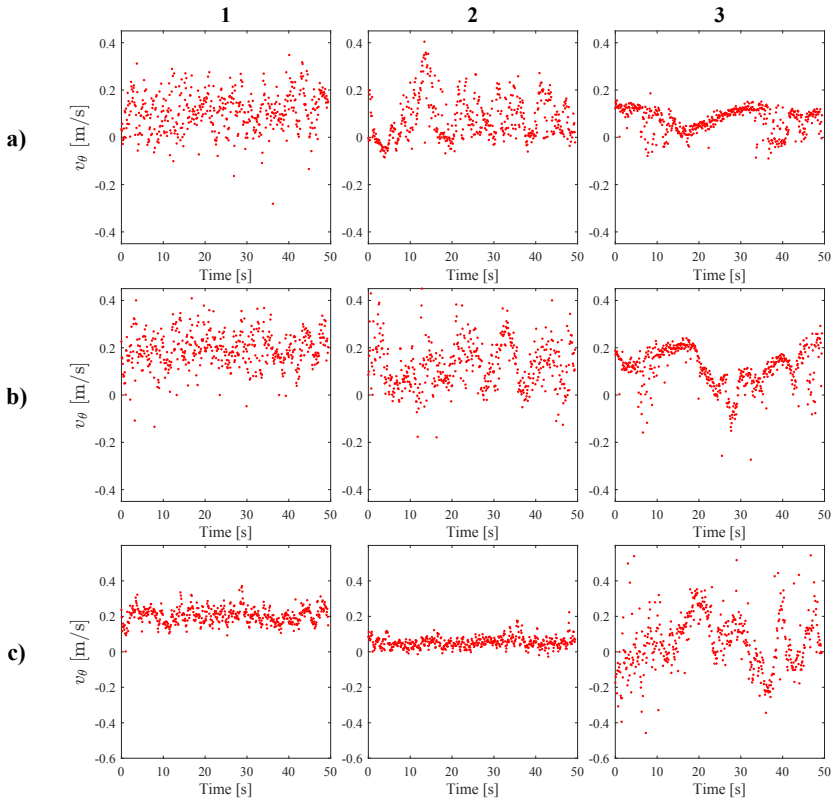

Figure 67: Time-series amplitude of the component v_θ for the $W_0 = 2\,\mathrm{m}$ case. The spectra are computed at the (1) upstream, (2) midstream, and (3) downstream probes, corresponding to the (a) upper boundary, (b) central reference line, and (c) lower boundary locations.

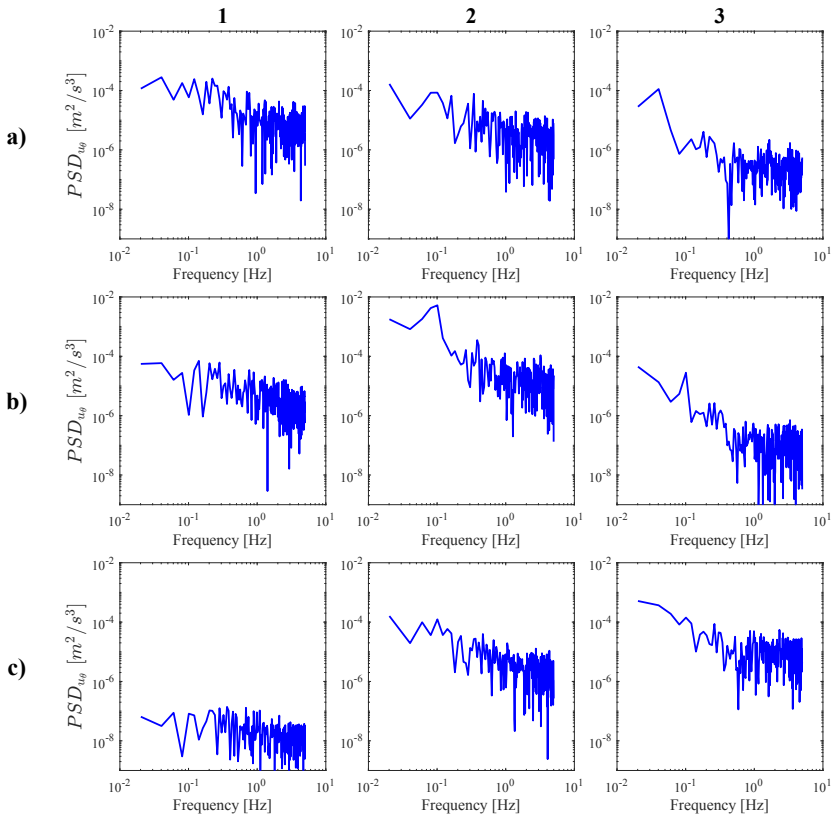

Figure 68: PSD of the velocity component u_θ for the $W_0 = 2\,\mathrm{m}$ case. The spectra are computed at the (1) upstream, (2) midstream, and (3) downstream probes, corresponding to the a) upper boundary, b) central reference line, and c) lower boundary locations.

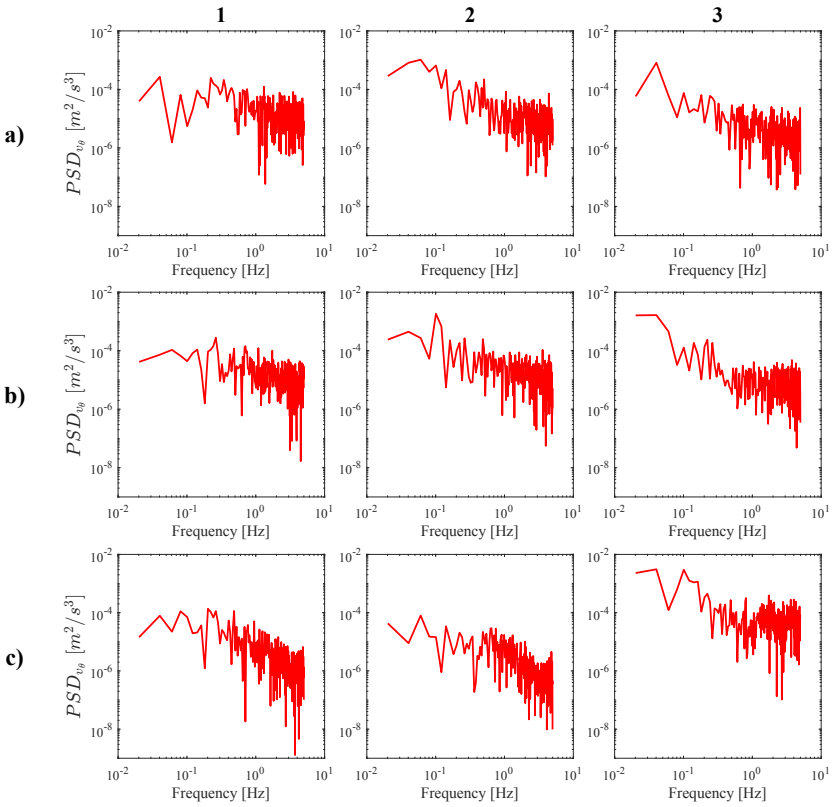

Figure 69: PSD of the velocity component v_θ for the $W_0 = 2\,\mathrm{m}$ case. The spectra are computed at the (1) upstream, (2) midstream, and (3) downstream probes, corresponding to the a) upper boundary, b) central reference line, and c) lower boundary locations.

Based on the results discussed above, the analysis was subsequently focused on the Midstream probe located along the central reference line, which is considered representative of the flow dynamics within the mixing layer. The same analysis was then extended to the remaining experimental configurations. As shown in Figure 70, with the exception of the case $W_0 = 0.4$ m, which exhibits a more complex spectral distribution and does not follow the general trend, all velocity components consistently display a dominant spectral peak at frequencies of the order of 10^{-1} Hz.

This frequency range is plausibly associated with buoyancy-driven instabilities and, in particular, with the formation and evolution of Kelvin–Helmholtz billows [52]. The presence of such coherent structures reflects the strong interaction between shear and stratification within the mixing layer, and their characteristic timescales are directly manifested in the observed spectral peaks.

The recurrence of this dominant frequency across different channel widths and velocity components suggests the existence of a robust dynamical mechanism governing the flow evolution, likely linked to the intrinsic instability of the gravity current interface.

A quantitative summary of the dominant frequencies for each configuration is provided in Table 12, where the values obtained for u_θ, v_θ, and $|\nu|$ are reported for the Midstream probe along the central reference line. These results provide a coherent framework for interpreting the temporal dynamics of the flow and further support the identification of Kelvin–Helmholtz-type activity as a key feature of the mixing process.

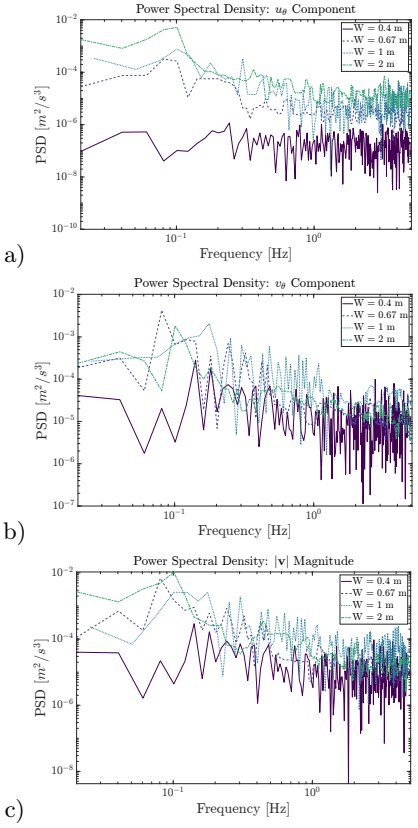

Figure 70: PSD of the velocity component along a) x_θ, b) y_θ, and their vectorial combination c) for all the experimental cases.

Table 12: Dominant frequencies extracted from the PSD analysis at the Midstream probe of the internal line, for different channel widths W. Frequencies are reported for the velocity components u_θ and v_θ, as well as for their vectorial combination $|\nu|$.

W_0	u_θ [Hz]	v_θ [Hz]	$\lvert v\rvert$ [Hz]
0.4	0.242	0.141	0.141
0.67	0.081	0.081	0.081
1	0.101	0.177	0.177
2	0.101	0.101	0.101

8 Conclusions

In this thesis, various types of gravity currents were analyzed through numerical simulations in combination with laboratory data, providing deeper insight into their underlying physical mechanisms.

Gravity currents in lock-exchange configurations: The study initially investigated the near-wall behavior of gravity currents using WR-LES to assess the feasibility of approximating the flow with WF-LES. Subsequently, coarse-grid WF-LES simulations were conducted to reduce computational costs. The main findings are summarized as follows:

- **Boundary layer characterization:** A well-defined boundary layer forms at the current head, particularly during the self-similar phase, where velocity profiles approximately follow a logarithmic law. Compared to the canonical logarithmic law, a different inclination of the profile is observed, associated with stratification and dependent on both the reduced gravity g' and the flow depth H.
- **Wall-modeled LES performance:** Coarser-grid WF-LES approaches, both with and without wall functions, reproduced the main flow features with good qualitative agreement, except for the Blended wall model. The temporal evolution of the gravity current front was captured with low relative errors, typically within 0.25%–2.70%. Notably, the case employing Spalding's wall model exhibited a progressive reduction in error relative to the reference simulation over time. However, due to limited wall-normal resolution, coarser-grid cases were unable to resolve near-bottom turbulent structures observed in the wall-resolved simulation, indicating potential deficiencies in representing sediment resuspension mechanisms. The largest discrepancies among cases were associated with entrainment, mean density, and the overall area of the gravity current. When considering the flow as a whole, the unresolved case and the modified eddy diffusivity approach showed the closest agreement with the WR-LES reference. In contrast, cases incorporating eddy viscosity intensification performed better when focusing on the gravity current head, particularly during the later stages of the flow evolution. Overall, Spalding's wall function provided the most accurate representation of near-wall dynamics among the tested approaches.
- **Computational efficiency:** Employing wall models reduced the computational time from roughly 10^2 to 10^0 hours per case (using 320 cores), while maintaining high fidelity. This efficiency gain enables simulations of more complex geometries and flows at higher Reynolds numbers.

Sediment-laden gravity currents interacting with submerged obstacles: both the single-phase (*buoyantBoussinesqPimpleFoam*) and two-phase (*SedFoam*) solvers were validated against laboratory experiments, demonstrating their ability to reproduce the key flow features. The main findings are as follows:

- **Obstacle impact on flow:** The presence of a cylinder substantially altered the flow dynamics, mixing processes, and near-bed shear stresses. The obstacle caused a deceleration of the current front; during this phase, momentum is predominantly transferred from the streamwise to the wall-normal direction. This is followed by a plunging phase, during which the plume fully decays at the bottom of the domain.
- **Erosion and deposition:** The cylindrical obstacle enhances erosional processes downstream, particularly near the current head, while denser fluid preferentially deposits upstream. This effect is especially pronounced in turbidity currents, where the erosive potential increases immediately downstream of the obstacle, partly due to flow plunging. Furthermore, the plunging generates a vortical region just downstream of the cylinder, transiently establishing a secondary erosional front ahead of the main current head.
- **Hydrodynamic forces:** Analysis of drag and lift coefficients indicated that the cylinder strongly influenced flow dynamics, highlighting the combined effects of obstacle interaction and sediment load.

Hyperpycnal plumes: The surface dynamics of a hyperpycnal plume, representative of a river–basin system, were analyzed using laboratory data from the Coriolis platform (LEGI, Grenoble) to assess the influence of inlet geometry. The main findings are:

- **Plunging point identification:** A quantitative approach based on the Q-criterion and turbulent kinetic energy was developed to determine the location of the plunging point.
- **Channel width effects:** The plunging location shifts linearly downstream with increasing inlet channel width, demonstrating a predictable dependence of detachment on inflow geometry.
- **Mixing dynamics:** The mixing layer between the river inflow and the plunging region is characterized by the spatial and temporal evolution of Kelvin–Helmholtz structures. A spectral decomposition was employed to quantify the dynamics of these structures.

These results provide a robust foundation for future investigations of sediment-laden and hyperpycnal flows in natural environments, supporting studies of varying inflow conditions, sediment concentrations, and complex geometries.

Declaration

The author declares to have used Google Translate, WordReference, Grammarly, ChatGPT, GEMINI, and Copilot for translation from the native language and text verification. The translations generated with the support of these tools have been carefully checked and modified as necessary.

Acknowledgments

This work is funded by the National Recovery and Resilience Plan project TeRABIT (Terabit network for Research and Academic Big data in Italy - IR0000022 - PNRR Missione 4, Componente 2, Investimento 3.1 CUP I53C21000370006) in the frame of the European Union - NextGenerationEU funding.

The author acknowledges the support of the CINECA award under the ISCRA initiative for the availability of high-performance computing resources and support. Furthermore, the author also acknowledges the LEGI laboratory of the Grenoble-Alpes University for the hospitality and availability.

9 Bibliography

References

[1] Adduce, C., Sciortino, G. & Proietti, S. Gravity Currents Produced by Lock Exchanges: Experiments and Simulations with a Two-Layer Shallow-Water Model with Entrainment. J. Hydraul. Eng. 138, 111-121 (2012).

[2] Zordan, J., Sher, D. & Huppert, H. E. Experimental and numerical investigation of lock-exchange gravity currents encountering cylindrical obstacles. Physics of Fluids 32(10), 106605 (2020).

[3] Armanini, A. Initiation of sediment motion. In Principles of River Hydraulics, edited by A. Armanini, Springer International Publishing, Cham, 2018, pp. 49–76.

[4] Armenio, V. & Sarkar, S. An investigation of stably stratified turbulent channel flow using large-eddy simulation. J. Fluid Mech. 459, 1-42 (2002).

[5] Blanckaert, K., Vinnå, L. R., Bouffard, D., Lemmin, U. & Barry, D. A. Field observations reveal how plunging mixing and sediment resuspension affect the pathway of a dense river inflow into a deep stratified lake. Water Resour. Res. 60(4), e2023WR036813 (2024).

[6] Boegman, L. Currents in Stratified Water Bodies 2: Internal Waves. Encyclopedia of Inland Waters, 539-558 (2009).

[7] Bonamy, C., Chauchat, J., Cheng, Z., Nagel, T. & Hsu, T. J. SEDFOAM: An OpenFOAM solver for sediment transport. HAL Archive, hal-01685275 (2018).

[8] Buchhave, P. Particle image velocimetry—status and trends. Exp. Therm. Fluid Sci. 5, 586-604 (1992).

[9] Cabot, W. & Moin, P. Approximate Wall Boundary Conditions in the Large-Eddy Simulation of High Reynolds Number Flow. Flow Turbul. Combust. 63, 269-291 (2000).

[10] Chapman, D. Computational Aerodynamics Development and Outlook. AIAA Journal 17, 1293-1313 (1979).

[11] Chauchat, J., Cheng, Z., Nagel, T., Bonamy, C. & Hsu, T. J. SedFoam-2.0: a 3-D two-phase flow numerical model for sediment transport. Geosci. Model Dev. 10, 4367-4392 (2017).

[12] Chong, M. S., Perry, A. E. & Cantwell, B. J. A general classification of three-dimensional flow fields. Phys. Fluids A 2(5), 765-777 (1990).

[13] Chowdhury, M. & Testik, F. A review of gravity currents formed by submerged single-port discharges in inland and coastal waters. Environ. Fluid Mech. 14, 265-293 (2014).

[14] Comte, F. & Lesieur, M. Large-eddy simulation of transition to turbulence in a boundary layer developing spatially over a flat plate. J. Fluid Mech. 326, 1-36 (1996).

[15] De Vanna, F., Bernardini, M., Picano, F. & Benini, E. Wall-modeled LES of shock-wave/boundary layer interaction. Int. J. Heat Fluid Flow 98, 109071 (2022).

[16] Ding, W., Cai, T., Sun, H., Zhao, X. & Fan, Y. Numerical simulation study on the interaction between a gravity current and horizontal cylinders. Ocean Eng. 289, 116236 (2023).

[17] Drew, D. A. Mathematical modeling of two-phase flow. Annu. Rev. Fluid Mech. 15, 261-291 (1983).

[18] Ellison, T. & Turner, J. Turbulent entrainment in stratified flows. J. Fluid Mech. 6(3), 423-448 (1959).

[19] Fan, G., Liu, Y., Zhao, W. & Wan, D. Effect of wall stress models and subgrid-scale models for flow past a cylinder at Reynolds number 3900. Phys. Fluids 36, 015152 (2024).

[20] Fannelop, T. & Waldman, G. Dynamics of Oil Slicks. AIAA J. 10, 506-510 (1972).

[21] Ferziger, J., Perić, M. & Street, R. Computational Methods for Fluid Dynamics. Springer (2020).

[22] Franck, N. & Ducros, F. Subgrid-Scale Stress Modelling Based on the Square of the Velocity Gradient Tensor. Flow Turbul. Combust. 62, 183-200 (1999).

[23] Georgoulas, A., Angelidis, P., Panagiotidis, T. & Kotsovinos, N. 3D numerical modelling of turbidity currents. Environ. Fluid Mech. 10, 603-635 (2010).

[24] Gong, C., Wang, Y., Rebesco, M., Salon, S. & Steel, R. How do turbidity flows interact with contour currents in unidirectionally migrating deep-water channels?. Geology 46, 551-554 (2018).

[25] Gonzalez-Juez, E., Meiburg, E. & Constantinescu, G. Gravity current flow past a circular cylinder: forces, wall shear stresses and implications for scour. J. Fluid Mech. 657, 231-259 (2010).

[26] Goodarzi, D., Lari, K., Khavasi, E. & Abolfathi, S. Large eddy simulation of turbidity currents in a narrow channel with different obstacle configurations. Sci. Rep. 10, 12814 (2020).

[27] Härtel, C., Meiburg, E. & Necker, F. Analysis and direct numerical simulation of the flow at a gravity-current head. Part 1. Flow topology and front speed for slip and no-slip boundaries. J. Fluid Mech. 418, 189-212 (2000).

[28] Heerema, C., Cartigny, M., Jacinto, R., Simmons, S., Apprioual, R. & Talling, P. How distinctive are flood-triggered turbidity currents?. J. Sediment. Res. 92, 1-11 (2022).

[29] Hogg, C., Pietrasz, V., Ouellette, N. & Koseff, J. Dispersion and transport of hypersaline gravity currents in the presence of internal waves at a pycnocline. OS11A-2005 (2015).

[30] Hsu, T.-J., Jenkins, J. T. & Liu, P. L. F. On two-phase sediment transport: dilute flow. J. Geophys. Res. 108, 14 (2003).

[31] Hsu, S.-K., Kuo, J., Lo, C.-L., Tsai, C.-H., Doo, W.-B., Ku, C.-Y. & Sibuet, J.-C. Turbidity currents, submarine landslides and the 2006 Pingtung earthquake off SW Taiwan. Terrestrial, Atmospheric and Oceanic Sciences 19(6), 767-772 (2008).

[32] Hsu, T.-J. & Liu, P. L. F. Toward modeling turbulent suspension of sand in the nearshore. J. Geophys. Res. 109, C06018 (2004).

[33] Hunt, J. C. R., Wray, A. A. & Moin, P. Eddies, streams, and convergence zones in turbulent flows. Center for Turbulence Research Report CTR-S88, Stanford University (1988).

[34] Huppert, H. & Simpson, J. The slumping of gravity currents. J. Fluid Mech. 99, 785-799 (1980).

[35] Inghilesi, R., Adduce, C., Lombardi, V., Roman, F. & Armenio, V. Axisymmetric three-dimensional gravity currents generated by lock exchange. J. Fluid Mech. 851, 507-544 (2018).

[36] Jackson, R. Locally averaged equations of motion for a mixture of identical spherical particles and a Newtonian fluid. Chem. Eng. Sci. 52(15), 2457-2469 (1997).

[37] Jayatilleke, C. The influence of Prandtl number and surface roughness on the resistance of the laminar sub-layer to momentum and heat transfer (1966).

[38] Jeong, J. & Hussain, F. On the identification of a vortex. J. Fluid Mech. 285, 69-94 (1995).

[39] Kaltenbach, H. J. Cell aspect ratio dependence of anisotropy measures for resolved and subgrid scale stresses. J. Comput. Phys. 136, 399-410 (1997).

[40] Kim, J., Moin, P. & Moser, R. Turbulence statistics in fully developed channel flow at low Reynolds number. J. Fluid Mech. 177, 133-166 (1987).

[41] Kneller, B. & Buckee, C. The structure and fluid mechanics of turbidity currents: a review of some recent studies and their geological implications. Sedimentology 47, 62-94 (2000).

[42] Kostaschuk, R., Nasr-Azadani, M. M., Meiburg, E., et al. On the Causes of Pulsing in Continuous Turbidity Currents. J. Geophys. Res. Earth Surf. 123(11), 2827-2843 (2018).

[43] Kuhlbrodt, T., Griesel, A., Montoya, M., Levermann, A., Hofmann, M. & Rahmstorf, S. On the driving processes of the Atlantic meridional overturning circulation. Rev. Geophys. 45 (2007).

[44] Kundu, P. K., Cohen, I. M. & Dowling, D. R. Fluid Mechanics. 6th ed., Academic Press (2015).

[45] Kyrousi, F., Leonardi, A., Roman, F., Armenio, V., Zanello, F., Zordan, J., Juez, C. & Falcomer, L. Large Eddy Simulations of sediment entrainment induced by a lock-exchange gravity current. Adv. Water Resour. 114, 102-118 (2018).

[46] Lamb, M. P., McElroy, B., Kopriva, B., Shaw, J. & Mohrig, D. Linking river-flood dynamics to hyperpycnal-plume deposits: Experiments, theory, and geological implications. Geol. Soc. Am. Bull. 122(9-10), 1389-1400 (2010).

[47] López Castaño, S., Petronio, A., Petris, G. & Armenio, V. Assessment of Solution Algorithms for LES of Turbulent Flows Using OpenFOAM. Fluids 4, 171 (2019).

[48] Lube, G., Breard, E. C. P., Jones, J., Fullard, L., Dufek, J., Cronin, S. J. & Valentine, G. A. Characteristics and controls of the runout behaviour of non-Boussinesq particle-laden gravity currents – A large-scale experimental investigation of dilute pyroclastic density currents. Earth Planet. Sci. Lett. 533, 116042 (2020).

[49] Maggi, M., Adduce, C. & Negretti, M. Lock-release gravity currents propagating over roughness elements. Environ. Fluid Mech. 22, 383-402 (2022).

[50] Maggi, M., Negretti, M., Hopfinger, E. & Adduce, C. Turbulence characteristics and mixing properties of gravity currents over complex topography. Phys. Fluids 35, 016607 (2023).

[51] Maggi, M. R., Di Lollo, G. & Adduce, C. Dynamics and mixing of gravity currents over an array of cylindrical obstacles. Phys. Fluids 37, 076629 (2025).

[52] Malekmohammadi, S., Cheynet, E. & Reuder, J. Observation of Kelvin-Helmholtz billows in the marine atmospheric boundary layer by a ship-borne Doppler wind lidar. Sci. Rep. 15, 5245 (2025).

[53] Meiburg, E. & Kneller, B. Turbidity Currents and Their Deposits. Annu. Rev. Fluid Mech. 42, 135-156 (2010).

[54] Menter, F. Two-equation eddy-viscosity turbulence models for engineering applications. AIAA Journal 32, 1598-1605 (1994).

[55] Miramontes, E., Eggenhuisen, J., Jacinto, R., Poneti, G., Pohl, F., Normandeau, A., Campbell, D. & Hernández-Molina, F. Channel-levee evolution in combined contour current–turbidity current flows from flume-tank experiments. Geology 48, 353-357 (2020).

[56] Mukha, T., Rezaeiravesh, S. & Liefvendahl, M. A library for wall-modelled large-eddy simulation based on OpenFOAM technology. Comput. Phys. Commun. 239, 204-224 (2019).

[57] Mulder, T., Syvitski, J. P. M., Migeon, S., Faugères, J. C. & Savoye, B. Marine hyperpycnal flows: Initiation, behavior and related deposits. A review. Mar. Pet. Geol. 20(6-8), 861-882 (2003).

[58] Necker, T., Härtel, C., Kleiser, L. & Meiburg, E. High-resolution simulations of particle-driven gravity currents. Int. J. Multiphas. Flow 28(2), 279-300 (2002).

[59] Nogueira, H., Adduce, C., Alves, E. & Franca, M. Analysis of lock-exchange gravity currents over smooth and rough beds. J. Hydraulic Res. 51, 417-431 (2013).

[60] Nogueira, H. I. S., Adduce, C., Alves, E. & Franca, M. J. Dynamics of the head of gravity currents. Environ. Fluid Mech. 14, 519-540 (2014).

[61] Normandeau, A., Campbell, D. & Cartigny, M. The influence of turbidity currents and contour currents on the distribution of deep-water sediment waves offshore eastern Canada. Sedimentology 66, 1746-1767 (2019).

[62] Ooi, S., Constantinescu, G. & Weber, L. Numerical simulations of lock-exchange compositional gravity currents. J. Fluid Mech. 635, 361-388 (2009).

[63] Ottolenghi, L., Adduce, C., Inghilesi, R., Armenio, V. & Roman, F. Entrainment and mixing in unsteady gravity currents. J. Hydraul. Res. 54, 541-557 (2016).

[64] Ottolenghi, L., Adduce, C., Inghilesi, R., Roman, F. & Armenio, V. Mixing in lock-release gravity currents propagating up a slope. Phys. Fluids 28, 056604 (2016).

[65] Ottolenghi, L., Adduce, C., Roman, F. & Armenio, V. Analysis of the flow in gravity currents propagating up a slope. Ocean Model. 115, 1-13 (2017).

[66] Pelmard, J., Norris, S. & Friedrich, H. LES grid resolution requirements for the modelling of gravity currents. Comput. Fluids 174, 256-270 (2018).

[67] Piomelli, U. Wall-layer models for large-eddy simulations (2001).

[68] Piomelli, U. Wall-layer models for large-eddy simulations. Prog. Aerosp. Sci. 44, 437-446 (2008).

[69] Pittalis, D., Carletti, A., Ghiglieri, G. & Celico, F. The influence of hydrogeological properties, seawater intrusion and refreshening on the quality of groundwater used for irrigation in an agricultural coastal plain in North Sardinia, Italy. Environ. Earth Sci. 75, 963 (2016).

[70] Pope, S. Turbulent flows. Cambridge Univ. Press (2015).

[71] Rebesco, M., Hernández-Molina, F., Van Rooij, D. & Wåhlin, A. Contourites and associated sediments controlled by deep-water circulation processes: State-of-the-art and future considerations. Mar. Geol. 352, 111-154 (2014).

[72] Rottman, J. & Simpson, J. Gravity currents produced by instantaneous releases of a heavy fluid in a rectangular channel. J. Fluid Mech. 135, 95-110 (1983).

[73] Schiller, L. & Naumann, A. A drag coefficient correlation. Z. Ver. Deutsch. Ing. 77, 318-320 (1935).

[74] Sequeiros, O. Estimating turbidity current conditions from channel morphology: A Froude number approach. J. Geophys. Res. Oceans 117 (2012).

[75] Serchi, G., Salsi, A., Besio, G. & Vittori, G. A numerical study of the triggering mechanism of a lock-released density current. Eur. J. Mech. B-Fluids 30(5), 543-551 (2011).

[76] Shanmugam, G. New Perspectives on Deep-Water Sandstones: Origin, Recognition, Initiation, and Reservoir Quality, Handbook of Petroleum Exploration and Production, Vol. 9, Elsevier, Amsterdam, 524 pp. (2012).

[77] Shi, H., Negretti, M., Chauchat, J., Blanckaert, K., Lemmin, U. & Barry, D. A. Unconfined plunging of a hyperpycnal river plume over a sloping bed and its lateral spreading: Laboratory experiments and numerical modeling. Water Resour. Res. 58(8), e2022WR032633 (2022).

[78] Shields, A. Application of similarity principles and turbulence research to bed-load movement. Preußische Versuchsanstalt für Wasserbau, Berlin, Germany (1936). Traduzione inglese: W.P. Ott & J.C. van Uchelen, California Institute of Technology, Pasadena, 1956.

[79] Simpson, J. Gravity currents in the environment and the laboratory. Cambridge University Press (1997).

[80] Spalding, D. A Single Formula for the "Law of the Wall". J. Appl. Mech. 28, 455-458 (1961).

[81] Stancanelli, L., Musumeci, R., Cavallaro, L. & Foti, E. A small scale Pressure Retarded Osmosis power plant: dynamics of the brackish effluent discharge along the coast. Ocean Eng. 130, 417-428 (2017).

[82] Temmerman, L., Leschziner, M. A., Mellen, C. P. & Fröhlich, J. Investigation of wall-function approximations and subgrid-scale models in large eddy simulation of separated flow in a channel with streamwise periodic constrictions. J. Heat Fluid Flow 24(2), 157-180 (2003).

[83] Thorez, S., Lemmin, U., Barry, D. A. & Blanckaert, K. Hydro-Sedimentary Processes of a Plunging Hyperpycnal River Plume Revealed by Synchronized Remote Imagery and Gridded Current Measurements. Water Resour. Res. 60, e2023WR035907 (2024).

[84] Tokyay, T., Constantinescu, G. & Meiburg, E. Lock-exchange gravity currents with a high volume of release propagating over a periodic array of obstacles. J. Fluid Mech. 672, 570-605 (2011).

[85] Tomasicchio, G. R. Capabilities and Limits for ADVP Measurements of Breaking Waves and Bores. Coastal Eng. 53, 27-37 (2006).

[86] Traer, M. M., Hilley, G. E., Fildani, A. & McHargue, T. The sensitivity of turbidity currents to mass and momentum exchanges between these underflows and their surroundings. Journal of Geophysical Research: Earth Surface, 117, F01009 (2012).

[87] Ungarish, M. An Introduction to Gravity Currents and Intrusions. 1st edn. Chapman and Hall/CRC, New York, 512 pp. (2009).

[88] Versteeg, H., Henson, J. & Malalasekera, W. An Adaptive Angular Quadrature for the Discrete Transfer Method Based on Error Estimation. J. Heat Transf. 125, 301-311 (2003).

[89] Westerweel, J., Elsinga, G. E. & Adrian, R. J. Particle image velocimetry for complex and turbulent flows. Annu. Rev. Fluid Mech. 45, 369-396 (2013).

[90] Wu, C. & Ouyang, H. Flow morphology in bottom-propagating gravity currents over immersed obstacles. AIP Adv. 10, 115103 (2020).

[91] Yang, Z. Large-eddy simulation: Past, present and the future. Chin. J. Aeronaut. 28(1), 11-24 (2015).

[92] Zgheib, N., Bonometti, T. & Balachandar, S. Direct numerical simulation of cylindrical particle-laden gravity currents. Comput. Fluids 123, 23-31 (2015).

[93] Zgheib, N., Ooi, A. & Balachandar, S. Front dynamics and entrainment of finite circular gravity currents on an unbounded uniform slope. J. Fluid Mech. 801, 322-352 (2016).

[94] Zhou, Q. & Mendoza, C. Gravity currents interacting with submerged obstacles: flow structure and mixing mechanisms. Environ. Fluid Mech. 17(4), 757-776 (2017).

UNIVERSITÀ
DEGLI STUDI
DI TRIESTE

La borsa di dottorato è cofinanziata con risorse dell'Unione europea, NextGeneration EU - Piano Nazionale di Ripresa e Resilienza, Missione 4 – Componente 2 – Investimento 3.1 CUP I53C21000370006